DOSIMETRIC EFFECTS OF PROSTATE CALCIFICATIONS IN HIGH-DOSE RATE BRACHYTHERAPY CALCULATIONS

by

William Musgrave

Submitted in partial fulfilment of the requirements
for the degree of Master of Science

at

Dalhousie University
Halifax, Nova Scotia
August 2017

TABLE OF CONTENTS

LIST OF TABLES

LIST OF FIGURES

ABSTRACT

Purpose: At the Nova Scotia Cancer Center (NSCC), high-dose rate (HDR) brachytherapy using ^{192}Ir is often used as a single-fraction dose boost for intermediate and high-risk prostate cancer patients prior to external-beam radiation therapy (EBRT). Recent dosimetric concerns have focused on material heterogeneities that cannot be accounted for in clinical treatment planning systems using the Task Group 43 (TG-43) water-based dose calculation algorithm. This work investigates the impact of prostate calcifications, a heterogeneity with a high atomic number, on dose distributions calculated using the EGSnrc code for Monte Carlo (MC) radiation transport in both water phantoms and heterogeneous virtual patient phantoms created from planning computed tomography (CT) images.

Methods: A model of Nucletron's microSelectron-v2 ^{192}Ir source was created using the EGSnrc C++ class library (egspp) and validated by computing TG-43 dosimetry parameters. In a series of phantom simulations, spherical prostate calcifications (with radii of 1 mm and 3 mm) were embedded near the source at distances of 5 mm and 5 cm and compared to homogeneous water phantom simulations. Finally, patient-specific calculations were performed using several tissue assignment schemes to assign prostate and calcified materials to a virtual patient phantom based upon a patient's planning CT. MC simulations were then performed using the dwell positions and weights derived from the treatment plan, while clinical metrics were extracted from the cumulative dose volume histograms (cDVHs) extracted from the resultant dose distributions.

Results: When benchmarked against literature results, TG-43 parameter values generally agreed within 2%. Shadowing effects were observed beyond the calcification in the phantom study, resulting in mean dose decreases of 1.48% and 6.80% for the small and large calcifications placed 5 mm away from the source. The maximum observed reductions to the prostate V_{100}, V_{150} and V_{200} in patient-specific phantoms were 1.78%, 1.18% and 0.40% respectively, compared to a water phantom, while the urethra D_{10} was reduced by only 26 cGy.

Conclusions: While the dosimetric effects were mild in the context of the patient's treatment, larger prostate calcifications simulated in water phantoms resulted in mean dose reductions of approximately 6.80% in the water phantom study. Hence, calcifications should be investigated in future work involving other patients with larger calcifications.

LIST OF ABBREVIATIONS USED

μ-PIXE	Micro-particle induced x-ray emission
AAPM	American Association of Physicists in Medicine
AP	Photon lower cutoff energy (PEGS4)
AJCC	American Joint Committee on Cancer
cDVHs	Cumulative dose-volume histograms
CPE	Charged-particle equilibrium
CPU	Central processing unit
CT	Computed tomography
CTV	Clinical target volume
DNA	Deoxyribonucleic acid
DVHO	Dose-volume histogram optimization
EBRT	External beam radiation therapy
ECUT	Electron lower cutoff energy
EGS	Electron-Gamma-Shower
egspp	EGSnrc C++ class library
ESTRO	European Society for Radiotherapy and Oncology
FTIR	Fourier transform infrared spectroscopy
HDR	High dose rate
HEBD	High-Energy Brachytherapy Dosimetry Group (AAPM/ESTRO)
HU	Hounsfield Units
HVL	Half-value layer
IR	Infrared
ICRU	International Commission on Radiation Units and Measurement
ICRU-38	ICRU Report No. 38
LDR	Low dose rate
MBDCAs	Model-based dose calculation algorithms
MC	Monte Carlo
MDR	Medium dose rate
MRI	Magnetic resonance imaging
NIST	National Institute of Standards and Technology
NSCC	Nova Scotia Cancer Center
OARs	Organs at risk
UP	Photon upper cutoff energy (PEGS4)
PCUT	Photon lower cutoff energy
PDR	Pulsed dose rate
PTV	Planning target volume
PSA	Prostate specific antigen
QA	Quality assurance
TG-43	Task Group No. 43
TG-56	Task Group No. 56
TG-186	Task Group No. 186
TRUS	Transrectal ultrasound

ACKNOWLEDGEMENTS

Firstly, I would like to thank my supervisor Dr. Krista Chytyk-Praznik for her invaluable guidance, mentorship and constructive criticism over the past two years. She was always willing to meet with me to assess research results – sometimes with limited notice in advance – and her generosity does not go unappreciated. Whether it was re-exporting an Oncentra plan from the brachytherapy suite, organizing an opportunity for me to observe HDR brachytherapy in person, or assisting me with QA-related issues on one of the linear accelerators in the Nova Scotia Cancer Center after clinical hours, she was dedicated to helping me succeed. Thanks for giving me the opportunity to pursue this wonderful project and remaining patient during the turbulent periods.

I would also like to gratefully acknowledge Dr. Alasdair Syme and Dr. Mammo Yewondwossen for all of the constructive criticism and assistance refining the scope of the project. This thesis has truly benefited from your collective domain-specific knowledge and guidance through many of the scientific subtleties I encountered. I would also like to thank Dr. James Robar for all of the mentorship and the opportunities to get involved in the Department of Medical Physics, along with Dr. David Parsons, Steve Bromwich and Scott Murphy for helping me with EGSnrc and/or cluster-related issues. Furthermore, I would like to thank the medical physicists, radiation oncologists, therapists, nurses and electronic technicians at the Nova Scotia Cancer Center who assisted me over the course of the last two years. In particular, I would like to acknowledge medical physics resident Dr. Conor Shaw, Dr. Chris Thomas and Dr. Edwin Sham for all of their insight into the QA duties. Special thanks are also extended to Tanya Timmins and Angela Henry for all of the administrative assistance and to all of my professors.

I would also like to thank all of my fellow graduate students who have laughed, complained and even commiserated with me over the past two years. The students from the 2015 “cohort” (Allan Hupman, Ethan Avila, Christopher O’Grady, Nathan Murtha, Louis Jay and Wesley Smith) inspired me daily with their tenacity as we tackled the daily challenges of the coursework. Additionally, Parisa Sadeghi, Courtney Henry, Emma Shouldice, Lin Ling and Amirreza Abbasnejad were supportive, funny and encouraging labmates throughout the project.

Early into the thesis-writing, I fractured my right ankle during one of my regular soccer matches and was forced to use crutches and a compression boot for a week and a half. My parents transported me to and from the office extremely frequently over this period of time and went out of their way to help me succeed when all of my life circumstances seemed bleak. I’m appreciative beyond words. Finally, I would like to thank all of my friends from the Halifax PLAYS soccer and volleyball leagues, who helped me have fun and contributed to my work-life balance.

CHAPTER 1 INTRODUCTION

1.1 Prostate Cancer

1.1.1 Canadian Cancer Society 2017 Statistics

In 2017, the Canadian Cancer Society estimated that one in two Canadians (1 in 2.2 females and 1 in 2 males) will develop cancer in their lifetimes (0-90+ years of age) [1]. The probability of developing a particular cancer is a multivariate function that is dependent upon distributions in population demographics, life expectancies and risk factors (including smoking and obesity rates) [1]. The rapid acceleration in the proportion of seniors within the total Canadian population (estimated to be 15.9% in 2016, constituting 5.9 million Canadians [2]) is also noteworthy, as cancer is intimately correlated with aging.

Half of the 206,200 expected new cases of cancer in Canada in 2017 were expected to be diagnosed as prostate, breast, lung and colorectal cancers [1]. Prostate cancer is the leading cancer in men, representing 20.7% of male cancers and 10% of cancers overall [1]. One in seven men are expected to develop prostate cancer over the course in their lifetime [1]. Furthermore, it is estimated that more than 95% of prostate cancers are adenocarcinomas [3].

1.1.2 Prostate Gland

The prostate is a walnut-sized gland located anteriorly to the rectum and inferiorly and posteriorly to the bladder [4]. It surrounds the upper part of the urethra, a tube that carries urine from the bladder to the penis and out of the body [4]. It is estimated that 50-80% of prostate cancers involve the apex of the prostate [3]. While normal prostates are mostly composed of homogeneous tissue, many men have heterogeneities called calcifications dispersed throughout the gland.

Prostate volumes generally range from 15cc to 30cc for healthy adult males, but the prostate size and shape alters as a man ages [5]. Furthermore, prostate volumes can even exceed 100 cc for both asymptomatic men and men with prostate cancer [6]. As prostates are close to the urinary and reproductive systems, symptoms of prostate cancer can

include urinary dysfunction, painful ejaculation, erectile dysfunction, incontinence and loss of bowel control [7].

1.2 Treatment Options

While a plethora of treatment and management options are available at contemporary cancer centers, the choice for a particular patient often depends upon several factors. One consideration is the prostate specific antigen (PSA) level that is measured during blood tests at the time of diagnosis [4]. PSA is a protein that is created by normal cells in the prostate and can be found in seminal fluid and in the blood of healthy men [4]. Additionally, clinicians must consider the grading and staging of the prostate cancer. For prostate adenocarcinoma, the Gleason score is used to grade the cancer and is computed by assigning grades out of 5 to the primary and secondary cancers based upon the underlying cell morphology observed under a microscope and summing the scores [4].

The American Joint Committee on Cancer (AJCC) TNM tumour staging system uses three series of categories (designated T, N and M), along with the PSA level at the time of diagnosis and the Gleason score, to classify the tumour's progression [8]. The groups associated with the AJCC staging system (7^{th} edition, 2010) are described in Table 1, while clinical definitions of the T, N and M categories can be found in Appendix A. Furthermore, the D'Amico risk group classification system uses the PSA level, Gleason score and T category in order to assess the likelihood of tumour recurrence for a given patient [9]. The risk is classified as low-risk, intermediate-risk or high-risk using this system (Table 2) [8] [9].

1.2.1 Active Surveillance

In active surveillance, a patient defers immediate treatment for prostate cancer but still returns to the hospital for digital rectal exams and PSA blood tests every 3-6 months [3]. Annually or bi-annually, a repeat biopsy is performed to ensure that Gleason grade has not worsened [3]. While active surveillance eliminates negative side effects caused by other therapies, there is a risk for tumour progression and may increase subsequent side effects at a future point in time [3]. That said, active surveillance is a viable option for

men with low risk prostate cancer or men who have other medical conditions (such as severe heart disease) that could be complicated during other treatments [9].

Table 1 The American Joint Committee on Cancer (AJCC) TNM tumour staging system for prostate cancer (7th edition, 2010) [3]. T refers to the primary tumour classification, N refers to the regional lymph nodes classification, and M refers to the distant metastases classification. The prostate-specific antigen reading (ng/mL) is also taken into consideration, along with the Gleason score. X indicates that a reading was unable to be assessed or simply unassessed.

Group	T	N	M	PSA	Gleason
I	T1a-c	N0	M0	PSA < 10	Gleason ≤ 6
IIA	T2a	N0	M0	PSA < 10	Gleason ≤ 6
IIB	T1-2a	N0	M0	PSA X	Gleason X
III	T1a-c	N0	M0	PSA < 20	Gleason 7
IV	T1-ac	N0	M0	10 ≤ PSA < 20	Gleason ≤ 6
	T2a	N0	M0	PSA < 20	Gleason ≤ 7
	T2b	N0	M0	PSA < 20	Gleason ≤ 7
	T2b	N0	M0	PSA X	Gleason X
	T2c	N0	M0	Any	Any
	T1-2	N0	M0	PSA ≥ 20	Any
	T1-2	N0	M0	Any	Gleason ≥ 8
	T3a-b	N0	M0	Any	Any
	T4	N0	M0	Any	Any
	Any	N1	M0	Any	Any
	Any	Any	M1	Any	Any

Table 2 The D'Amico risk group classification criteria for prostate cancer [9].

Risk Classification	Criteria
Low Risk	-Gleason < 6 and PSA < 10 -T1c or T2a
Intermediate Risk	-Gleason 7 or 10 ≤ PSA ≤ 20 -T2b
High Risk	-Gleason > 8 or PSA > 20 or T2c or T3

1.2.2 Radical Prostatectomy

In radical prostatectomy, the entire prostate gland, the seminal vesicles and part of the urethra within the prostate are surgically removed (along with the pelvic nodes if appropriate) [10]. Radical prostatectomies are a viable option for all stages of prostate cancer and can be combined with other modalities, including radiation therapy [10]. However, the recovery of erectile function post-surgery is dependent upon the nerve-sparing techniques used during surgery [3] [4] [11].

1.2.3 Androgen Deprivation Therapy

Androgen deprivation therapies are used to suppress the activities of androgens in the testicles and the adrenal glands that allow prostate cancer cells to grow [12]. These forms of therapy are usually considered for patients with stage III or stage IV prostate cancer, high-risk prostate cancer, or tumour recurrence [12]. Similarly, these therapies can be combined with other modalities (such as radiation therapy).

1.2.4 Radiation Therapy

Radiation therapy involves the use of ionizing radiation to damage the deoxyribonucleic acid (DNA) of cancerous cells and can be used to treat all stages of prostate cancer. Directly ionizing radiation (such as charged particles with a sufficient kinetic energy) produce ionization via collisions with matter [13]. Indirectly ionizing radiation (such as uncharged photons) produce directly ionizing particles while interacting with matter and are incapable of directly producing ionization during their collisions with matter. For this

type of radiation, ionization is accomplished by the secondary charged particles stemming from the indirectly ionizing radiation [13].

Two forms of radiation therapy for prostate cancer include external beam radiation therapy (EBRT) with a linear accelerator and brachytherapy. In EBRT, an external source of ionizing radiation is used to accelerate electrons to kinetic energies between 4 and 25 MeV. As a result, high-energy electron and photon beams can be directed towards the prostate from outside of the body [14]. This is contrasted to brachytherapy, which involves the placement of a sealed radioactive source in close vicinity to the tumour site [14].

1.3 Brachytherapy

Brachytherapy (derived from the Greek prefix *brachys*, meaning "short") involves the placement of encapsulated radioactive sources near well-localized tumours [14] [15]. An estimated 5-15% of all cancer patients receiving radiotherapy are suitable candidates for brachytherapy in an average radiation therapy clinic [16]. Table 3 summarizes some of the major potential contraindications that can exclude a patient from brachytherapy treatments, while Table 4 considers the indications for performing brachytherapy as a monotherapy or a boost [17].

Table 3 A selection of contraindications and possible contraindications for prostate brachytherapy procedures [17].

Contraindications [17]	Possible Contraindications [17]
Ataxia telangiectasia	Previous pelvic radiotherapy
Pre-existing rectal fistula	Limited life expectancy (< 10 years)
Distant metastases	Inflammatory bowel disease

Contraindications [17]	Possible Contraindications [17]
Large defects associated with transurethral resection of the prostate	High International Prostate Symptom Score (> 20), indicating moderate or severe urinary symptoms
Lack of rectum	Large prostate (> 60 cc)
	Large median lobes
	Pubic arch interference

Table 4 A selection of indications for prostate brachytherapy procedures [17].

Indications [17]	Possible Brachytherapy Procedures [17]
Low-risk prostate cancer	Monotherapeutic brachytherapy
Intermediate-risk prostate cancer	Brachytherapy, either as a boost or as monotherapy
High-risk prostate cancer	Brachytherapy, with a boost preferred over monotherapy

1.3.1 Implantation Types

Implants can be broadly classified based upon the location of the source applicators, as they can be placed within the tumourous tissue (interstitial brachytherapy), within a body cavity near the tumour volume (intracavitary brachytherapy), within molds or plaques directly over the tumourous tissue (surface brachytherapy), within a lumen (intraluminal

brachytherapy) or within the blood vessels of small or large arteries (intravascular brachytherapy) [14] [16]. Additionally, intraoperative brachytherapy involves irradiating a tumour bed during a surgical procedure [16].

Examples of sites for interstitial brachytherapy include the breast, prostate, and head and neck, whereas intracavitary brachytherapy can be used for gynaecological and rectal cancers. Surface brachytherapy is used for the skin while esophageal and lung sites are treated during intraluminal brachytherapy. The breast is also a site commonly used for intraoperative brachytherapy.

1.3.2 Loading Approaches

Brachytherapy procedures are also classified based upon the manner in which the radioactive sources are placed into the applicators. In earlier implementations of brachytherapy, applicators were pre-loaded with the radioactive sources prior to surgical placement (a method referred to as *hot loading*) [18]. This introduced significant radiation safety concerns, as medical and support staff were regularly exposed to high doses of radiation [18]. While handling and preparing sources, appropriate shielding was required and personal dosimeters were essential. That said, hot loading is still used for low dose rate (LDR) permanent prostate implants.

The development of afterloading applicator systems (most notably by Henschke in 1960) led to an innovative new technique for source placement called *manual afterloading* [18]. In manual afterloading, applicators were typically placed in close proximity to the target volume with dummy sources in place in order to calculate the implant dosimetry from radiographic images [18]. After verifying applicator placement, staff would manually replace the dummy sources with radioactive sources that were prepared separately and inserted within the treatment room [18]. While this still represented a radiation safety hazard, staff members were no longer responsible for confirming applicator placement while the sources were already in position.

More recently, remote-controlled afterloading devices have been developed that virtually eliminate staff exposure. Modern afterloaders consist of an irradiation device (located within the treatment room of the brachytherapy suite) and a control unit (located within

the control room of the brachytherapy suite) [19]. The irradiation device is a shielded vault containing the radioactive source that is remotely controlled using the control unit. Since the source is attached to a driving cable source coupled to a stepping motor, it can be transported mechanically through transfer tubes attached to the irradiation device to particular dwell positions within a catheter channel [19]. The irradiation device used at the Nova Scotia Cancer Center (NSCC) is the 30-channel microSelectron high dose rate (HDR) unit, shown in Figure 1 with transfer tubes attached.

Figure 1 The microSelectron HDR remote afterloader (Elekta, Stockholm, Sweden).

Using an *automatic remote afterloading* approach in the clinic also provides dosimetric benefits compared to hot loading procedures. The increased flexibility in source positioning, coupled with the computerized optimization of dwell times, led to the development of highly adaptive conformal treatment plans that escalate the dose to the required target volume while simultaneously sparing nearby organs at risk (OARs) [19]. Once optimized, treatment plans could thus be administered without direct human intervention.

1.3.3 Dose Rates and Implant Durations

Brachytherapy implants are also classified based upon the dose rate at a dose specification point and the duration of the implant. ICRU (International Commission on Radiation Units and Measurements) Report No. 38 (ICRU-38) defines a *low dose rate*

(LDR) treatment as one that delivers a dose rate of 0.4-2 Gy/h at the specification point [14] [20]; examples of sources used in manually or automatically afterloaded LDR brachytherapy include ^{125}I, ^{103}Pd and ^{131}Cs (Table 5 in Chapter 2), although LDR treatments of head and neck cancers can also be performed using ^{192}Ir wires that are cut to ensure the dose rate falls within the defined range [14]. For ^{125}I and ^{103}Pd, treatment dose rates can be as low as 0.01-0.3 Gy/h and are often used to provide a high total dose over the course of weeks or months [14]. *Medium dose rate* (MDR) treatments have dose rates of 2-12 Gy/h at the dose specification point, but MDR procedures are seldom utilized clinically [14] [19]. Furthermore, a *high dose rate* (HDR) treatment is defined as one that exceeds 12 Gy/h at the specification point; these treatments are delivered exclusively using a remote controlled HDR afterloader, with ^{192}Ir, ^{60}Co, and ^{169}Yb being common radionuclides [14] [19]. LDR brachytherapy afterloaders typically use multiple sources to achieve the requisite dose rate, whereas HDR afterloaders involve a single source.

One other treatment predicated upon variations in dose rate is not addressed in ICRU-38. *Pulsed dose rate* (PDR) brachytherapy treatments typically involve administering a lower activity HDR source (such as a 37 GBq ^{192}Ir source) in small fractions (lasting approximately 10-30 minutes) hourly over the course of a few days [21]. While cellular damage has not been fully repaired between fractions, PDR treatments achieve a similar radiobiological effect to LDR treatments [21].

In *temporary* brachytherapy treatments, the implantation occurs only for a definite period of time until the prescribed dose has been reached [14]. This is common for treatments involving ^{192}Ir and ^{137}Cs. However, *permanent* brachytherapy implants are placed indefinitely as the source decays [14].

1.3.4 Boosts, Focal Therapy and Monotherapy

HDR brachytherapy treatments can be used as a conformal dose escalation (or boost) to EBRT. Hypofractionated HDR brachytherapy boosts, as performed at the NSCC, may even offer distinct radiobiological advantages for treating prostate adenocarcinoma. A cell's sensitivity to radiation is quantified by the ratio α/β (with units Gy), where α takes

into account irreparable cell damage (proportional to the total dose D) and β takes into account cellular damage that can be ameliorated (proportional to the squared dose D^2) [22] [23]. In a recent review involving 21 independent studies, α/β was estimated to be 1.3 Gy for rapidly proliferating prostate adenocarcinoma cells [22] [23]. This is a value that is lower than the 3 Gy α/β ratio required for late rectum complications. As a result, prostate adenocarcinoma cells should be susceptible to all hypofractionated schemes that involved an increased fraction size and dose rate [23]. Hence, late normal-tissue complications can theoretically be held constant while greater prostate adenocarcinoma cell kill can be achieved using an HDR brachytherapy boost [23] [24].

Focal HDR brachytherapy is often used for patients with recurrence after previous radiation treatments. Using this technique, dose is prescribed to the site of local recurrence instead of the entire prostate gland in order to avoid side effects like erectile dysfunction and rectal toxicity [25]. This can be generally classified as hemi-focal (restricted to half of the prostate gland) or ultra-focal (restricted to an identified lesion with a margin) [25]. As images acquired using magnetic resonance imaging (MRI) are capable of distinguishing intraprostatic lesions, focal therapies are commonly performed in brachytherapy suites equipped with MRI scanners. T2-weighted, fast-spin-echo sequences are commonly utilized in MRI-planned brachytherapy [26]. The peripheral zone of the prostate (composed predominantly of water) appears more intense than the central gland, and thus many lesions can be identified from abnormalities in intensity within the peripheral zone [27]. Intraprostatic lesions can also be identified using multiparametric MRI, registering the T2-weighted images with diffusion-weighted images and dynamic contrast-enhanced MRI images [28].

HDR prostate brachytherapy with ^{192}Ir has also been used as a monotherapy for low-risk prostate cancer treatments in some centers [24]. In a recent study at the Willliam Beaumont Hospital (Royal Oak, Michigan), the outcomes of 65 patients treated with this technique were compared to the outcomes of 84 patients that were treated with monotherapeutic LDR permanent treatments using ^{103}Pd seeds [24]. The administered LDR dose was 120 Gy in one fraction while the HDR dose was 38 Gy delivered in two daily fractions over the course of two days. The same biochemical control was achieved

with both approaches, but monotherapeutic HDR brachytherapy treatments led to decreased acute urinary frequency and rectal pain compared to the LDR treatment [24].

1.4 Uncertainties in Brachytherapy

A calibrated brachytherapy source must be traceable to a national standards laboratory [14]. This typically involves measurements of a source's strength, quantified by the air-kerma strength S_K (discussed more thoroughly in Chapter 2). For high-energy HDR sources like ^{192}Ir, the uncertainty associated with S_K values calibrated in a primary standards laboratory is typically 2.2% [29]. Secondary calibrations within the clinic are typically done using a well type ionization chamber and should be within ±3% [30]. The magnitude of the S_K uncertainty is important to keep in mind, as S_K is a parameter involved in all dose calculations.

The overall accuracy of a particular dose calculation is also of concern in this study. The American Association of Physicists in Medicine (AAPM) Task Group Report 56 recommends that computer-assisted dose calculations have an overall accuracy of ±2% relative to the input data and algorithm used [30]. The report also recommends the performance of quality assurance tests to confirm that the positional accuracy of the source is within ±1 mm and that the temporal accuracy of all source dwell times is within ±2% [30]. Physical dose delivery accuracy should be within 5-10% of the calculated distribution [30].

1.5 HDR Brachytherapy at the Nova Scotia Cancer Center

At the NSCC, intermediate and high-risk prostate cancer patients may receive a temporary ^{192}Ir HDR brachytherapy implant with a prescription dose of 15 Gy to the prostate. This typically serves as a boost, preceding an additional prescription dose of 37.5 Gy to the prostate that the patients receive during 15 fractions of EBRT over three weeks. High-risk patients that require lymph node irradiation are treated with 46 Gy in 23 fractions of EBRT. The prescription and dose constraints for ^{192}Ir HDR brachytherapy are based upon the boost policy established by Morton *et al*. at Sunnybrook Odette Cancer Center in Toronto [31].

In the operating room of the NSCC brachytherapy suite, the patient is administered general anaesthesia and placed in the dorsal lithotomy position [28]. Subsequently, a transrectal ultrasound (TRUS) transducer attached to a stepper is used to acquire real-time 3D images of the patient's prostate gland [28]. The anterior-posterior angle of the probe may also be adjusted to allow for better contact with the anterior rectal wall, resulting in images with minimal artifact due to air pockets. These images ultimately guide the placement of catheters for the HDR brachytherapy implant. A Foley catheter, which was inserted into the urethra to drain urine from the bladder prior to image acquisition, allows for better visualization of the urethra when contouring structures during the treatment planning step.

Real-time TRUS imaging offers a number of distinct clinical benefits over computed tomography (CT) images. During TRUS-planned HDR brachytherapy, the image-guided catheter insertion process and treatment planning are performed within the same treatment room while the patient is anaesthetized [31]. By comparison, treatment planning with CT imaging would involve awakening the patient for transportation to a CT scanner outside of the treatment room and investigating any potential catheter displacement that could occur during this process. [31] This ultimately prolongs the procedure. While MRI-planned HDR brachytherapy is able to detect intraprostatic legions to boost dose to defined segments of the prostate for focal brachytherapy, HDR prostate brachytherapy treatments at the NSCC are for the whole-gland and do not require these capabilities.

At the NSCC, flexible bevel-tipped OncoSmart ProGuide plastic needles (Elekta Brachytherapy Solutions, Veenendaal, The Netherlands) were chosen for insertion into the prostate template (Figure 2) to circumvent more prominent imaging artifacts that may be caused by the use of rigid steel or titanium catheters. The plastic catheters also have a smaller "dead" space (the distance from the end of the catheter to the first dwell position) of 0.6 mm compared to the 1.0 mm "dead" space for metal needles. In general, the placement of each individual catheter is not optimized but rather selected by considering general catheter arrangements that have resulted in the requisite dose coverage and OAR sparing in patients with similar prostate dimensions [31]. Minor deviations from the

general catheter arrangement, if required, are typically motivated by patient-specific insertion issues or dosimetric concerns stemming from atypical OARs.

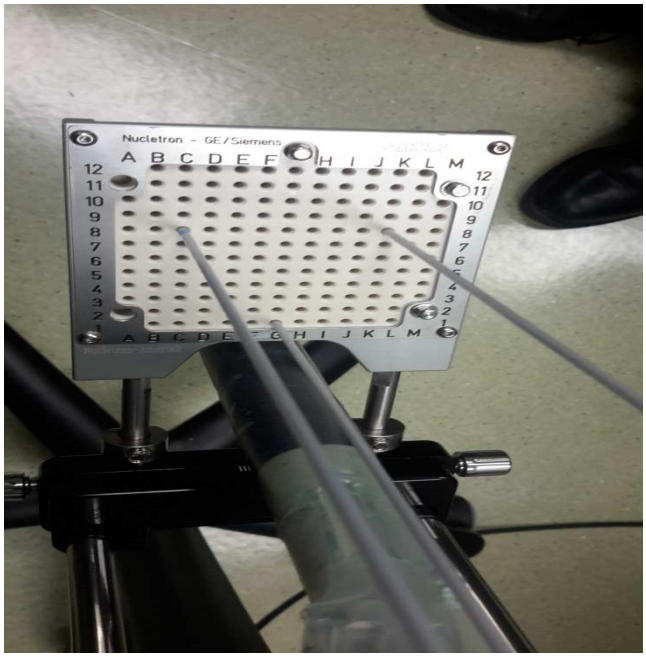

Figure 2 Plastic catheters are inserted into the HDR prostate template (Nucletron B.V., Veendendaal, The Netherlands) during TRUS-guided catheter placement.

Care should also be taken when selecting the number of catheters used for a particular treatment. Using only a few catheters can ultimately reduce the conformity of the dose distribution to the target volume and result in pronounced dose heterogeneities, while too many catheters may unnecessarily traumatize the patient post-surgery [31].

After the catheter insertion process is complete, a second 3D TRUS image is acquired using the brachytherapy stepper with all catheters in place [28]. To ensure source positions can be localized correctly during treatment planning, each needle tip position must be identified within the TRUS image and accurately determined. Given the low resolution of TRUS images, this task is more easily accomplished by measuring the length of each catheter protruding from the template (Figure 2) and subtracting that from the known total needle length. This calculation is thus a surrogate for needle tip position. These measurements are typically made with a ruler and entered into both the Oncentra Prostate treatment planning system (Elekta Brachytherapy Solutions, Veenendaal, The

Netherlands) and an independent written recording sheet for quality assurance (QA) purposes [28]. This procedure is often double-checked and independently measured by multiple members of the radiation therapy team to ensure values are accurate. Following these measurements, the target and OARs are contoured on transverse slices by a radiation oncologist.

Using Oncentra Prostate (Elekta Brachytherapy Solutions, Veenendaal, The Netherlands), needles are then reconstructed by an attending medical physicist. This involves observing the appearance of needles from the TRUS images and ensuring that the needle tip and first dwell position for a given catheter (represented by coloured indicators superimposed over the TRUS images by the treatment planning system) are consistent with the image [28].

Following catheter reconstruction, treatment plan optimization is performed using the Dose-Volume Histogram Optimization (DVHO) algorithm implemented in Oncentra Prostate (Elekta Brachytherapy Solutions, Veenendaal, The Netherlands). While DVHO-generated plans are susceptible to extreme differences between dwell times which could result in hots spots or under-dosed regions within the planning target volume (PTV), Nucletron recently introduced a Dwell Time Deviation Constraint that alleviates this dosimetric concern [28].

After an acceptable treatment plan has been generated by Oncentra Prostate (Elekta Brachytherapy Solutions, Veenendaal, The Netherlands), all involved staff can leave the treatment room while the source is remotely afterloaded from the safe to the planned dwell positions within the catheters. If there are no complications following treatment, planning CT images for fractionated EBRT are acquired within 24 hours.

1.6 Specific Aims

Recent LDR brachytherapy studies have focused on prostate calcifications, heterogeneities with a high atomic number Z that are often present in prostate glands with prostate adenocarcinoma. More precise information on the composition of prostate calcifications and methods for modeling them will be considered later in this thesis.

Nevertheless, there is some indication that these materials result in moderate reductions to clinical dose metrics associated with local tumour control, such as the prostate D_{90} and V_{100}, compared to metrics calculated in a strictly water-based geometry using AAPM's Task Group 43 (TG-43) dose calculation formalism [31] [32] [33]. While this dose calculation formalism is discussed more thoroughly in the next chapter, it is worthwhile noting that TG-43 remains the current clinical standard and is widely adopted worldwide [31][32][33]. To date, however, limited research has been conducted into the effects of prostate calcifications in contexts related to HDR brachytherapy.

This thesis investigates the dosimetric consequences of modeling prostate calcifications in the vicinity of an ^{192}Ir HDR source for both a water reference medium and a series of patient-specific prostate phantoms. This work is entirely computational in nature and involves the use of EGSnrc and its C++ class library (egspp), software for modeling the transport of photons and charged particles within a user-defined geometry [34] [35]. Furthermore, the vast majority of the research analysis has been performed using MATLAB (The MathWorks, Inc., Natick, Massachusetts, U.S.A.). While more specific hypotheses of the thesis are formulated in Chapter 4 after a thorough review of the requisite physics involved, the objectives of the thesis are as follows:

1. *Develop a Monte Carlo (MC) platform for performing dose calculations related to HDR brachytherapy.* While the current work is focused on the influence of calcifications in prostate brachytherapy, the code developed should be well-documented, user-friendly and the basis for future work involving other anatomical sites.
2. *Validate the microSelectron-v2 ^{192}Ir source (Nucletron B.V., Veendendaal, The Netherlands) by calculating essential TG-43 dosimetric parameters*. To ensure that the source is being modeled correctly, the dose rate constant Λ is calculated along with the radial dose function $g(r)$ and anisotropy functions $F(r,\theta)$ using MC simulations.
3. *Investigate the dosimetric effects of introducing a prostate calcification to an ^{192}Ir source within a water phantom.* Using a voxelized water phantom with an embedded calcification and a pure water voxelized phantom, effects are

quantified by considering (a) 2D axial dose differences passing through the calcification center and (b) dose profiles through the calcification center in the transverse, coronal and sagittal planes.

4. *Perform a patient-specific dose calculation using ^{192}Ir for an HDR prostate brachytherapy patient with a prostate calcification and compare clinical metrics to the TG-43 dose calculation formalism.* The calculation should not be affected by interseed attenuation, as the procedure involves a single ^{192}Ir translated through catheters to the given dwell positions. However, there are challenges involved with deformably registering TRUS images with CT images containing latent electron density information and adapting a software that is commissioned to only use ultrasound imaging. Hence, the patient's HDR prostate brachytherapy plan is created using the planning CT acquired before EBRT and planned using Oncentra Brachy (Elekta Brachytherapy Solutions, Veenendaal, The Netherlands). Calculations will involve extracting the density information from those CT images and assigning materials to voxels within a numerical virtual patient phantom.

1.7 Thesis Outline

This thesis has been organized into six additional chapters and a series of appendices.

- Chapter 2 summarizes all aspects of HDR brachytherapy dosimetry involving ^{192}Ir, including all of the relevant photon interactions with matter, ^{192}Ir source characteristics, TG-43 dose calculation formalism and limitations, and the recommendations for model-based dose calculation algorithms (MBDCAs) from the AAPM Task Group 186 (TG-186) [31] [32] [33] [36].
- Chapter 3 reviews the methodologies and key concepts underlying MC simulations for radiation transport, with particular emphasis placed on the use of egspp.
- Chapter 4 discusses the composition and properties of prostate calcifications and reviews the methods that have been taken to model calcifications in the context of LDR brachytherapy.

- Chapter 5 is dedicated to the methods that have been utilized in the current work, while Chapter 6 consists of a thorough discussion of the relevant results stemming from this project.
- Finally, Chapter 7 states the key research contributions made in the present study, assesses the clinical utility of the work and proposes avenues for future research.

CHAPTER 2 HDR BRACHYTHERAPY DOSIMETRY USING ^{192}IR

2.1 Introduction

In this chapter, the fundamental radiometric quantities and photon interactions pertinent to ^{192}Ir dosimetry will be introduced, along with the concept of charged particle equilibrium. This serves as a preface to additional discussions on the dose calculation formalism developed by Task Group No. 43 of the AAPM Radiation Therapy Committee and the recent recommendations for early adopters of more sophisticated model-based dose calculation algorithms by AAPM's Task Group No. 186 (TG-186) [31] [32] [33] [36].

2.2 Photon Interaction Processes

The attenuation and scatter of γ-rays produced within the core of an ^{192}Ir source is primarily governed by three photon interaction processes: *the photoelectric effect*, *Compton (incoherent) scattering* and *Rayleigh (coherent) scattering* from atoms [13]. *Pair production* – a process in which an incident photon vanishes near the Coulomb field of a nucleus and creates an electron-positron pair – can be neglected for ^{192}Ir, as the shielded photon spectrum rarely exceeds the threshold energy of 1.022 MeV required for the process to occur [37]. After each process is explained kinematically, the scenarios in which each interaction becomes important will be discussed.

2.2.1 Rayleigh (Coherent) Scattering

Rayleigh (coherent) interactions involve the elastic scattering of photons (of energy $h\nu$) with a bound orbital electron [13]. As the energy losses are insignificant during this process, the scattered photon retains the original energy $h\nu$ and the entire atom recoils by an insignificant amount to conserve momentum [13]. As no secondary particles are given kinetic energy during this process, no energy is deposited resulting from Rayleigh scattering [37].

2.2.2 Photoelectric Effect

In the *photoelectric effect* (also referred to as *photoabsorption*), a photon of energy $h\nu$ is absorbed entirely during a collision with an electron bound in an inner orbital shell of an atom with binding energy E_b (strictly provided that $h\nu > E_b$) [13] [37]. Subsequently, the electron is scattered at a planar angle θ relative to the trajectory of the incident photon with kinetic energy T:

$$T = h\nu - E_b \qquad (1)$$

While the recoiling atom's planar angle ϕ (constrained within $0° < \phi < 180°$) ensures that momentum is conserved during the interaction, its kinetic energy T_a is generally orders of magnitude smaller than T and therefore negligible [13].

Whenever an orbital shell electron is ejected, this vacancy is filled by an electron falling from an outer shell during a process called *atomic de-excitation* [13]. Vacancies within the K- and L- shells can result in the emission of fluorescent x-rays (with an energy equal to the energy difference between the shell with the vacancy and the shell from which the electron moves) [37]. Fluorescence emission associated with each shell vacancy is governed by a probability called the fluorescence yield (designated Y_K or Y_L for K- and L-shells) [37]. The fluorescence yield is generally a function of the atomic number Z [37]. While fluorescence x-ray emission is highly probable for K-shell photoabsorption events in high-Z materials ($Y_K \sim 1$), fluorescent x-rays associated with L-shell photoabsorption events occur far more infrequently (Y_L = 0.42 for Z = 90) [37]. None of the energy associated with the fluorescent x-ray is converted to electron kinetic energy [37].

Auger electron emission involves the ejection of electrons from exterior shells to occupy the vacancy in an interior shell [37]. The energy of Auger electrons is equal to the difference between the energy levels of the shells. An electron cascade can result as electrons from more remote shells occupy these vacancies, halting only when conduction-band electrons resolve the outermost electron vacancies (with energy equal to the outer shell binding energy) [37]. Whenever Auger electrons fill a vacancy, the binding energy associated with the shell of the vacancy is converted to electron kinetic energy [37].

2.2.3 Compton (Incoherent) Scattering

Compton scattering processes involve the interaction of a photon (of energy $h\nu$ and momentum $\frac{h\nu}{c}$) with an atomic electron (of binding energy $E_{binding} << h\nu$) [37]. To a first order approximation, these electrons are assumed to be both stationary and unbound and thus have no inherent kinetic energy or momentum [37]. As a result of the collision, the photon is scattered at an angle ϕ with respect to the photon's initial trajectory and assumes a new lower energy $h\nu'$ and momentum $\frac{h\nu'}{c}$ [37]. Additionally, the Compton recoil electron is sent along a trajectory with angle θ carrying momentum $p = mv$ and kinetic energy $T = mc^2 - m_0c^2$ (where m_0 is the electron's rest mass, v is the electron's velocity and $m = \frac{m_0}{\sqrt{1-(\frac{v}{c})^2}}$ is the electron's relativistic mass) [37].

Conservation of momentum and energy can be used to derive T and $h\nu'$, which is conventionally expressed in terms of the incident photon energy $h\nu$ and the photon scatter angle ϕ:

$$h\nu' = h\nu \frac{1}{1+(\frac{h\nu}{m_0c^2})(1-\cos\phi)} \tag{2}$$

$$T = h\nu - h\nu' = h\nu \frac{(\frac{h\nu}{m_0c^2})(1-\cos\phi)}{1+(\frac{h\nu}{m_0c^2})(1-\cos\phi)} \tag{3}$$

The recoil angle θ can be determined similarly through the following derived relation:

$$\cot\theta = \left(1 + \frac{h\nu}{m_0c^2}\right)\tan(\frac{\phi}{2}) \tag{4}$$

For all low-energy (< 0.01 MeV) incident photons, the recoil electron kinetic energy T is essentially negligible and $h\nu \cong h\nu'$; this limiting scenario is termed *elastic Thomson scattering* [37]. For energies exceeding 0.01 MeV, T becomes appreciable. Regardless, the precise energy imparted to the electron T depends upon the photon scattering angle ϕ. $T$is maximized for complete photon backscatter ($\phi = 180°$ and cos ϕ = -1), while T = 0 MeV for straight-ahead scattering ($\phi = 0°$ and cos ϕ = 1) [13]. The Compton formalism also reveals a strong dependence on the magnitude of the incident photon energy $h\nu$, as a 1 MeV photon transfers approximately 80% of its energy to T while a 60 keV photon transfers approximately 19% of its energy to T [13].

2.2.4 Probability of Interaction Processes

In order to quantify the probability of each interaction process, it is useful to introduce the linear attenuation coefficient μ and mass attenuation coefficient $\left(\frac{\mu}{\rho}\right)$. For a monoenergetic parallel beam of N photons traversing through a medium with infinitesimal thickness dl, dN photons will interact with the medium on average [13]. The product $\mu \cdot dl$ is defined as the probability that a particle traversing a medium of thickness dl interacts within it, where μ is given in the following expression:

$$\mu = \frac{1}{dl}\frac{dN}{N} \tag{5}$$

μ is typically expressed with units of cm^{-1} and also be considered the number of interactions per unit length [37]. As μ depends upon the density ρ of the attenuating material, it is more useful to consider the mass attenuation coefficient $\left(\frac{\mu}{\rho}\right)$ derived by simply dividing μ by ρ [37]. Hence, the units of $\left(\frac{\mu}{\rho}\right)$ are typically $cm^2\ g^{-1}$.

In this thesis, the total mass attenuation coefficient $\left(\frac{\mu}{\rho}\right)$ is defined as the sum of the mass attenuation coefficients attributable to Rayleigh scattering, Compton scattering and the photoelectric effect [13]. These are designated $\left(\frac{\sigma_R}{\rho}\right)$, $\left(\frac{\tau}{\rho}\right)$ and $\left(\frac{\sigma}{\rho}\right)$, respectively [37].

For a material with atomic number Z, the mass attenuation coefficient for Rayleigh scattering $\left(\frac{\sigma_R}{\rho}\right)$ is approximately proportional to $\frac{Z}{(h\nu)^2}$. [37]. While this relationship suggests that Rayleigh scattering gains importance in scenarios involving low-energy photons and high-Z materials, $\left(\frac{\sigma_R}{\rho}\right)$ values can be two or three orders in magnitude lower in high-Z materials compared to the mass attenuation coefficient for the photoelectric effect $\left(\frac{\tau}{\rho}\right)$ [13]. Hence, Rayleigh scattering events typically become more appreciable for low-Z materials such as water (the radiation transport media used in the TG-43 dose calculation formalism) relative to photoabsorption events provided the photon energy is sufficiently large enough (e.g. 60 keV for water) [13]. This increase in importance is largely attributable to the increased scattering angle of Rayleigh photons with Z and $h\nu$, but it is important to emphasize that Compton scattering ultimately dominates at large $h\nu$ [13].

For energies below 0.1 MeV, $\left(\frac{\tau}{\rho}\right)$ is approximately proportional to $\frac{Z^3}{(h\nu)^3}$ at energies above the K-edges [13]. Hence, photoabsorption dominates at low photon energies and in high-Z materials (such as the active core and encapsulation of a brachytherapy source or a high-Z heterogeneity like a calcification) [13]. While this is usually accompanied by increased fluorescent x-ray emission in high-Z materials (attributable to the increase in fluorescent yield with Z), these x-rays do not transfer their energy to electron kinetic energy [13].

The Compton mass attenuation coefficient $\left(\frac{\sigma}{\rho}\right)$ is derived from the Klein-Nishina cross section per electron (under the assumption that the interaction electrons are unbounded and stationary), and is approximately proportional to $(h\nu)^{-1}$ and independent of Z [37]. Compton scattering is the dominating photon interaction process governing energy absorption in soft tissues for photons with energies exceeding 60 keV (where the photoelectric effect is less important).

2.3 Radiometric and Dosimetric Quantities

2.3.1 Kerma

As uncharged photons penetrate through a medium, they transfer energy to directly ionizing, secondary charged particles during photoabsorption and Compton interactions with atoms of the medium. Kerma (the *kinetic energy released* per unit *mass*, designated K) is a dosimetric term that quantifies this liberation of energy by an indirectly ionizing radiation field and depends upon both the radiant energy R and a stochastic quantity called the energy transferred (designated ϵ_{tr}) [37].

The radiant energy R is defined as the cumulative energy of all particles, charged or uncharged, that is transferred, emitted or received [37]. Consequently, the energy transferred ϵ_{tr} in a volume V is expressed using the following formula:

$$\epsilon_{tr} = (R_{in})_u - (R_{out})_u^{nonr} + \Sigma Q \qquad (6)$$

ϵ_{tr} is computed by first evaluating the difference between the radiant energy of uncharged particles entering V, $(R_{in})_u$, and the radiant energy of uncharged particles leaving V, $(R_{out})_u^{nonr}$. The latter term excludes the contributions of uncharged particles stemming from the radiative losses of charged particles while in V. This difference is added to the net energy derived from rest mass in V, ΣQ [37]. Radiative losses occur during any process that involves the transformation of charged-particle kinetic energy to photon energy (namely bremsstrahlung or in-flight annihilation of positrons) [37]. More succinctly, ε_{tr} is the kinetic energy received by charged particles in V (excluding any energy transfer between charged particles) [37].

If P is a point of interest inside of the volume V, the kerma K at P in an infinitesimal volume dv with mass dm is defined as:

$$K = \frac{d\epsilon_{tr}}{dm} \qquad (7)$$

K is a measure of the expected energy ϵ_{tr} transferred to charged particles by uncharged particles per unit mass dm at the point P, and includes any of the radiative losses indicated earlier [37].

2.3.2 Collision Kerma

If one chooses to exclude the radiative-loss energy resulting from charged particles originating in V from ϵ_{tr}, designated R_u^r, then a quantity called the net energy transferred ϵ_{tr}^n can be defined as:

$$\epsilon_{tr}^n = \epsilon_{tr} - R_u^r \qquad (8)$$

ϵ_{tr}^n can be used to partition the kerma K into two components, designated K_c and K_r respectively [37]. K_c is referred to as the collision kerma and refers to the part of the kerma K involved in excitation and ionization events near the point P:

$$K_c = \frac{d\epsilon_{tr}^n}{dm} \qquad (9)$$

This is contrasted with K_r, referred to as the radiative kerma. K_r is the part of the kerma K involved in photon transport away from the point P and is usually calculated by simply taking the difference between the kerma K and the collision kerma K_c [37].

2.3.3 Absorbed Dose

The absorbed dose D is defined through a quantity called the energy imparted ϵ [37]. ϵ is defined with reference to a mass m within a volume V as the following:

$$\epsilon = (R_{in})_u - (R_{out})_u + (R_{in})_c - (R_{out})_c + \Sigma Q \qquad (10)$$

$(R_{in})_u$ and $(R_{in})_c$ represent the total radiant energy entering V from uncharged and charged particles, respectively, while $(R_{out})_u$ and $(R_{out})_c$ represent the total radiant energy leaving V from uncharged and charged particles [37]. Hence, D can be specified as the expected energy imparted per unit mass dm at a point P inside V:

$$D = \frac{d\epsilon}{dm} \tag{11}$$

Energy is imparted into matter during interaction events between ionizing radiation and the atoms of the medium.

The transfer of energy is mediated by the mass attenuation coefficient $\left(\frac{\mu}{\rho}\right)$, the mass energy transfer coefficient $\left(\frac{\mu_{tr}}{\rho}\right)$ and the mass energy absorption coefficient $\left(\frac{\mu_{en}}{\rho}\right)$. The latter two terms can be expressed with respect to $\left(\frac{\mu}{\rho}\right)$, which has been previously defined, and are a function of the photon energy hv and the atomic number Z of the medium [38]. $\left(\frac{\mu_{tr}}{\rho}\right)$ is defined as the product of the mass attenuation coefficient and the average fraction of the incident photon energy that is transferred to secondary electrons, $\left(\frac{\overline{E_{tr}}}{hv}\right)$:

$$\left(\frac{\mu_{tr}}{\rho}\right) = \left(\frac{\mu}{\rho}\right) \cdot \left(\frac{\overline{E_{tr}}}{hv}\right) \tag{12}$$

Moreover, $\left(\frac{\mu_{en}}{\rho}\right)$ is defined as the product of the mass attenuation coefficient and the average fraction of the incident photon energy that is absorbed in the medium $\left(\frac{\overline{E_{ab}}}{hv}\right)$:

$$\left(\frac{\mu_{en}}{\rho}\right) = \left(\frac{\mu}{\rho}\right) \cdot \left(\frac{\overline{E_{ab}}}{hv}\right) \tag{13}$$

These quantities are generally tabulated along with $\left(\frac{\mu}{\rho}\right)$ in most databases, including the NIST (National Institute of Standards and Technology) XCOM database used in this study [39].

2.3.4 Charged-Particle Equilibrium

For points in a homogeneous medium greater than 2 mm away from an ^{192}Ir source (with dimensions greater than the maximum range of secondary electrons), a condition called charged particle equilibrium (CPE) becomes relevant [29]. Under the assumption of CPE, the absorbed dose D at the point in this homogeneous region is approximately equal to the collision kerma K_c due to the uniformity of the radiation field [29]. Note that the CPE condition also requires that the photons involved have a large mean free path relative to the maximum range of the secondary electrons [29]. This is valid for all photon energies below 1 MeV, which applies for ^{192}Ir [29]. For distances smaller than 2 mm, the influence of the ^{192}Ir β-emissions becomes relevant and electronic equilibrium is not achieved [13].

As dose is typically scored with respect to voxels that are approximately the same size as CT image voxels, CPE exists near an ^{192}Ir source for all scoring voxels greater than 2 mm away [29]. While an interface will exist between voxels composed of different media, the effect of this interface on the resulting dose distribution can be considered negligible under CPE [29]. Hence, it is possible to disregard electron transport in Monte Carlo simulations and simply score the absorbed dose as collision kerma (Chapter 3).

2.4 Artificial Production of ^{192}Ir Sources

^{192}Ir is produced artificially from (n, γ) reactions generated within a nuclear reactor [13]. Stable target nuclei of ^{191}Ir capture bombarded neutrons with a probability equal to the activation cross-section [13]. This prompts the conversion to unstable ^{192}Ir* and its subsequent de-excitation to ^{192}Ir via the emission of γ-rays [13].

This process is inefficient for natural iridium (which consists of approximately 37.3% ^{191}Ir and 62.7% ^{193}Ir), as 1 in 10^6-10^9 target nuclei are activated per neutron flux produced in the reactor [13]. Hence, the overall product will have a low-specific activity due to the high concentrations of unactivated ^{191}Ir and unnecessary ^{193}Ir [13]. To generate higher specific activities, enriched ^{191}Ir is created by depleting natural iridium from its ^{193}Ir content and then irradiated [13]. Specific activity increases of up to 210% have been reported when enriched ^{191}Ir is irradiated for 85% of the original irradiation time used for natural iridium [13]. As iridium itself is very brittle, it is combined with soft platinum for stability prior to source production [13]. HDR ^{192}Ir sources are then encapsulated in stainless steel capsules and welded onto steel wires for use in a remote afterloader [13].

2.5 ^{192}Ir Source Characteristics

The set of feasible brachytherapy applications associated with a particular radionuclide (such as ^{192}Ir) can be assessed by analyzing the physical characteristics of the manufactured source.

2.5.1 Half-Life $T_{1/2}$

As radioactive decay is a stochastic occurrence, it is necessary to quantify the probability of decay dP for a given nucleus of a radionuclide per unit time dt. This is referred to as the *decay constant*, λ, and is conventionally expressed with units s^{-1}:

$$\lambda = \frac{dP}{dt} \tag{14}$$

The *half-life*, $T_{1/2}$, of the radionuclide is defined to be the time required for the number of unstable nuclei to be halved and depends upon λ:

$$T_{1/2} = \frac{\ln(2)}{\lambda} \tag{15}$$

^{192}Ir sources have a half-life $T_{1/2}$ of 73.81 days, which greatly exceeds the time required to ship the source to a clinic and the preparation time for implantation [13]. This half-life is also economically beneficial, as daily decay corrections are on the order of 1% [12]. While ^{192}Ir wires are often temporarily implanted as wires or needles in LDR treatments, the long half-life of ^{192}Ir accommodates temporary HDR treatments as well.

2.5.2 Specific Activity $A_{specific}$

For a radionuclide with half-life λ and number of nuclei $N(t)$ at time *t*, the *activity* $A(t)$ describes the number of decays at time *t*, designated $dN(t)$, observed per unit time dt:

$$A(t) = \frac{dN(t)}{dt} = \lambda N(t) \qquad (16)$$

$A(t)$ is expressed conventionally with units s^{-1}, called the becquerel (Bq) in contexts related to activity. To facilitate a comparison between radionuclides, a time-independent quantity called *maximum specific activity* is defined as the activity per molar mass as follows:

$$A_{specific} = \lambda \frac{N_A}{M} \qquad (17)$$

N_A is Avogadro's number (6.0221415×10^{23} mol^{-1}) and M is the molar mass of the radionuclide considered (with units of g mol^{-1}) [13]. The maximum specific activity is conventionally expressed with units of GBq mg^{-1}.

Since the molar mass of ^{192}Ir is 191.963 g mol^{-1}, ^{192}Ir sources have a high specific activity of 340.98 GBq mg^{-1} [13]. Hence, it is possible to miniaturize ^{192}Ir sources for use in remote afterloaders while still maintaining a high-dose rate for temporary implants.

2.5.3 Density and Atomic Number

For a radioactive source, the density and atomic number of the source core largely determine how isotropic the dose distribution is [13]. Since ^{192}Ir has an atomic number of 77 and a density of 22.42 g cm^{-3}, self-absorption occurs within the active core and creates an anisotropic dose distribution [13].

2.5.4 Air Kerma-Rate Constant Γ_δ

One common measure for specifying the strength of a γ-emitting brachytherapy source is the *air kerma-rate constant* Γ_δ (expressed with SI units as J $kg^{-1}m^2$) [13]. For a point source associating with a radioactive source located in a vacuum with activity A, Γ_δ is defined using the following formula:

$$\Gamma_\delta = \frac{r^2 \dot{K}_\delta}{A} \tag{18}$$

$\dot{K}_\delta$ is the air kerma rate in an air-filled volume at the distance r from the point source attributable to photons with energy exceeding the energy cut-off δ (usually 10 keV). If the point source is spherically symmetric, monoenergetic, and produces photons of energy E, the air kerma-rate $\dot{K}_\delta$ is given by the following expression:

$$\dot{K}_\delta = \psi \left(\frac{\mu_{tr}}{\rho}\right)_{E,air} = \left(\frac{1}{4\pi r^2}\right) AE \left(\frac{\mu_{tr}}{\rho}\right)_{E,air} \tag{19}$$

Γ_δ can then be formulated as:

$$\Gamma_\delta = \left(\frac{1}{4\pi}\right) E \left(\frac{\mu_{tr}}{\rho}\right)_{E,air} \tag{20}$$

This generalizes to the following expression for a point source with a photon spectrum with N energies, where n_i photons of energy E_i are emitted per disintegration:

$$\Gamma_\delta = \left(\frac{1}{4\pi}\right) \sum_i^N n_i E_i \left(\frac{\mu_{tr}}{\rho}\right)_{E_i,air} \tag{21}$$

This formulation for the air kerma-rate constant Γ_δ does not take into account the effects of source self-attenuation and the attenuating properties of the encapsulating material, and is strictly valid for point sources [13]. Furthermore, if the intermediate material is not vacuum, additional corrections for scatter and attenuation are required and non-negligible [13]. Nevertheless, the normalization by activity makes Γ_δ a reasonable metric for inter-source strength comparisons.

2.5.5 Energy Measures

Several energy metrics are commonly used to quantify a radionuclide's penetration power and the subsequent shielding requirements involved for the brachytherapy clinic. These include the *mean photon energy*, the *mean γ-ray energy,* the *effective energy* and the *half-value layer (HVL) of lead (Pb)* [13].

For a radionuclide with a photon spectrum consisting of N energies (where n_i photons of energy E_i are emitted per disintegration), the mean photon energy E_{mean} is defined as:

$$E_{mean} = \frac{\sum_i^N \ n_i E_i}{\sum_i^N \ n_i} \tag{22}$$

In general, photons leaving a radioactive source core include γ-rays emitted from the unstable nuclei, characteristic x-rays generated as charged particles change energy levels, and bremsstrahlung x-rays generated as charged particles are deflected near a nucleus and slow down [13]. All three types of radiation are included within E_{mean}, but a second metric called the mean γ-ray energy $E_{mean\,\gamma}$, only takes the γ-rays into account [13]. Hence, n_i is restricted to being the γ-ray count for energy E_i and the same formula applies.

Radiation penetrability is more suitably measured using the effective energy E_{eff}, defined as the air-kerma weighted mean energy:

$$E_{eff} = \frac{\sum_i^N \ n_i {E_i}^2 \left(\frac{\mu_{tr}}{\rho}\right)_{E_i,air}}{\sum_i^N \ n_i E_i \left(\frac{\mu_{tr}}{\rho}\right)_{E_i,air}} \tag{23}$$

By weighing each E_i contribution by its air-kerma rate constant, the penetrability assessed via the effective energy metric builds in source strength information [13].

A final metric for assessing radiation penetrability is the HVL for Pb, defined as the amount of thickness (in millimeters) required to halve the exposure rate [13].

By all measures, ^{192}Ir is a moderately penetrating radionuclide compared to others used in brachytherapy applications. The photons produced by an unfiltered ^{192}Ir core can range in energies from 61 to 137.8 keV (depending on the manufacturer), resulting in a mean photon energy of E_{mean} of 355 keV, a mean γ-ray energy $E_{mean\,\gamma}$ of 372 keV and an effective energy E_{eff} of 398 keV [13]. As these energy measures exceed 100 keV, the resulting dose distribution is usually homogeneous and not heavily influenced by photoabsorption-related inhomogeneities. Furthermore, the HVL is 3.0 mm Pb, which is comparable to the HVL of ^{198}Au (2.8 mm Pb) [13]. While ^{192}Ir also has a β-emission spectrum, it does not play a significant role beyond 2 mm past the encapsulated source [13].

2.5.6 Comparison to Other Radionuclides

Table 5 Source properties for a variety of radionuclides used in brachytherapy (adapted from [13]).

Isotope	$T_{1/2}$	E_{mean} [keV]	Maximum Specific Activity [GBq mg^{-1}]	Γ_δ [μGy h^{-1} MBq^{-1} m^2]	Typical Clinical Use
^{192}Ir	73.81 d	355	340.98	0.1091	Temporary
^{125}I	59.49 d	28	650.15	0.0348	Permanent and Temporary
^{103}Pd	16.99 d	21	2763.13	0.0361	Permanent
^{226}Ra	1600 y	830	0.0366	-	Temporary
^{60}Co	5.27 y	1253	41.91	0.3059	Temporary
^{137}Cs	30.07 y	615	3.202	0.0771	Temporary
^{198}Au	2.70 d	406	9055.12	0.0545	Permanent
^{169}Yb	32.02 d	93	893.29	0.0431	Permanent and Temporary
^{170}Tm	128.60 d	66	221.07	0.00053	Temporary

Table 5 summarizes the source properties for a variety of radionuclides, including ^{192}Ir, ^{60}Co, ^{137}Cs, ^{198}Au, ^{125}I, ^{103}Pd, ^{169}Yb and ^{170}Tm. For HDR brachytherapy sources like ^{192}Ir with high E_{mean} values, Compton scattering occurs frequently within low-Z media like soft tissue [36]. Hence, HDR brachytherapy dose calculations are highly dependent on scatter conditions [36]. This is to be contrasted with sources typically used for LDR brachytherapy (like ^{103}Pd and ^{125}I), which have lower E_{mean} values of 21 keV and 28 keV [13]. As lower energies increase the photoabsorption cross section, photoabsorption is generally of more concern in the physics of LDR brachytherapy [12]. Hence, care must be taken to ensure that tissue composition is defined accurately in LDR brachytherapy calculations (especially near high-Z media) [36]. It is important to emphasize, however, that self-absorption within the high-Z source core and encapsulation occurs in both LDR and HDR sources and is attributable to the increased photoabsorption cross-section for high-Z materials [13].

2.6 TG-43 Dosimetry Formalism

The aim of source dosimetry is to determine the distribution of dose surrounding a radioactive source within a given reference medium [13]. The earliest frameworks for source dosimetry were often based upon quantities related to radium, including the equivalent mass of radium for source strength specification, and were also independent of differences in source designs for the same radionuclide [13]. These significant limitations led to the development of the AAPM TG-43 dosimetry formalism for photon-emitting interstitial brachytherapy sources in 1995 (which was later updated in 2004) [30] [31] [32].

Under the TG-43 formalism, sources are defined as either ideal point sources (the *1D TG-43 approximation*) or as sources with a cylindrically symmetrical activity distribution (the *2D TG-43 approximation*) [13]. The former definition is typically used when source orientation information is unable to be assessed for all seeds involved (a scenario that occurs frequently in permanent LDR brachytherapy), while the latter definition is conventionally used for HDR brachytherapy. Irrespective of the source definition involved, TG-43 dose calculations involve the summation of dose distributions involving a single radioactive source in an effectively infinite water phantom to account for radiation scattering. While TG-43 calculations were originally designed for the use of LDR sources, it remains the current clinical standard for brachytherapy calculations involving HDR and PDR sources as well [13] [36].

Figure 3 shows the geometry associated with the TG-43 dose calculation formalism for an HDR brachytherapy source with a modeled driving cable. The source is assumed to be cylindrically symmetric. Observe that the tip of the source capsule is aligned with the +z direction and that the polar angle θ is defined as the angle of a point $P(r, \theta)$ with respect to the source's longitudinal axis at a radial distance r from the source's center. The formalism defines a reference position $(r_0,\ \theta_0) = (1\text{ cm},\ 90°)$ along the transverse bisector of the source. Using the updated TG-43 formalism, the distribution of the dose rate to water in water medium using the 2D TG-43 approximation, designated $\dot{D}(r, \theta)$, is described using the following formula:

$$\dot{D}(r, \theta) = S_K \Lambda \frac{G_L(r, \theta)}{G_L(r_0,\ \theta_0)} g_L(r) F(r, \theta) \qquad (24)$$

Many of the parameters in this formula were introduced with the TG-43 formalism, including the radial dose function $g_L(r)$, anisotropy function $F(r, \theta)$ and the dose rate constant Λ [30] [31] [32]. These parameters can be calculated from Monte Carlo (MC) simulations (Chapter 3) [13].

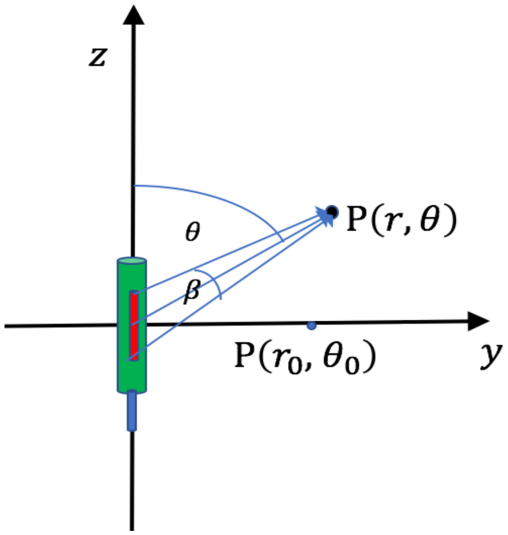

Figure 3 The TG-43 dose calculation geometry for an encapsulated source with a driving cable. It is capable of determining the dose rate at a point P(r, θ), where r is the radial distance from the source center and θ is the angle subtended with respect to the longitudinal axis.

2.6.1 Air Kerma Strength S_K

The air kerma strength S_K is conventionally defined as the product of the reference air kerma rate evaluated at a distance d along the transverse plane, designated $\dot{K}_\delta(d)$, and the square of the distance d:

$$S_K = \dot{K}_\delta(d) \cdot d^2 \qquad (25)$$

The reference distance Is conventionally d = 1 m and $\dot{K}_\delta(d)$ is measured *in vacuo*, indicating that resultant measurements have been corrected for attenuation and scattering within the intermediate media [13]. $\dot{K}_\delta(d)$ is also evaluated with respect to a cutoff energy δ (typically 5 keV), as this suppresses low-energy characteristic x-rays generated within the source encapsulation that do not contribute significantly to dose [13]. As a result, S_K is typically expressed with units U, where 1 U = 1 cGy cm^2 h^{-1}.

2.6.2 Dose Rate Constant Λ

The dose rate constant in water, Λ, is defined as the ratio of the dose rate to water in water medium at the reference location $(r_0,\ \theta_0) = (1\text{ cm},\ 90°)$ to the previously defined air kerma strength S_K:

$$\Lambda = \frac{\dot{D}(r_0,\ \theta_0)}{S_K} \qquad (26)$$

Λ is a parameter that depends on the components of the radioactive source geometry, structure and the particular radionuclide under consideration [13]. The units of Λ are cGy $h^{-1}\,U^{-1}$.

2.6.3 Geometry Function $G(r,\theta)$

In TG-43 calculations, the role of the geometry function $G(r,\theta)$ is to provide an effective inverse-square law correction based upon the assumed shape of the source core [13]. For $\dot{D}(r,\theta)$ calculations using the 2D TG-43 approximation, the source core is considered to be an ideal 1D line segment with radioactivity distributed uniformly across the length L [13]. Hence, the geometry function calculated using the line source approximation (designated $G_L(r,\theta)$) is given in the following expression from TG-43U1:

$$G_L(r,\theta) = \frac{\beta}{L_s r \sin\theta} \text{ if } \theta \neq 0° \qquad (27)$$

$$G_L(r,\theta) = \frac{1}{r^2 - \frac{{L_s}^2}{4}} \text{ if } \theta = 0° \qquad (28)$$

β is the angle subtended by the point of interest $P(r,\theta)$ and the two ends of the core, which has an active length L_s [13].

For 1D TG-43 calculations, the point source approximation is used instead. The geometry function, designated $G_P(r,\theta)$, is independent of the polar angle θ and simply equal to $\frac{1}{r^2}$ (indicating that no correction is applied to the inverse-square law) [13]. While the radial dose function $g(r)$ is often calculated using the point-source approximation and the line-source approximation for the geometry function (designated $g_P(r)$ and $g_L(r)$ respectively), the anisotropy function $F(r,\theta)$ is typically only considered using the line-source approximation for the geometry function [13]. The units of the geometry function are typically cm^{-2}.

2.6.4 Radial Dose Function $g(r)$

The radial dose function, denoted either $g_P(r)$ or $g_L(r)$ based upon the geometry function used, is a parameter that quantifies the effect of absorption and scatter with distance along the transverse plane ($\theta_0 = 90°$) [13]. It is a dimensionless quantity that is independent of the polar angle θ considered and is defined using the following formula:

$$g(r) = \left(\frac{G(r_0,\ \theta_0)}{G(r,\ \theta_0)}\right)\left(\frac{\dot{D}(r,\ \theta_0)}{\dot{D}(r_0,\ \theta_0)}\right) \qquad (29)$$

Hence, it already takes the effective inverse-square law corrections (if any) of the corresponding geometry function into account. At the reference location, $g(r_0) = 1.0$.

2.6.5 Anisotropy Function $F(r,\theta)$

Finally, the anisotropy function $F(r,\theta)$ considers absorption and scatter effects attributable to source design factors (including the encapsulation, the active core and the driving cable) [13]. The effects of source design are the predominant cause of angular dependence in the dose rate distribution and are accommodated for in the dimensionless quantity $F(r,\theta)$ [13].Again, the inverse-square law corrections are taken into account in the definition of $F(r,\theta)$:

$$F(r,\theta) = \left(\frac{G(r,\ \theta_0)}{G(r,\theta)}\right)\left(\frac{\dot{D}(r,\theta)}{\dot{D}(r,\ \theta_0)}\right) \qquad (30)$$

It is also important to note that the TG-43U1 formalism can be equally applied to absolute dose to water in water medium, $D(r,\theta)$, by simply replacing every dose rate term in all TG-43 parameters with an equivalent absolute dose term. This reasonably assumes that the dose rate ratios (particularly those in the radial dose function and the anisotropy function) are equivalent to absolute dose ratios.

2.7 TG-186: Recommendations for Model-Based Approaches

While the TG-43 dose calculation formalism is consistent and relies on only a few parameters that can be easily calculated, it is a water-based dosimetry system that suffers from dosimetric limitations [13] [36]. These have been well-documented in the literature, particularly in a Vision 20/20 review paper from Rivard *et al* [40]. For low-energy sources, differences in the mass-attenuation coefficients of soft tissue relative to water can lead to significant differences in dose calculated in a non-water medium [40]. The absorbed dose is also affected by the mass-energy absorption coefficient of the medium and is generally 2% lower in tissue compared to water for HDR sources [40]. TG-43 dose calculations do not account for any high-Z heterogeneities [40]. Moreover, the algorithm implicitly assumes that the absorbed dose and kerma are equivalent within 5% (which is invalid within a few millimetres of an ^{192}Ir source). [40]

In light of these dosimetric limitations, a number of model-based dose calculation algorithms (MBDCAs) have been developed to model radiation transport within non-water media (including high-Z heterogeneities, applicators and tissues) [36]. Examples of MBDCAs include the collapsed-cone superposition/convolution method, deterministic solutions of the linear Boltzmann transport equation and Monte Carlo simulations (used in this study and discussed more thoroughly in Chapter 3). In 2012, AAPM's Task Group Report No. 186 offered recommendations to early adopters of MBDCAs and guidance on a few major issues that lacked community consensus [36]. This includes the dose specification medium to be selected in MBDCAs and the material definition and assignment method to be used for patient modelling with MBDCAs [36].

2.7.1 Dose Specification Medium

In MBDCAs, radiation is transported within the local medium m, but the calculation of absorbed dose requires a specification medium. Hence, the absorbed dose D can be reported to the local tissue m composing each voxel (designated $D_{m,m}$) or reported instead to a water reference medium w (designated $D_{w,m}$) [36]. This is to be contrasted with the TG-43 dose calculation algorithm, which involves radiation transport occurs within a water medium and is reported with respect to a water reference medium (designated $D_{w,w}$) [30] [31] [32]. TG-186 recommends reporting $D_{m,m}$ and only optionally reporting $D_{w,m}$, as the latter is simply a theoretical construct [36].

2.7.2 Material Definition and Assignment Method

Given the importance of tissue modelling in LDR brachytherapy dose calculations, MBDCAs must be initialized with accurate information concerning the tissue mass density and atomic composition of each voxel within a geometry [36]. These factors are used to determine interaction cross sections for each voxel and influence how radiation is transported [36].

TG-186 recommends using only a few defined materials from previous international reports (including ICRU Report No. 46) and deriving the mass density ρ for these materials from CT images [36]. The process of determining ρ depends on the CT scanner's calibration curve for HU versus electron density relative to water, $\rho_{e,\ rel}$, but further discussion pertaining to this conversion will be provided in Chapter 5 [36].

The tissue composition assignment should be guided using contours delineated by a radiation oncologist [36]. Furthermore, TG-186 recommends that voxels outside of the contours be assigned a "mean soft tissue" from ICRU Report No. 46 [41]. In spite of these recommendations, TG-186 is careful to emphasize that the tissue compositions within the literature are poorly validated and may not represent the tissues of an individual cancer patient [36]. The determination of tissue composition remains an area of active research to this date.

CHAPTER 3 MONTE CARLO SIMULATIONS

3.1 Introduction

Use of the Monte Carlo (MC) technique for numerical integration is ubiquitous, with applications in the physical sciences, finance and even the U.S. Coast Guard's search and rescue operations. This chapter introduces the general principles underlying the MC method in radiation therapy, with a specific interest in the Electron-Gamma-Shower (EGS) system of computer codes [34]. This includes an examination of the primary underlying EGS subroutines, scoring estimators and the history-by-history method for estimating statistical uncertainties. Finally, a discussion on the methods used for modeling complex geometries with the EGSnrc C++ class library (including patient-specific phantoms and brachytherapy sources) is presented [35].

3.2 Analog Simulation of Photon Transport

Monte Carlo simulations can be used to solve the Boltzmann radiation transport equation by stochastically simulating the behavior of many particles within a transport geometry and determining the average [42]. By taking advantage of the central limit theorem and the law of large numbers from statistics, the solution can be determined to a specified statistical uncertainty as the average behavior resulting from these particles [42].

Conventionally, photon transport is simulated by explicitly tracking all particle interactions with the atoms and molecules of the ambient medium [43]. This computational approach is referred to as an analog simulation and involves the statistical selection of a particle's distance to the next interaction site, interaction process and subsequent changes to the particle's energy and direction until a specified threshold energy (PCUT) is reached [43].

In an analog simulation, photons are first produced from the source of radiation specified by the user with a particular direction $\vec{u}$ and energy E [43]. These particle showers are referred to as histories. A particle's distance to the next interaction site is calculated by considering the probability that a particle interacts at a distance r from its original position in the interval dr, designated $p(r)dr$:

$$p(r)dr = e^{-\mu r}\mu dr \tag{31}$$

μ is the linear attenuation coefficient defined in Chapter 2 [13]. The inverse-transform method can be utilized to equate the cumulative probability of $p(r)$ with a random number ξ, allowing a distance r to the interaction site to be computed using a random number generator:

$$r = -\frac{\ln(1-\xi)}{\mu} \tag{32}$$

The photon is then transported to the interaction site in the direction $\vec{u}$ via ray-tracing [43]. As the interaction cross sections are dependent upon the atomic number Z of the material and the density ρ, the simulation must be capable of determining the medium of the interaction site [43].

Based upon the medium of the interaction site and the photon interactions that the user has chosen to model, a finite number of interaction cross sections are available to be sampled using the inverse-transform method [43]. Similar to the selection of r, a number ξ is selected using a random number generator and an interaction is selected based upon the relative probabilities of each interaction possible at the interaction site [43].

Once the interaction is selected, the photon can emerge unaffected or it can be scattered in a different direction $\vec{u}'$ with a possible loss of energy [43]. Secondary charged particles liberated during the interaction are generally transported using Berger's condensed history technique and must also be followed until the low-energy limit (ECUT) is reached [43]. To determine the changes in energy and direction to the photon, the probability distributions associated with the interaction cross sections must be sampled using a random number generator [43].

Once all photons and secondary charged particles have energies below their energy cutoffs (PCUT and ECUT respectively), energy is deposited locally to the region the particles are in. It is also possible for particles to simply escape the geometry entirely. Note that the quantity of interest specified by the user is scored as an average over finite voxels and not to points [43]. The statistical uncertainty of a dose calculation depends on the number of particle histories N and usually decreases as $N^{-1/2}$ [34]

Within the context of brachytherapy dose calculations, charged particle equilibrium can be assumed beyond 2 mm of an ^{192}Ir source for all scoring voxels [29]. Hence, dose can be equated with collision kerma and the latter can be scored instead by simply suppressing electron transport [29]. By choosing an appropriately large ECUT, secondary electrons generated during photon interactions can be deposited locally within the voxel corresponding with the interaction site [29].

3.3 EGSnrc

EGSnrc is a general-purpose package for MC simulations that is capable of transporting photons and electrons from energies of a few keV up to hundreds of GeV [34]. Radiation transport can occur within elements, compounds or mixtures as defined through the data preparation package PEGS4 [34]. Furthermore, many physical processes are available for simulation (including Compton scattering, Rayleigh scattering and the photoelectric effect, as discussed in Chapter 2). EGSnrc has been used for all radiation transport calculations performed in this work.

3.3.1 EGSnrc Subroutines

A few subroutines specific to EGSnrc are worthy of further discussion.

- HATCH is a subroutine involved in reading the radiation transport media data defined using PEGS4 [34].
- SHOWER initializes the subroutines involved in photon and charged particle transport for each particle history [34].
- The subroutine HOWFAR is user-specified and defines the radiation transport geometry. All regions must be assigned an atomic composition and density [34].

- AUSGAB is the subroutine used to score a quantity of interest (like dose) with a scoring estimator (to be discussed shortly) [34].

3.3.2 History-By-History Approach

During an EGSnrc MC simulation, a quantity X is estimated with $\bar{X}$, the average of a set of N statistically independent particle showers (termed histories). If X_i denotes the scored quantity associated with history i, the best estimate of the variance of the mean ($S_{\bar{X}}$) is determined using a history-by-history approach [44]:

$$S_{\bar{X}} = \sqrt{\frac{1}{N-1}\left(\frac{\sum_{i=1}^{N} {X_i}^2}{N} - \left(\frac{\sum_{i=1}^{N} X_i}{N}\right)^2\right)} \qquad (33)$$

3.4 Scoring Estimators

The AUGSAB subroutine must be provided with a method for computing the quantity of interest called a scoring estimator [42]. In brachytherapy dose calculations, one of two scoring estimators is generally used to score dose with voxels of the geometry generated by HOWFAR. The first is called the analog estimator and computes the energy deposited by calculating the difference between the energy entering and leaving the voxel [42]. One can subsequently derive dose by dividing by the voxel's mass (which depends on the mass density ρ). This is to be contrasted with the track-length estimator, which scores dose by allowing contributions to a voxel from all photons with a flight path that cross through its sensitive volume [42]. An increase in efficiency of 20-50 has been reported for this estimator compared to the analog estimator [42]. That said, the simpler analog estimator has been chosen for MC dose calculations in this work.

3.5 egspp: the EGSnrc C++ Class Library

The EGS system was developed to be general-purpose in nature and merely provides methods for accessing cross-section libraries, simulating particle interactions and propagating radiation in arbitrary geometries [34]. This design philosophy grants MC practitioners the freedom of developing programs with user-specified geometries and particle sources tailored for a host of applications, along with routines for scoring virtually any dosimetric quantities of interest. However, modeling sophisticated geometries and particle sources remained a computationally intractable □ulphur□ that was practically restricted to programmers of the highest proficiency.

Created in April 2005, the open-source EGSnrc C++ class library (egspp) addressed these concerns, providing users with a general-purpose geometry package and a set of classes for particle sources and quantity scoring [35]. MC calculations can be performed using a self-contained egspp application, requiring only an input file (of format *.egsinp) specifying the geometry, particle sources and MC-related parameters selected by the user [35].

Many features available within the egspp framework are well-suited for MC dose calculations for brachytherapy and have been utilized in this work.

3.5.1 EGS_XYZGeometry

Three-dimensional gridded geometries consisting of rectilinear voxels can easily be constructed using the EGS_XYZGeometry class [35]. These gridded geometries are desirable for data analysis, as the distribution of the scored quantity of interest can be evaluated in multiple planes and any directional dependence can also be assessed. Since the user must specify the boundaries in X, Y and Z between voxels, the voxel size can also be varied (e.g. voxels can be larger at further distances away from a radioactive source to compensate for the limited interaction counts and improve dose statistics).

The EGS_XYZGeometry class is also relevant for the creation of patient-specific phantoms [32]. One can create a gridded rectilinear geometry (XYZ_Geometry) using the latent electron density information from a patient's CT scan provided it is available in two EGSnrc file formats (*.ramp and *.egsphant). The *.egsphant file is an ASCII file specifying the media of the phantom, the voxel boundaries in the X, Y, and Z directions, and the relevant media and density of each voxel. The *.ramp file defines the mass-density-to-medium conversion rules for the phantom and is also required at this time. A medium *I* is to be used for all voxels between mass density *min_density_i* and *max_density_i*, assuming a default density *default_density_i*. *.egsphant and *.ramp files can be created using the file editing features in MATLAB and require the user to specify a tissue assignment scheme (discussed in Chapter 4) and the contour information contained in the patient's RP-DICOM file.

3.5.2 EGS_NDGeometry

Using the EGS_NDGeometry class, cut planes can be placed within a three-dimensional space to demarcate spaces to insert a geometry [35]. Hence, sophisticated geometries can be constructed in a composite manner from simpler geometrical objects (such as spheres, cones and cylinders). For example, radioactive sources can be constructed with the EGS_NDGeometry class in this manner. It is important to note that geometries are embedded within the gridded background of the phantom and consequently, internal effects cannot be assessed unless the embedded geometry itself is voxelized.

3.5.3 EGS_SourceCollection

egspp particle sources are objects capable of delivering a distribution of particles in accordance with an energy spectrum specified by the user [35]. These particles are characterized in terms of their charge q, energies E, positions $\vec{x}$, directions $\vec{u}$ and statistical weights w. While it is possible to use classes for defining monoenergetic and Gaussian energy spectra, EGSnrc distributions also come with a series of tabulated photon and beta emission spectra for a variety of radionuclides (including ^{60}Co, ^{137}Cs and ^{192}Ir) that can be utilized. Particle sources can further be defined as point sources, parallel beams, or as isotropically emitting sources with a user-defined shape. Particle sources are placed at the origin by default but can be moved to specific locations and even rotated using the EGS_TransformedSource class [35]. The EGS_SourceCollection class allows the user to specify multiple particle sources at once, with probabilistic activation weights w_j associated with each of the j sources considered. These particle sources share the number of particle histories set by the user. The EGS_SourceCollection may be useful for simulating treatments that involve multiple sources, such as in LDR brachytherapy implants, but it is also used in this work to model an HDR brachytherapy treatment (Chapter 5).

3.6 `tutor7pp`

EGSnrc has built-in parallel processing capabilities that can be summoned using a computer cluster's batch queueing system [34] [35]. As a result, egspp applications can also be written to facilitate the parallelizable scoring of a quantity of interest [32]. The prototypical application for this purpose is `tutor7pp`, which scores the deposited, transmitted and reflected energy fractions in any geometry region within the vicinity of a user-specified particle source [35]. In this work, `tutor7pp` has been altered to score the deposited energy within each region of an input geometry.

Prior to simulation, the set of histories can be split into sized partitions, referred to as chunks in the EGSnrc documentation [34]. Since the chunk size determines the number of histories accessible to be simulated for each central processing unit (CPU), it allows the parallel processing system of a computer cluster to allocate histories to CPUs in proportion with each CPU's computation speed and ultimately increases the efficiency of the simulation. The number of chunks is thus a run control variable in `tutor7pp` that can be specified in the user's input file (*.egsinp).

Chunks can be further divided into a set of batches, with the batch number determined in the user's input file. While batches were once instrumental for the calculation of statistical variance $S_{\bar{X}}$ in earlier instantiations of EGSnrc, the history-by-history method has relegated batches to serve merely as simulation checkpoints [34] [44]. At the conclusion of each batch in `tutor7pp`, the accumulated simulation progress associated with a given CPU is reported and outputted to a log file (with format *.egslog) and the data corresponding to the simulated histories within the batch is condensed and added to a repository file (with format *.egsdat) [34]. It is then possible to import these files into programming languages like MATLAB (The MathWorks, Inc., Natick, Massachusetts, U.S.A.). in order to analyze the resulting distribution of the scored quantity.

3.7 Simulating Brachytherapy Using egspp

Previous studies have demonstrated the viability of conducting MC brachytherapy simulations using egspp. Recently, Chamberland *et al*. developed `egs_brachy`, an EGSnrc user code capable of performing brachytherapy-specific dose calculations using a library of pre-defined sources, applicators and phantom geometries [45]. `Egs_brachy` includes the ability to define phase-space sources and has a particle recycling feature for re-using particles generated from one source for other sources within the geometry [45]. `Egs_brachy` also includes a few variance reduction techniques capable of improving the simulation efficiency for a given number of particle histories without biasing the result [45]. These include bremsstrahlung cross-section enhancement, uniform bremsstrahlung splitting and Russian roulette. According to the study introducing `egs_brachy`, the user code was capable of calculating dose distributions for geometries approximating prostate and permanent breast implants in 39 seconds while achieving a 2% average statistical uncertainty to doses in the PTV [45].

CHAPTER 4 PROSTATE CALCIFICATIONS

4.1 Introduction

This chapter reviews the primary approaches that have been used to determine the material composition of prostate calcifications to this date, including Fourier transform infrared spectroscopy (FTIR), Raman spectroscopy and micro-particle induced x-ray emission (μ-PIXE). Characterization studies using these techniques have strongly influenced the prostate calcification modeling in this thesis.

While most MC studies into the dosimetric consequences of prostate calcifications have been restricted to LDR brachytherapy, this chapter summarizes the key developments in the evolution of these studies in order to justify the methods and assumptions used in the present HDR study. Finally, the chapter concludes with hypotheses regarding the dosimetric effects of prostate calcifications in HDR brachytherapy with ^{192}Ir.

4.2 Composition and Characterization of Prostate Calcifications

Prostate calcifications are high-Z materials formed from calcium deposition within prostate tissue or the acini of the prostate gland [4]. While the calcification formation process is not well understood, it is hypothesized to be related to stagnant prostatic fluid [4]. Both highly concentrated and more diffuse calculi have been observed during surgery and from all major diagnostic image modalities (including CT, ultrasound and MRI) [4]. In contrast to acquired CT images, real-time ultrasound images do not convey information about the density properties of calcified regions and are thus less advantageous for the numerical modeling of calcifications.

Surgical resection studies offer a unique insight into the anatomical distribution of calcifications of prostate cancer patients. Suh *et al.* recently studied the frequency and patterns of calcifications within the prostate and ejaculatory system in this manner [46]. The authors examined whole mount sections of 298 specimens extracted from consecutive radical prostatectomy or radical cystoprostatectomy due to prostate and/or urinary bladder cancer. While 14 cases involved benign prostate specimens, 284 involved prostates with adenocarcinoma. The authors determined that calcifications were found in 88.6% of all prostate and ejaculatory systems, 58.1% of seminal vesicles and 17.1% of ejaculatory ducts [46].

In 2012, the TG-186 report highlighted prostate and breast calcifications as materials of interest for heterogeneity correction in brachytherapy [36]. Citing an early study conducted by Chibani *et al*. into the dosimetric effect of prostate calcifications on ^{103}Pd and ^{125}I LDR brachytherapy prostate implants, the report formally recommended the use of breast calcification (with the elemental composition by percentage mass tabulated in ICRU Report 46) as a surrogate material for prostate calcifications [36] [41] [48]. The rationale for this decision was predicated upon a lack of reliable compositional information about prostate calcifications [36].

In response to the recent interest in modelling patient heterogeneities using MBDCAs for brachytherapy, researchers have increasingly focused on accurately determining the chemical composition of prostate calcifications. One technique for identifying the organic and inorganic molecular constituents of prostate calcifications involves measuring infrared (IR) spectra using a Fourier Transform infrared (FTIR) spectroscopic system, Raman shift using a Raman spectroscopic system or a system combining the modalities [48]. Raman shifts occur when monochromatic laser photons are scattered inelastically by excited molecules within a medium, resulting in scattered photons with a detectable frequency and energy difference relative to the incident photons. Both Raman and FTIR systems can probe into the molecular vibrations of calcifications, with Raman relying on variations in molecular polarizability and FITR relying on variations in the molecular dipole moment evident from the IR spectra [48].

In a study by Hsu *et al*., ground prostatic calculi samples extracted from nine patients with benign prostatic hyperplasia were sealed within two pellets of KBr and subsequently pressed to form a disc that could be analyzed using separately using both FTIR and Raman spectroscopic systems [48]. FTIR results indicated that the samples mainly consisted of carbonated hydroxyapatite [$Ca_{10}(PO_4)_6(OH)_2$], although additional traces of undifferentiated calcium oxalate [CaC_2O_4] were also detected in some calculi considered [48]. The Raman spectroscopic system was able to further resolve the calcium oxalate, discerning both calcium oxalate monohydrate [$CaC_2O_4\ H_2O$] and calcium oxalate dehydrate [$CaC_2O_4\ 2H_2O$] in some of the samples [48]. Results were also corroborated using a FTIR microspectroscopic mapping system that was developed to rapidly and accurately determine the molecular constituents without the need for combining conventional FTIR and Raman systems [48]. Only carbonated hydroxyapatite will be considered for calcification modelling in this study.

Additionally, micro-particle induced x-ray emission (μ-PIXE) has been used to probe the composition of prostate calcifications [4] [49]. Pope *et al*. extracted four calcified specimens from patients during prostatectomy and exposed the samples to 3 MeV proton microbeams generated in a 10 MV Tandem accelerator at the Australian Nuclear and Science Technology Organization [4] [49]. The irradiated samples emitted characteristic x-rays in response to atomic de-excitation events, which were subsequently detected by a 100 mm^2 high-purity Germanium detector located 100 mm away from the sample. Information about heavy elemental composition and a 2D distribution of trace elements could then be obtained [4] [49].

μ-PIXE results for the four calcified samples indicated the presence of phosphorus, sulphur, chlorine, potassium, calcium, iron, zinc and strontium in significant quantities [4] [49]. While the authors postulated differences in calcification composition could be attributable to variations in the patient-specific calcification synthesis process, further investigation was beyond the scope of their research [4] [49]. Lighter elements undetectable using the μ-PIXE technique were approximated to be oxygen for calcification modeling simulations, an assumption justified by the authors as being consistent with previous studies that suggested calcification was primarily carbonated hydroxyapatite and calcium oxalate [4] [49]. While Pope had four different composition types, only the first one (hereto referred to as Pope calcification #1) will be considered in this study.

Elemental compositions by percentage mass for all calcification materials discussed in this section are supplied in Chapter 5.

4.3 Approaches to Calcification Modeling

To date, the vast majority of MC prostate calcification modeling studies have been restricted to assessing the dosimetric impact in LDR brachytherapy contexts. As any MBDCA must provide a voxel-by-voxel cross-section assignment in accordance with a consistent underlying guideline, these investigations can naturally be categorized by the manner in which calcification materials and densities were assigned [36].

4.3.1 Random Assignment of Calcification Voxels

Earlier studies often modeled localized calcifications as CT-voxel-sized cubes randomly scattered throughout a fixed amount of the prostate volume phantom. In 2005, Chibani *et al.* investigated the impact of prostate calcifications on ^{103}Pd and ^{125}I LDR implants by modeling calcifications as 2 x 2 x 2 cm^3 cubes of breast calcification (ICRU Report No. 46) randomly scattered throughout the prostate volume in 1-5% of the voxels [41] [47]. The authors reported a maximal dose reduction of 37% to the clinical target volume (CTV) D_{90} when 5% of the voxels in the prostate volume were calcified [47].

A 2007 retrospective post-implant ^{125}I dosimetry study by Carrier *et al*. was similarly concerned about localized calcifications, but also considered the impact of modeling diffuse calcifications [50]. The calcification model utilized for MC simulations, whether diffuse or localized, was reported to have a significant impact on the underlying dosimetry. For extreme models, dose differences of more than 10 Gy (6.94% of the 144 Gy prescription dose) were observed for the CTV D_{90} [50]. The authors elected not to show their preliminary results, noting the challenge of choosing a correct calcification model and assigning a realistic calcification mixture to voxels based upon the limited elemental information available from CT images [50]. Carrier *et al.* ultimately concluded that calcification modeling was an aspect of model-based dose calculation that required further investigation [50].

4.3.2 Tissue Assignment Schemes

Given the limitations brought forward by Carrier *et al*., some rationale was now required for MBDCAs to ensure tissue assignment was performed adequately (particularly for prostate calcifications). Accurate tissue assignment is particularly important in the context of low-energy brachytherapy, as attenuation and mass absorption coefficients are highly variable at lower energies [36]. As a result, tissue assignment schemes were developed to assign materials and densities to all CT image voxels within a given physician-delineated contour, thereby creating a virtual patient geometry for MC simulations [36]. This material assignment could be based upon the CT number of each particular voxel or assigned independently [36]. Similarly, the density of the assigned material could be CT-derived or a nominal density [36].

This technique is ultimately more malleable than a simple random assignment to a subset of the voxels within the prostate, as calcifications can be exclusively introduced to voxels with sufficiently large CT numbers and schemes with varying levels of sophistication can easily be compared. For example, a scheme assigning prostate tissue of nominal density to all voxels within the entire prostate contour can be compared to one that assigns calcifications (or even interpolations between calcification and prostate tissue) to voxels within the prostate based upon voxel CT numbers. However, it is important to note that tissue compositions are generally assumed and the assigned material may not adequately correspond to the actual composition of the voxel [36]. Hence, further research into methods for accurately determining the composition of tissues and calcifications within a patient is still required.

In 2014, Mason *et al.* performed MC dose calculations with MCNPX using post-implant CT images from 40 ^{125}I patients [51]. Ten of these patients were chosen specifically because they had the largest calcification volumes from their post-implant CT images out of the most recent 100 patients. Virtual ^{125}I seeds were implanted into a voxelized water phantom, a voxelized prostate phantom and a voxelized phantom containing prostate tissue, mean male tissue and bone based on the post-implant CT [51]. In the prostate phantom, the mass densities of all voxels were CT-derived (with prostate tissue for all voxels within the CTV and mean male tissue for all voxels outside of the CTV) [51]. The final phantom assigned bone with CT-derived density to background voxels with Hounsfield Units (HU) values greater than 200 (associated with a density 1.2 g/cm^3) and mean male tissue with CT-derived density to all other background HU values [51]. Similarly, prostate tissue was assigned to prostate voxels with HU values less than 200 and a mixture of prostate tissue and calcification was assigned to voxels exceeding this value [51]. The authors compared results from the complex tissue phantom to the MC water phantom for patients with calcifications and observed a mean reduction to the prostate D_{90} of 4.5% [51]. Furthermore, the maximum prostate D_{90} reduction exhibited was 7.4% [51]. This exceeds the effect of interseed attenuation and tissue modeling for patients without calcifications, where the mean reduction to the prostate D_{90} was 2.9% for the prostate phantom compared to the water phantom [51].

Similarly, Miksys *et al*. developed tissue assignment schemes for post-implant CT images of eight prostate LDR brachytherapy patients treated with ^{125}I sources and performed patient-specific simulations using the EGSnrc user code BrachyDose [52]. While the tissue assignment schemes were similar to those utilized by Mason *et al*., some novel schemes involved assigning homogeneous mixtures of calcification and prostate (using 20% and 5% mass fraction increments) to voxels within the prostate [51][52]. For *n*% prostate tissue and *m*% calcification, the theoretical mass densities of these mixtures was computed using the following formula:

$$\rho_{n\%p,m\%c} = \frac{100 \cdot \rho_p \cdot \rho_c}{n \cdot \rho_c + m \cdot \rho_p} \tag{34}$$

Halfway threshold densities between mass fraction increments were used to derive CT number thresholds, which could be used for assigning densities to HU values [52]. The authors noted lower doses (potentially by 25-30%) to all voxels near a calcification, attributable to an attenuation effect caused by the higher atomic number of the calcification [52]. Moderate (2-5%) discrepancies in all prostate dose metrics considered, including D_{90}, V_{100} and $V_{150,}$ were also reported when compared to a water phantom [52].

Collins-Fekete *et al*. conducted a retrospective study into the effects of calcifications on LDR dose distributions for 43 prostate cancer patients with visible calcifications [53]. Unlike Miksys *et al*., the contours of interest in this study also included the bladder, rectum, CTV and urethra. MC simulations were performed in GEANT4, which uses a Layered Mass Geometry mode that allows for the superposition of radioactive sources onto a voxelized grid [52] [53]. A MC phantom involving water and calcified tissues was compared to a purely water geometry, resulting in an average decrease of 6.4% in the prostate D_{90} and an average decrease of 2.6% for V_{100} when dose was scored with reference to the local medium [53]. Extreme clinical cases resulted in dose discrepancies on the order of 45%. The authors concluded that the effect of calcifications in LDR brachytherapy was comparable to the effect of including prostate tissue heterogeneity. Furthermore, calcifications had a stronger mean effect than interseed attenuation [53].

4.4 Predictive Metrics

To make predictions regarding potential MC dose discrepancies, highly sensitive metrics must be established that correlate well with existing data. Using linear regression, Collins-Fekete *et al*. determined that the ratio of calcification volume to prostate volume was a reasonable predictor of large dose discrepancies between a TG-43 dose distribution and a dose distribution calculated in a calcified MC phantom ($R^2 = 0.75$) [53]. On the other hand, the distance between the calcification center-of-mass and the prostate center-of-mass, normalized to the effective radius of the prostate, was a less effective predictor ($R^2 = 0.34$) [53]. While this line of inquiry is highly speculative and still in its infancy, it is possible that metrics developed in LDR brachytherapy studies will be equally applicable to HDR studies.

4.5 HDR Brachytherapy Hypotheses

The surge of MC studies that model complex factors (like calcifications) in LDR brachytherapy has influenced research in HDR brachytherapy as well. Recently, Mason *et al.* used MC simulations to assess whether ultra-focal prostate HDR brachytherapy plans are more sensitive to MC-related dose discrepancies compared to whole-gland treatment plans [25]. This was largely evaluated by adding air-filled steel catheters (Elekta AB, Stockholm, Sweden) to MC water phantoms being treated with whole-gland, hemi-gland and ultra-focal treatments [25]. The catheters had a 1.9 mm outer diameter, a 7 mm long plug and a 3 mm conical end section. The authors concluded that MC-calculated focal treatments only resulted in a minor decrease in most DVH parameters (< 2%) compared to MC-calculated whole-gland treatments (< 1.5%), indicating little additional sensitivity [25]. At the time of publication (2014), there were no previously published MC studies related to HDR prostate brachytherapy.

Little research has been conducted concerning the effects of modeling prostate calcifications on the dose distribution near a ^{192}Ir source. In a recent Vision 20/20 article published in 2009, Rivard *et al.* reasoned that the prostate anatomical site would be mostly insusceptible to significant differences between administered and delivered doses due to the dosimetric limitations of TG-43 [30] [31] [32] [40]. The authors noted that

HDR prostate implants do not suffer from interseed attenuation [40]. Since the prostate is deeply seated, it more closely approximates the TG-43 water phantom geometry than other sites and is thus less sensitive to radiation scattering conditions [40]. Furthermore, high-energy photons have approximately the same attenuation properties per centimeter in water and tissue and high-Z materials used in HDR brachytherapy (such as a 0.1 mm thick stainless steel applicator) do not cause large deviations in photon transmission rates through water [40]. Hence, it is hypothesized that calcifications will only cause significant dose perturbations if they have a substantial effective radius (to maximize attenuation-related deviations in photon transmission rates) and are placed within a few millimeters of the ^{192}Ir source. Within a treatment context, the effect is hypothesized to be negligible compared to the 2% difference observed between the absorbed dose to tissue and the absorbed dose to water.

CHAPTER 5 METHODS

5.1 Source Model

The microSelectron-v2 HDR ^{192}Ir source (Nucletron B.V, Veenendaal, The Netherlands) was modeled predominantly using the dimensions specified in earlier studies by Taylor *et al.* (corrected in 2017) and Daskalov *et al* [54] [55] [56] [57]. It consisted of an ^{192}Ir core, an AISI 316L stainless steel encapsulation, and an AISI 316L stainless steel driving cable. The ^{192}Ir core (with density 22.42 g cm^{-3}) was modelled as a 3.48 mm long cylinder (0.65 mm in diameter) with two appended 45° conical sections (0.265 mm in length) serving as the rounded ends [58]. Furthermore, the AISI 316L stainless steel encapsulation (with density 8.06 g cm^{-3}) was modelled as an enclosing cylinder (0.9 mm in diameter) with a hemispherical tip (0.45 mm in cross-sectional diameter, located 2 mm from the center of the cylinder). By comparison, the AISI 316L stainless steel composing the driving cable has a density of 4.81 g cm^{-3} and was simply modelled as an appended 2 mm long cylinder (with a 0.7 mm diameter) attached to the end of the encapsulating cylinder. In Figure 4, the microSelectron-v2 HDR ^{192}Ir source is visualized using egs_view, a graphical user interface (GUI) capable of visualizing egspp geometries.

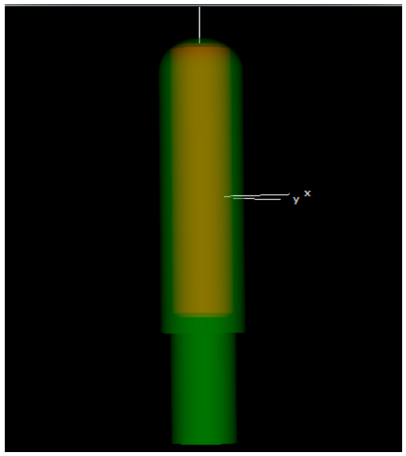

Figure 4 The microSelectron-v2 source model used in this study, as visualized with the EGSnrc GUI egs_view. The AISI steel encapsulation and driving cable are indicated in green, while the ^{192}Ir active core is displayed as red. The egs_view coordinate system is also visible in white.

The microSelectron-v2 was fully specified with the addition of an egspp particle source, an object that used a Zaman and Marsaglia random number generator (ranmar) to sample photons from an incident bare ^{192}Ir energy spectrum (Duchemin and Coursol) [59]. Photons were sampled isotropically from a cylindrical shape with the same dimensions and active length as the ^{192}Ir core.

5.2 Material Generation

An aggregated dataset specifying all materials involved in radiation transport was generated using PEGS4 code. This included any materials associated with the microSelectron-v2, ambient surrounding materials (including water, prostate tissue, air and cortical bone) and all calcification compositions. Table 6 details all of the materials and mixtures used in this thesis. Some media were specified as mixtures by weight using literature-derived mass elemental compositions, but many of the homogeneous mixtures consisting of n % prostate and m % calcification were derived by calculating the theoretical mass density of the mixture $\rho_{n\%p,m\%c}$:

$$\rho_{n\%p,m\%c} = \frac{100 \cdot \rho_p \cdot \rho_c}{n \cdot \rho_c + m \cdot \rho_p} \tag{35}$$

Transport functions (including cross sections, ionization stopping powers and gamma-ray mean free paths) were computed based upon the elemental component of each mixture and were fitted within a delimited range of energies for photons and electrons using piecewise linear functions. The upper cutoff energies for photon and charged particle transport (UP and UE) were set to 50 MeV (an arbitrary value that far exceeds brachytherapy energies), while the lower cutoff energies AE and AP were 0.512 MeV and 0.001 MeV for electrons and photons respectively. AE and UE are required parameters for material generation, even though electrons are not transported in the simulation.

Table 6 A list of materials used in MC simulation geometries in this thesis.

Tissue	Density ρ [g cm^{-3}]	Mass % H	Mass % C	Mass % N	Mass % O	Other Contributions
^{192}Ir [58]	22.4	-	-	-	-	Ir (100%)
AISI steel cable and encapsulation [58]	8.02 (encapsulation) 4.81 (steel cable)	-	-	-	-	Mn (2%), Si (1%), Cr (17%), Ni (12%), Fe (68%)
Woodard and White prostate [61]	1.92	10.5	8.9	2.5	77.4	Na (0.1%), Mg (0.2%), P (10.3%), S (0.3%), Ca (22.5%)
ICRU breast calcification [41]	3.06	0.3	1.6	0.5	40.7	P (18.7%), Ca (38.2%)
Carbonated hydroxyapatite [48]	3.16	0.2	_	_	41.4	P (18.5%), Ca (39.9%)

Tissue	Density ρ [g cm^{-3}]	Mass % H	Mass % C	Mass % N	Mass % O	Other Contributions
Pope composition #1 [49]	3.16	-	-	-	28.78	P (23.08%), S (0.29%), Cl (0.44%), K (0.06%), Ca (39.55%), Fe (0.007%), Zn (7.74%), Sr (0.035%)
ICRU mean male soft tissue [41]	1.03	10.5	25.6	2.7	60.2	Na (0.1%), P (0.2%), S (0.3%), Cl (0.2%), K (0.2%)
Woodard and White cortical bone [52]	1.92	3.4	15.5	4.2	43.5	Na (0.1%), Mg (0.2%), P (10.3%), S (0.3%), Ca (22.5%)
TG-43 Reference Air (40% Humidity) [31][32][33]	0.00120	0.0732	0.0123	75.0325	23.6077	Ar (1.2743%)

Tissue	Density ρ [g cm^{-3}]	Mass % H	Mass % C	Mass % N	Mass % O	Other Contributions
TG-43 Reference Water [32] [32] [33]	0.998	11.2	-	-	88.8	-
80%p20%c ICRU [41] [52]	1.20	8.5	7.4	2.1	70.1	Na (0.2%), P (3.8%), S (0.2%), K (0.2%), Ca (7.6%)
60%p40%c ICRU [41] [52]	1.41	6.4	6.0	1.7	62.7	Na (0.1%), P (7.5%), S (0.1%), K (0.1%), Ca (15.3%)
40%p60%c ICRU [41] [52]	1.72	4.4	4.5	1.3	55.4	Na (0.1%), P (11.3%), S (0.1%), K (0.1%), Ca (22.9%)
20%p80%c ICRU [41] [52]	2.20	2.3	3.1	0.9	48.0	P (15%), Ca (30.6%)

5.3 Dose Calculation Framework and Monte Carlo Parameters

The EGSnrc user-code `tutor7pp` was modified in order to score the total energy deposited within all regions specified in an egspp geometry. This allowed dose distributions to be calculated within all phantom geometries considered in this study.

Unless otherwise indicated, photon transport was simulated using a global photon transport cutoff energy (PCUT) of 1 keV and includes Rayleigh scattering, photoelectric absorption, bound Compton scattering and the fluorescent emission of characteristic x-rays [54]. The PCUT value was selected based upon previous studies by Taylor *et al.* and results in the inclusion of more photons compared to TG-43 (where PCUT is 5 keV) [31] [32] [33] [54] [55]. Photon cross sections used for interaction simulations were referenced from the NIST XCOM database [39]. Since the photon mean free path vastly exceeds the range of secondary electrons for all photon energies in the incident ^{192}Ir spectrum, secondary electrons deposit their energy locally under the assumption of charged particle equilibrium. Thus, electron transport was suppressed using a global electron transport cutoff energy (ECUT) of 10 MeV.

In contrast to the track-length estimators used in various brachytherapy-specific Monte Carlo user-codes (namely MCPT, MCPI, PTRAN and BrachyDose), a simple analog estimator was used to score the energy deposited in MeV to all voxels of the local transport medium based only on the simulated interactions occurring within individual voxels.

5.4 Source Validation

The ^{192}Ir microSelectron-v2 HDR source model was validated through Monte Carlo calculations of selected TG-43 dosimetry parameters, including radial dose functions $g(r)$, anisotropy functions $F(r,\theta)$ and the dose rate constant Λ. Comparison values for TG-43 dosimetry parameters have been calculated in previous studies by Taylor *et al.* using BrachyDose and tabulated in the TG-43 Parameter Database for Brachytherapy associated with the Carleton Laboratory for Radiotherapy Physics [54] [55].

All source validation simulations were performed with the source tip oriented in the +z-

direction and with the source itself located in the center of an (80 x 80 x 80) cm^3 rectilinear phantom composed of TG-43 reference water (0.998 g cm^{-3} at 22 °C) [31] [32] [33]. The phantom dimensions used in this study were motivated by Perez-Calatayud *et al*., as the authors concluded an 80-cm diameter phantom approximates an infinite scattering medium and ensures dosimetric accuracy for $g(r)$ is < 2% within 20 cm of the source (in accordance with the recommendations of AAPM's Task Group No. 56 [TG-56]) [30] [60]. The source was embedded within the center of an (40 x 40 x 40) cm^3 scoring grid of TG-43 reference water voxels prior to being placed within the (80 x 80 x 80) cm^3 exterior phantom. Cubic voxel dimensions for this scoring grid were chosen in accordance with the recommendations of AAPM and ESTRO (European Society for Radiotherapy and Oncology) on dose calculations for high-energy (average energy higher than 50 keV) photon-emitting brachytherapy sources in order to limit volume-averaging artifacts to <0.1% [56]. (0.1 x 0.1 x 0.1) mm^3 voxels were used for the innermost (2 x 2 x 2) cm^3 cube surrounding the source, while (0.5 x 0.5 x 0.5) mm^3 voxels were used for all voxels within a (10 x 10 x 10) cm^3 cube not within the innermost cube [60]. Similarly, (1 x 1 x 1) mm^3 voxels were used for voxels outside of these cubes in a (20 x 20 x 20) cm^3 cube, and (2 x 2 x 2) mm^3 voxels were used for all other voxels within the (40 x 40 x 40) cm^3 scoring cube [60]. These dimensions are similar to those used by Taylor *et al*. while calculating TG-43 dosimetry parameters [54] [55].

5.4.1 TG-43 Parameter Determination

To compute TG-43 dosimetry parameters, specific dose values must be determined at particular radial distances *r* and polar angles θ relative to the source's longitudinal axis. It is worth noting that the center points of the cubic voxels rarely correspond to the values of the radii and/or polar angles associated with tabulated parameter values. As a result, the required dose values and uncertainties for $g(r)$ and $F(r,\theta)$ were derived from a bilinear interpolation involving the nearest neighbouring voxels surrounding the calculation point of interest $P(r,\theta)$ [54] [55]. TG-43 parameter uncertainties were propagated in quadrature using recommendations published in TG-43U1. $g(r)$ and $F(r,\theta)$ were calculated using 10^{10} initial particle histories.

The radial dose function $g(r)$ was calculated separately using both the line source and

the point source approximations to the geometry function, designated $G_L(r,\theta)$ and $G_P(r,\theta)$. While $G_P(r,\theta)$ is implemented mathematically as specified in TG-43U1, a computationally efficient calculation of $G_L(r,\theta)$ was presented by Taylor *et al.* and adopted in this study (Chapter 2) [31] [32] [33] [54]. Unlike those studies, dose values within all regions of the phantom geometry were interpolated and then divided by the relevant values of the geometry functions. To compare directly to results from Taylor *et al.* calculated using BrachyDose, $g(r)$ values were tabulated for radial distances between 0.2 cm $\leq r \leq$ 20 cm [54] [55]. While $g(r)$ was calculated for a fixed polar angle, $\theta = \theta_0 = 90°$, values for a fixed radial distance r were calculated by averaging along 10^4 azimuthal angles (designated φ) along the transverse plane.

Similarly, anisotropy functions $F(r,\theta)$ were calculated at three fixed radial distances (r = 0.5 cm, r = 1.0 cm and r = 5.0 cm) using dose values that were normalized relative to $G_L(r,\theta)$ after interpolation. These functions are designated $F(0.5\text{ cm},\theta)$, $F(1.0\text{ cm},\theta)$ and $F(5.0\text{ cm},\theta)$. For a fixed radial distance r and polar angle θ, $F(r,\theta)$ values were calculated by averaging over 10^4 azimuthal angles φ over the plane defined by θ. Once again, results were compared to Taylor *et al* [54] [55].

The dose rate constant Λ was calculated using the results from two separate simulations, motivated by the approach from Taylor *et al* [54] [55]. In the first, a (0.1 x 0.1 x 0.1) mm^3 water voxel was placed on the transverse plane ($\theta = \theta_0 = 90°$) at a distance of 1 cm from the center of the source within a non-voxelized water phantom with the same dimensions of (80 x 80 x 80) cm^3. The absorbed dose to water per history was calculated within this voxel using a MC simulation, which was initialized with 10^{11} histories and all other aforementioned MC parameters.

In the second, the air kerma strength per history S_K^{MC} was calculated using an expression from Taylor *et al*.:

$$S_K^{MC} = \dot{k}_\delta(d) \cdot d^2 \cdot k_{r^2} \qquad (36)$$

$\dot{k}_\delta(d)$ is the air kerma per history scored in a (10 x 10 x 0.05) cm^3 voxel of TG-43U1 dry reference air (with 40% humidity) embedded along the transverse plane of a (1000 x 1000 x 1000) cm^3 vacuum phantom at a fixed distance of d = 100 cm between the center

of the source and the voxel face [54] [55]. Unlike previous simulations, a photon energy cutoff PCUT of 10 keV was used to eliminate the contributions of any low-energy photons generated within the encapsulating material of the microSelectron-v2 HDR source [54] [55]. This calculation was also performed using 10^{11} particle hiistories.

As noted by Taylor *et al.*, the large voxel dimensions are critical to ensuring $\dot{k}_{\delta}(d)$ can be reported with low statistical uncertainties [54] [55]. As the inverse square law varies over the voxel used to score the air kerma per history, values of the air kerma per history will ultimately depend on the size of the scoring voxel considered [54] [55]. Hence, a dimensionless correction factor k_{r^2} was required to accurately determine the air kerma strength per history at a point when it was scored to a voxel of thickness t and width w:

$$k_{r^2} = \frac{1}{d^2 w^2 t} \int_{d}^{d+t} \int_{-w/2}^{w/2} \int_{-w/2}^{w/2} (x^2 + y^2 + z^2)\, dx\, dy\, dz \qquad (37)$$

The correction factor k_{r^2} allowed the air kerma per history to depend upon the square of the average radial distance r^2as opposed to the distance from the source to the scoring face [54] [55]. For the voxel considered in this study, with t = 0.05 cm and w = 10 cm, the correction factor k_{r^2} was 1.0022. The dose rate constant Λ was finally calculated by dividing the dose to water per history by the air kerma strength per history.

5.5 Calcification Phantom Simulations

To assess the dosimetric consequences of introducing a heterogeneity to the TG-43 reference water media, a series of egspp voxelized water phantoms containing an embedded calcification were developed. The inner partition of the phantom consisted of a (16 x 16 x 16) cm^3 rectilinear water phantom with (1 x 1 x 1) mm^3 scoring voxels chosen to more closely approximate the resolution of a typical patient's CT image. The dimensions of this inner partition resemble those used in a previous study by Carrier *et al.* and approximated the size of the region of interest containing the prostate and all other clinical structures of interest during clinical HDR prostate brachytherapy procedures [50]. Backscatter was provided by embedding this inner partition within a single (40 x 40 x 40) cm^3 water voxel, which acted as the outer partition of the phantom. The microSelectron-v2 HDR ^{192}Ir source model was embedded within the center of the phantom, while a

calcified sphere was placed in the nearby vicinity of this source along the egspp x-axis of the transverse plane. Each simulation was performed using 10^{10} particle histories.

The effect of heterogeneity distance along the transverse plane was considered by varying the radius r_c of a calcified sphere composed of ICRU breast calcification material (a surrogate for prostate calcification) while fixing its center-to-center radial distance r with respect to the source [41]. For two fixed radial distances (r = 5 mm and r = 5 cm), the calcification radius r_c was allowed to assume the values r_c = 1 mm and r_c = 3 mm. To further investigate the impact of the calcification composition selected, a fixed center-to-center radius of r = 5 mm was maintained while the calcification radius was set to r_c = 3 mm.

For all calcification phantoms considered, the results were assessed by examining absorbed dose $D_{w,m}$ profiles along the transverse, axial and coronal planes that pass through the center of the calcification. The calcification is modelled as a singular sphere embedded within the rectilinear voxelized geometry, overlapping with several voxels within the (16 x 16 x 16) cm^3 scoring grid.

Calcified phantoms were compared to a water phantom with the same dimensions in order to compute signed relative percent dose difference maps (defined as $100 \cdot \frac{D_{calcified} - D_{water}}{D_{water}}$) through all planes passing through the calcification center and the source. Dose variations attributable to the embedded calcification could then be assessed within the entire plane. The resulting relative percent dose difference maps were manipulated and made more informative by thresholding values with high statistical uncertainties. This processing allowed the underlying structure of the dosimetric effects to become more readily apparent.

Profiles within the percent dose difference planes that pass through the calcification center were also considered. For a given percent dose difference profile, a series of distance metrics were used to assess the mean, maximum and minimum signed dose difference along the profile between the center of the source and a radial distance d along the profile (designated $\Delta D_{d,mean}$, $\Delta D_{d,min}$ and $\Delta D_{d,max}$ respectively). In the current work, these metrics were assessed for three distance values (d = 2.5 cm, d = 5.0

cm and d = 8.0 cm) for all calcification profiles. These metrics were also used to assess the variability of dose discrepancies with depth along the profile for varied calcification radii.

5.6 Patient-Specific Phantom Simulations

5.6.1 Patient Dataset

The dosimetric impact of calcifications within the context of more sophisticated patient-specific geometries was also investigated through a further series of MC simulations. The work in this thesis retrospectively examined CT images derived from a single anonymized patient with prostate adenocarcinoma who was originally treated with a combination of EBRT and real-time TRUS-guided HDR brachytherapy boost at the NSCC. Using the American Joint Committee on Cancer (AJCC) TNM staging system, the tumour was classified as Stage T2b (N0, M0, a Gleason score of 7 and a PSA ≥ 20). In accordance with D'Amico risk categories, the patient was assessed as High Risk based upon the exhibited PSA level, Gleason score and T stage. The patient received a 15 Gy fraction of HDR brachytherapy one day prior to CT simulation, which was ultimately used to plan the EBRT regimen (consisting of 46 Gy delivered to the prostate and lymph nodes in 23 fractions). All OARs in the dataset were contoured by a dosimetrist, whereas target volumes (including the prostate, seminal vesicles and lymph nodes) were contoured by a radiation oncologist.

In order to create virtual patient phantoms, the patient's CT DICOM images and structure set used for EBRT planning were first imported into MATLAB (The MathWorks, Inc., Natick, Massachusetts, U.S.A.). The planning CT image was acquired using a Varian CT scanner at the NSCC and consisted of 512 x 512 x 136 voxels of size (1.27, 1.27, 2.50) mm^3. Hence, the total image dimensions were 65 x 65 x 34 cm^3. After the image was imported, the DICOM Rescale Slope (equal to unity) and Rescale Intercept (equal to -1024) were extracted from the CT image metadata in order to linearly transform the input pixel values PV to Hounsfield Units HU using the following equation:

$$HU = PV - 1024 \tag{38}$$

Hence, the planning CT image was stored as a 3D matrix of double-precision values

containing the appropriate HU values.

Contoured structures were extracted as 3D binary masks with the same resolution as the planning CT DICOM image. In each binary mask, 0 indicates that a particular voxel is not associated with the structure and 1 indicates that a particular voxel is associated with the structure. One structure included in the structure set was a distinctly visible calcification (with a volume of 0.082 cc, approximately 0.5% of the 17.341 cc prostate volume) that was added by the researchers in order to assess the dosimetric impact of a gross heterogeneity. Furthermore, a urethra structure was contoured from the bladder neck superiorly by the researchers. While the urethra is generally very difficult to completely assess from a CT image, the structure contour followed a typical path (as judged by previous research experience).

5.6.2 Tissue Assignment Schemes

To generate an egspp phantom that accounts for patient heterogeneities, a tissue assignment scheme must be selected in advance, along with the material chosen to model the contoured calcification. Tissue assignment schemes are contour-guided voxel-to-voxel mappings between the planning CT image and the resultant egspp phantom in which HU values in all regions are assigned to a particular material and density from a small library of tissues.

For all tissue assignment schemes that assign mass densities ρ to phantom voxels based upon the HU of the corresponding voxel in the planning CT image, a conversion from HU to ρ was required. Using calibration data associated with the Varian CT scanner at the NSCC (Table 7), HU values were first converted to the dimensionless electron density relative to water $\rho_{e,rel}$. $\rho_{e,rel}$ is defined mathematically as the product of the tissue mass density ρ and the electron density per unit mass (# electrons g^{-1}) N_g for a tissue t relative to water w [36]:

$$\rho_{e,rel} = \frac{(\rho N_g)_t}{(\rho N_g)_w} \tag{39}$$

As the electron density per unit mass N_g varies with a 2% standard deviation over all

human tissues (Beaulieu *et al.)*, $\rho_{e,rel}$ can be related linearly to the tissue density ρ (with units of g cm^{-3}) for all tissues except inflated lung with a maximum error of less than 1% ($R^2 = 0.99992$) [36]:

$$\rho = -0.1746 + 1.176 \cdot \rho_{e,rel} \qquad (40)$$

AAPM's TG-186 recommends the use of this linear relationship for all non-zero values of $\rho_{e,rel}$ to facilitate the assignment of materials based upon a voxel's tissue density ρ [36].

All tissue assignment schemes that were implemented in the current work are listed in Table 8. The 'TG-43' scheme assigned all voxels within the body contour as TG-43 reference water with a nominal density of 0.998 g cm^{-3} and all voxels outside of the body as TG-43 reference dry air (taken at 22℃ and 101.325 kPa) with a nominal density of 0.001196 g cm^{-3} [31] [32] [33]. While this scheme did not generate phantoms with an effectively infinite water medium, it was used to establish a reasonable comparison between MC dose distributions and the IPSA-generated dose distributions calculated using the TG-43-based Oncentra Brachy (Elekta Brachytherapy Solutions, Veenendaal, The Netherlands).

Table 7 The calibration data describing the relationship between HU values and electron density relative to water $\rho_{e,rel}$ for the Varian CT scanner used at the Nova Scotia Cancer Center.

HU	$\rho_{e,rel}$
-1050	0.000
-1000	0.000
100	1.100
1000	1.532
6000	3.920
29000	3.920

The 'TG-186' scheme was a variant of an approach by Miksys *et al*. designed to satisfy the primary requirements of the TG-186 report [35] [51]. In this scheme, all voxels within

the prostate were assigned to be Woodard and White prostate tissue with a nominal density of 1.04 g cm^{-3} , with the exception of a contoured calcification inside the prostate that was assigned one of the calcification materials listed in Table 6 [57]. Furthermore, all voxels within the body contour were assigned to be ICRU 1992 mean male soft tissue with a nominal density of 1.03 g cm^{-3}, while all voxels outside of the body were assigned the TG-43 reference dry air mixture described earlier [31] [32] [33] [41]. By comparing the 'TG-186' scheme to more sophisticated tissue assignment schemes that assign density values to voxels based upon the HU values of the input planning CT, the dosimetric effects of patient heterogeneities were isolated from the effects associated with the mere transition away from a water transport media.

Two tissue assignment schemes, designated as 'PC' and 'PC-20%' as per Miksys *et al*., assigned densities and materials to voxels based upon the input HU values [51]. These schemes can be equally applied for any calcification material specified in Table 6, although only the ICRU breast calcification surrogate was considered in the present study [41]. In these schemes, a homogeneous mixture of n % prostate and m % calcification was assigned to all voxels within the prostate within a particular subset of HU values. For a given tissue assignment scheme resolution r (where r = 50% and r = 20% mass fraction increments between successive mixtures are used for the 'PC' and 'PC-20%' schemes respectively), this range of HU values for homogeneous mixtures of n % prostate and m % calcification was determined by calculating the halfway theoretical mass densities between adjacent materials (i.e. the mixture with $n + \frac{r}{2}$ % prostate and $m - \frac{r}{2}$ % calcification and the mixture with $n - \frac{r}{2}$ % prostate and $m + \frac{r}{2}$% calcification), converting back to $\rho_{e,rel}$ and linearly interpolating using the Varian CT scanner calibration data in Table 7.

The ambient background of the phantom was also modeled using CT information for the latter two tissue assignment schemes. Outside of the prostate target within the body contour, voxels with an HU value greater than 494 were assigned as Woodard and White cortical bone with a CT-derived density [61]. Otherwise, voxels were assigned the mean male soft tissue composition from ICRU 1992 [41].

It is important to note that the overall accuracy of a CT-to-density conversion scheme requires that acquired images be free of residual streaking artifacts [36]. This is generally more of a concern within the context of post-implant CT images in LDR brachytherapy, as metal artifacts must be addressed using a metallic artifact reduction algorithm. To the best of our knowledge, the planning CT image considered in this study had no discernible streaking artifacts.

Finally, a worst-case scenario was assessed using a variation of the 'TG-186' scheme that additionally allowed for the random assignment of nominal density calcification material to 25% of the voxels within the prostate unassociated with the contoured calcification. This was used to assess the relationship between the clinical metrics and the calcification volume to prostate volume ratio.

Table 8 The tissue assignment schemes used during this study, along with their originating sources. For an assigned region of a certain scheme, the tissues compositions in the column next to it indicate what materials can be assigned to that region. The tissue assignment scheme either applies that rule for all HU values in the CT scan or assigns a material depending upon the Varian scanner's HU values. Finally, the density is specified as a nominal average value from the literature (Table 6) or derived from CT images.

Scheme Name	Inspired By	Assigned Region	Tissue Composition	Associated HU Values	ρ
'TG-43'	Mason *et al.*, Pope *et al.*	-Body -Outside Body	-TG-43 Reference Water -TG-43 Reference Air	-All -All	-Nominal -Nominal

Scheme Name	**Inspired By**	**Assigned Region**	**Tissue Composition**	**Associated HU Values**	**ρ**
'TG-186'	Miksys *et al.*	-Prostate	-Woodard and White Prostate	-All	-Nominal
		-Calcification	-Calcification*	-All	-Nominal
		-Outside Prostate in Body	-ICRU Mean Male Soft Tissue	-All	-Nominal
		-Outside Body	-TG-43 Reference Air	-All	-Nominal

Scheme Name	**Inspired By**	**Assigned Region**	**Tissue Composition**	**Associated HU Values**	**ρ**
'PC'	Miksys *et al.*	-Prostate	-Prostate -ICRU Breast Calcification	- Based on Varian Scanner	-CT-derived -CT-derived
		-Calcification	-ICRU Breast Calcification	- All	-CT-derived
		-Outside Prostate In Body	-ICRU Mean Male Soft Tissue	-Based on Varian Scanner	-CT-derived
		-Outside Body	-Cortical Bone	-All	-Nominal
			-TG-43 Reference Air	-All	-Nominal

Scheme Name	**Inspired By**	**Assigned Region**	**Tissue Composition**	**Associated HU Values**	**ρ**
'PC-20%'	Miksys *et al.*	-Prostate	-Prostate -ICRU Breast Calcification -20%p80%c -40%p60%c -60%p40%c -80%p20%c	-Based on Varian Scanner	-CT-derived
		-Calcification	-ICRU Breast Calcification	-Based on Varian Scanner	-CT-derived
		-Outside Prostate In Body	-ICRU Mean Male Soft Tissue	-Based on Varian Scanner	-CT-derived
		-Outside Body	-Cortical Bone -TG-43 Reference Air	-All	-Nominal

Scheme Name	Inspired By	Assigned Region	Tissue Composition	Associated HU Values	ρ
Worst-Case Scenario	Collins-Fekete *et al.*	-75% of the prostate	-Prostate	-All	-Nominal
		-25% of the prostate	-ICRU breast calcification	-All	-Nominal
		-Calcification	-ICRU breast calcification	-All	-Nominal
		-Outside Prostate in Body	-ICRU Mean Male Soft Tissue	-All	-Nominal
		-Outside Body	-TG-43 Reference Air	-All	-Nominal

The primary output of the selected tissue assignment scheme was a set of two 3D matrices, one containing the media selected for all voxels and another containing the densities selected for all voxels. To increase the simulation efficiency, matrices were truncated to a total image dimension of (20.1856 x 20.1856 x 20.5) cm^3, resulting in matrices that consisted of 159 x 159 x 82 voxels while preserving the voxel resolution of the planning CT image. The dimensions of the truncated matrices were chosen to ensure all relevant clinical structures were still contained within the simulation geometry. These truncated matrices were subsequently written slice-by-slice to an ASCIII file using the `DOSXYZnrc` *.egsphant format, along with a global list of all media referenced in the matrices and a list of the voxel boundaries for the output phantom [62]. Furthermore, a *.ramp file was created that defines the media density to medium conversion rules for the *.egsphant file. The *.ramp file specified that voxels with a mass density ρ (with units g cm^{-3}) between values *min_density_i* and *max_density_i* were assigned to medium *i* (assuming a default density of *default_density_i*). The media were specified in order by

increasing values of *max_density_i* so that the *.ramp file could be read correctly by egspp. Using the *.egsphant and *.ramp files, an egspp phantom geometry can be initialized with the patient heterogeneities dictated by the selected tissue assignment scheme.

5.6.3 Monte Carlo Simulation

Using MATLAB, the patient's treatment plan (stored as an RP-DICOM) was analyzed to determine the dwell positions (with coordinates expressed in millimetres) and weights associated with the ^{192}Ir microSelectron-v2 HDR source. Orientation information for each source was also extracted during this procedure. To avoid interseed attenuation and truly simulate a prostate brachytherapy delivery, data from the treatment plan was partitioned into separate simulations for each of the n source locations used in the treatment plan. This was accomplished by utilizing the file-writing capabilities of MATLAB to generate and name n separate egspp simulation files (with file format *.egsinp). Each *.egsinp file created in this process references the *.egsphant and *.ramp files in order to define the heterogeneous virtual patient phantom geometry. Following that, an oriented microSelectron-v2 HDR ^{192}Ir source was embedded within each phantom at the appropriate dwell position (with coordinates expressed in centimetres). While plastic catheters typically guide the source during clinical treatments, they were not modelled explicitly in the present work. The influence of the additional transit dose delivered as the source moves between dwell positions was also unassessed.

Using egspp to ensure that the proper dwell weights w were being taken into consideration was a notable challenge. However, this task was ultimately accomplished using the egspp EGS_SourceCollection class. It has a statistical weighting feature that ensures each source within a collection of sources is activated with a probabilistic weight based on the output of a random number generator. Unfortunately, this weighting feature did not work properly if a single source is used. Hence, a dummy source was placed alongside the microSelectron-v2 within the phantom geometry and given a statistical weighting of 1- w. To minimize the influence of the dummy source on the radiation field, it was defined as a monoenergetic point source emitting photons isotropically with energy $E = 10^{-10}$ MeV located at the origin of the phantom outside of the prostate and normal

tissues. As PCUT greatly exceeds the energy of photons emitted from the dummy source, the energy was deposited locally and was negligible compared to the dose deposition events stemming from the modelled ^{192}Ir source.

Simulations were distributed to an in-house computer cluster consisting of four nodes. Each of the n source collections (consisting of the microSelectron-v2 HDR ^{192}Ir source and the virtual source) was initialized with 500 million particle histories, ensuring that photons are emitted from the active core of the ^{192}Ir source with a w % probability. The dummy source was also activated with a (1- w) % probability during this process.

The current approach implemented for partitioning the simulation prevents the egspp simulation from combining all results automatically when all jobs submitted to the cluster have finished. Hence, the *.egsdat result files from all *n* simulations were renamed using a shell-script before results were combined in a separate step using `tutor7pp`'s "combine" mode. This combining process took approximately 20-30 minutes per patient-specific phantom, depending upon the number of *.egsdat result files being combined.

After normalizing energy deposition values by the number of histories per source collection (500 million), the absorbed dose per particle history D^{MC} for each region of the virtual phantom geometry was computed voxelwise by further dividing by the product of the volume V and density ρ. By default, the density value is derived from the heterogeneous *.egsphant file in order to score $D_{m,m}^{MC}$ (the absorbed dose reported to the local tissue m composing each voxel). Alternatively, the density value can be ignored and the absorbed dose $D_{w,m}^{MC}$ can be reported to a fixed reference water medium (with nominal density 0.998 g cm^{-3}).

To compare to clinical dose distributions, D^{MC} is converted to absolute dose (with units of cGy) by modifying an expression used by Poon *et al* [63].:

$$D_{abs}^{MC} = n \cdot \frac{D^{MC}}{S_K^{MC}} \cdot S_K^{exp} \cdot t_{w=1} \qquad (41)$$

Unlike studies performed by Poon *et al.* involving a single source, the activation weights of the source at all n dwell positions were already taken into account when the master file

combined the partitioned simulations. Hence, each source was not multiplied by its own dwell time during the conversion to absolute dose but rather the longest dwell time in the plan (associated with a dwell weight of w = 1). It is designated $t_{w=1}$ in the above expression, with units of hours. S_K^{exp} is the air kerma strength of the clinical source at the time of implant, as computed by Oncentra Brachy (Elekta Brachytherapy Solutions, Veenendaal, The Netherlands). It is expressed in units of U (1 U = 1 cGy cm^2 h^{-1}). Finally, S_K^{MC} is the Monte Carlo calculated air kerma strength per history of the source (as previously evaluated during source validation).

Prior to plan evaluation, the extent and variability of dose uncertainties to voxels within treatment structures (prostate and calcification) and OARs (urethra, rectum and bladder) was assessed using box-and-whisker-plots. These plots visually represent the mean and median dose uncertainty values, quartiles and maximal outliers. Under the recommendations of AAPM's TG-56 regarding the code of practice for brachytherapy physics, computer-assisted dose calculations should have a numerical accuracy of at least ± 2% in all structures of interest [30].

Table 9 Clinical dose objectives for ^{192}Ir HDR brachytherapy prostate plan at the Nova Scotia Cancer. These targets have been adapted from the Sunnybrook technique by Morton *et al* [26].

Structure	Clinical Metric	Objective
Prostate	V_{100}	$\geq$ 95%
	V_{150}	$<$ 135%
	V_{200}	$<$ 11 %
Urethra	D_{10}	$<$ 118%
Rectum	V_{80}	$<$ 0.5 cc

Plans were evaluated by assessing the cumulative dose volume histograms (cDVHs) for all structures referenced in the dose objectives (the prostate, urethra and rectum). The clinical dose metrics considered in this study are an adaptation of metrics used in the Sunnybrook technique by Morton *et al*. and are listed in Table 9 [31]. For all MC

calculated absolute dose distributions derived using a tissue assignment scheme, dose metrics were determined by linearly interpolating between cDVH values. This facilitates a comparison with respect to both the clinical Oncentra Brachy (Elekta Brachytherapy Solutions, Veenendaal, The Netherlands) dose distribution and other Monte Carlo dose distributions run using other tissue assignment schemes.

Chapter 6 RESULTS AND DISCUSSION

6.1 Source Validation

6.1.1 Radial Dose Functions $g(r)$

Figures 5 and 6 directly compare the radial dose functions $g_L(r)$ and $g_P(r)$ computed in the current study using egspp to Taylor *et al.*'s results calculated with the BrachyDose MC code [54] [55]. Discrepancies did not exceed ±1% for any of the interpolated tabulated values, indicating strong agreement with Taylor *et al.* [54] [55]. Furthermore, results from the current study satisfied the 2007 High Energy Brachytherapy Dosimetry group (HEBD) recommendation of ≤ 5% agreement for $g_L(r)$ between MC results and a dataset derived from a well-benchmarked code such as BrachyDose [56].

The maximum absolute percent discrepancies for both $g_L(r)$ and $g_P(r)$ occurred at r = 0.70 cm (0.795% and 0.912% respectively). The change in concavity exhibited in simulated $g_L(r)$ data (Figure 5) occurred at this radial distance and was not observed in the BrachyDose comparison results. Furthermore, radial dose function values within $r <$ 1 cm were associated with a larger mean absolute percent discrepancy (0.367% for $g_L(r)$ and 0.388% for $g_P(r)$) compared to $r \geq 1$ cm (0.151% for $g_L(r)$ and 0.166% for $g_P(r)$).

It is unclear what is responsible for the larger average discrepancies within 1 cm of the source. These effects are not associated with a breakdown in electronic equilibrium nor from neglecting the beta spectrum of ^{192}Ir (with a 181 keV average energy), as errors exceeding 2% attributable to electronic disequilibrium are only exhibited at or below 1.6 mm for ^{192}Ir and BrachyDose neglects contributions from the beta spectrum. However, dose values at tabulated radii were calculated using a bilinear interpolator prior to division by the appropriate geometry function values. Both geometry functions depend upon the quantity $1/r^2$, which increases rapidly with decreasing radial distance from the center of the source and may be responsible for this effect. In contrast, the comparison data divided all dose values by the geometry function prior to bilinear interpolation. The difference between the calculation methods in conjunction with the interpolation may be the cause of the larger average discrepancies when $r < 0.7$ mm.

The systematic underestimations exhibited at the tabulated values of r = 5 cm and r = 10 cm are likely voxel size effects attributable to the manner in which voxel dimensions were selected within the phantom and greatly exceed all other discrepancies for nearby r. The indicated radial distances represent the threshold between two subsets of voxels with different dimensions (e.g. the r = 5 cm threshold separates (0.5 x 0.5 x 0.5) mm^3 voxels from (1.0 x 1.0 x 1.0) mm^3 voxels). During calculation of $g(r)$, however, only a single voxel grid (e.g. a grid of smaller (0.5 x 0.5 x 0.5) mm^3 voxels for r = 5 cm) was used. Considering the smaller number of photon interactions at this distance and the source anisotropy, dose scored in off-axis voxels may be significantly lower than at the reference location (r = 1 cm, $\theta = \theta_0 = 90°$) and $g(r)$ would ultimately be diminished. A weighted interpolation based on voxel size may ameliorate this issue.

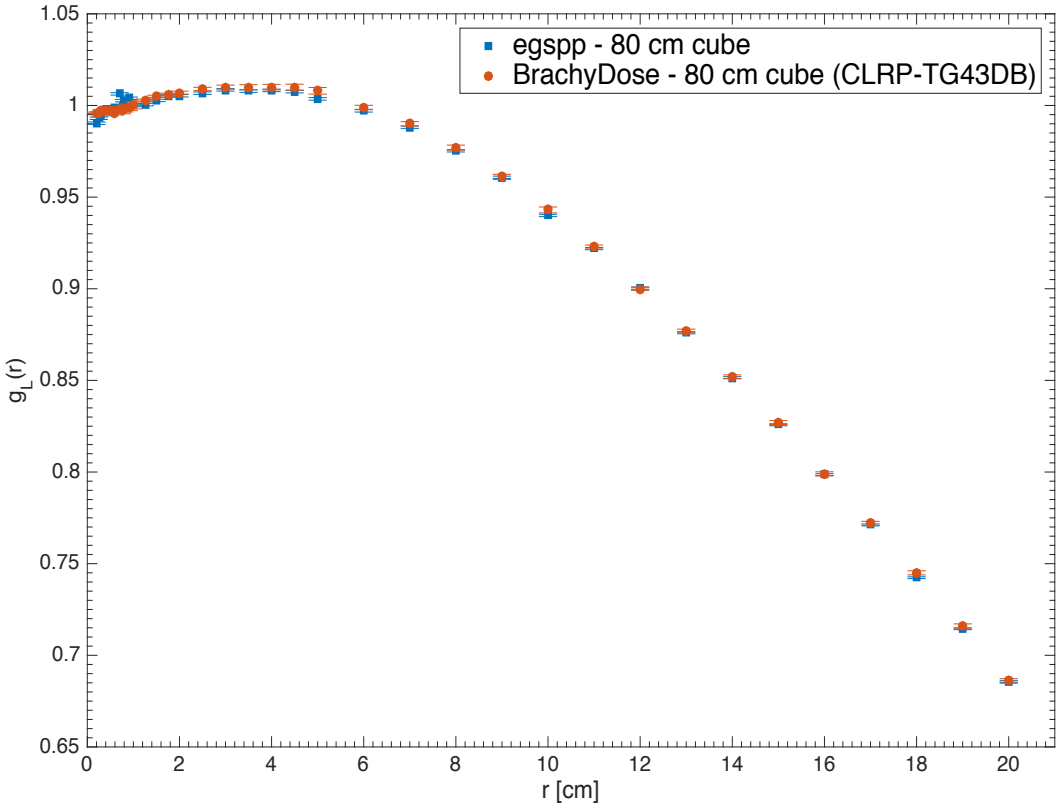

Figure 5 Radial dose function data, $g_L(r)$, calculated using the line-source approximation for a microSelectron v2 source model located at the center of an (80 cm)^3 voxelized water phantom. Simulation results (blue squares) are compared to data from Taylor *et al.* (red circles) [54] [55], computed using a similar geometry with the EGSnrc code BrachyDose.

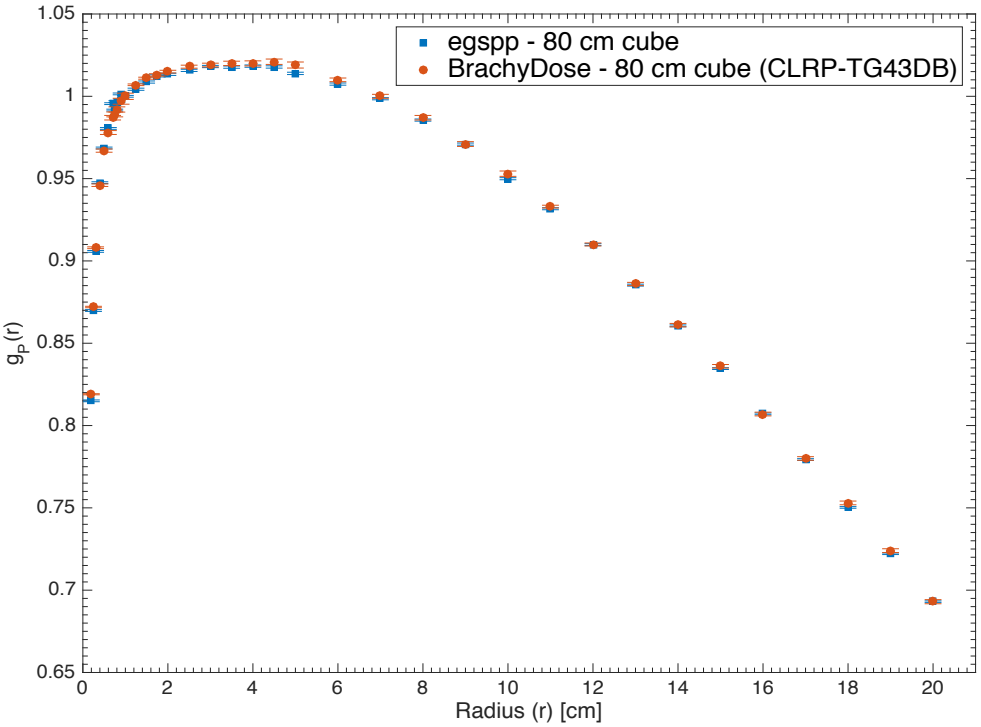

Figure 6 Radial dose function data, $g_P(r)$, calculated using the line-source approximation for a microSelectron v2 source model located at the center of an (80 cm)^3 voxelized water phantom. Simulation results (blue squares) are compared to data from Taylor *et al.* (red circles) [54] [55], computed using a similar geometry with the EGSnrc code BrachyDose.

6.1.2 Anisotropy Functions $F(r,\theta)$

The anisotropy function $F(r,\theta)$ was evaluated at three radial distances from the center of the source (r = 0.50 cm, r = 1.00 cm and r = 5.00 cm) using 47 polar angles dispersed over the range $0° \leq \theta \leq 180°$. Figures 7, 8 and 9 display the calculated $F(r,\theta)$ curves and compares to results obtained from BrachyDose by Taylor *et al*. for an identical geometry and results from Daskalov *et al* [54] [55] [56] [57]. For F(r = 1.00 cm, θ) and F(r = 5.00 cm, θ), results are further compared to the AAPM-ESTRO HEBD Working Group's Consensus Dataset [60]. Calculated data is generally in very good agreement with all references considered, especially for tabulated values in which θ is in close proximity to the transverse plane angle $\theta = \theta_0 = 90°$. In particular, tabulated anisotropy values agree within ±2% of tabulated values from BrachyDose for $50° \leq \theta \leq 125°$ (r = 0.50 cm), $20° \leq \theta \leq 140°$ (r = 1.00 cm) and $15° \leq \theta \leq 180°$ (r = 5.00 cm).

All calculated anisotropy functions satisfy the 2007 HEBD recommendation of ≤ 10% agreement for $F(r,\theta)$ between MC results and the benchmarked dataset BrachyDose within 5° of the source longitudinal axis (i.e. the line aligned with $\theta = 0°$ and $\theta = 180°$), with the exception of points located on the source longitudinal axis itself [60]. For $F(r = 0.50 \text{ cm}, \theta)$, the egspp-calculated function over-estimates BrachyDose by 5.75% above the source (θ = 1°) and under-estimates BrachyDose by 4.28% above the source (θ = 173°). The abrupt deviation observed at θ = 180° could not be compared, as it was not evaluated by BrachyDose. For r = 1.00 cm and r = 5.00 cm, the maximum discrepancies above and below the source are 6.21% and 20.0% (θ = 1° and θ = 180°) and 5.22% and 1.60% (θ = 0° and θ = 178°), respectively. Note that the maximum discrepancy at locations below the source and off the longitudinal axis for r = 1.00 cm is 3.97%, possibly indicating that θ = 180° values may be unreliable if r is too close to the source.

Since the entire active length of the source is aligned with the longitudinal axis, the absorbed dose within voxels in close vicinity to the longitudinal axis is decreased significantly due to increased self-absorption within the core and oblique filtration caused by the encapsulation and the steel driving cable. The resultant dose gradients are highly uncertain, particularly at close radial distances r, and more dependent on differences in source modeling relative to other regions of the dose distribution. Hence, the region within 5° of the source axis (>175° and < 5°) ignored by the HEBD 2007 recommendations is naturally associated with the maximum discrepancies observed for all anisotropy functions.

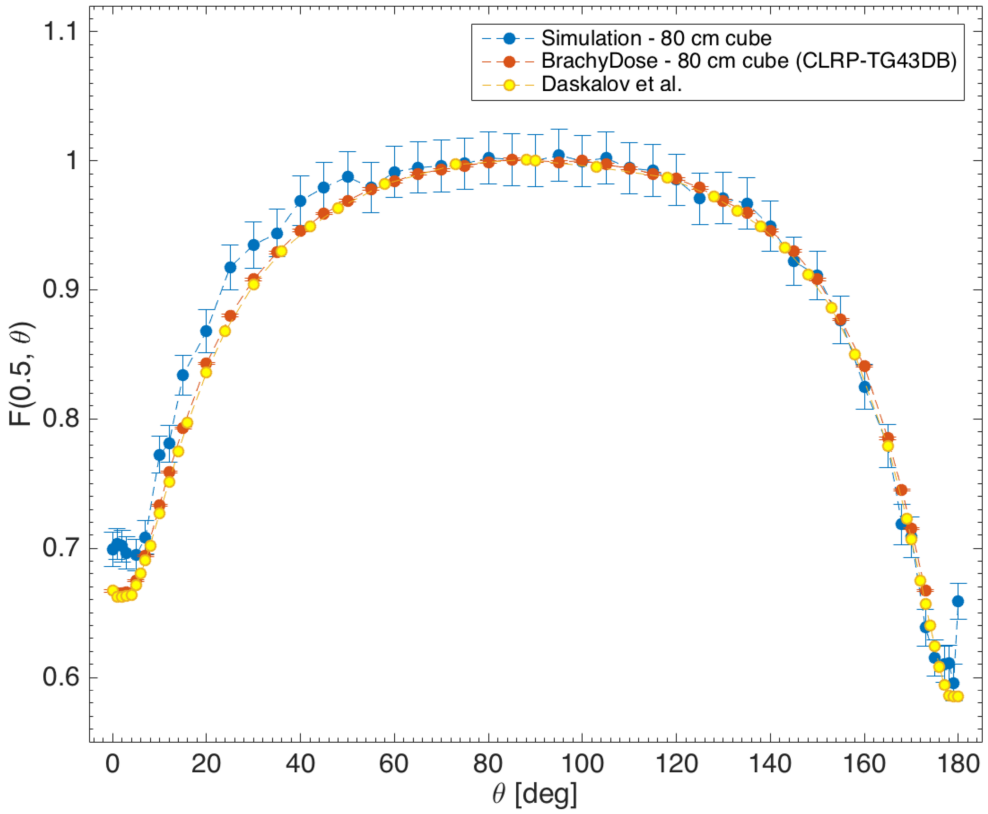

Figure 7 Anisotropy function calculated at a radial distance of $r = 0.5$ cm, $F(0.5, \theta)$, calculated using the line-source approximation for a microSelectron v2 source model located at the center of an (80 cm)^3 voxelized water phantom. Simulation results (blue squares) are compared to data from Taylor *et al.* (red circles) [52], computed using a similar geometry with the EGSnrc code BrachyDose, and Daskalov *et al.* (yellow circles), computed using MCPT [53] [54].

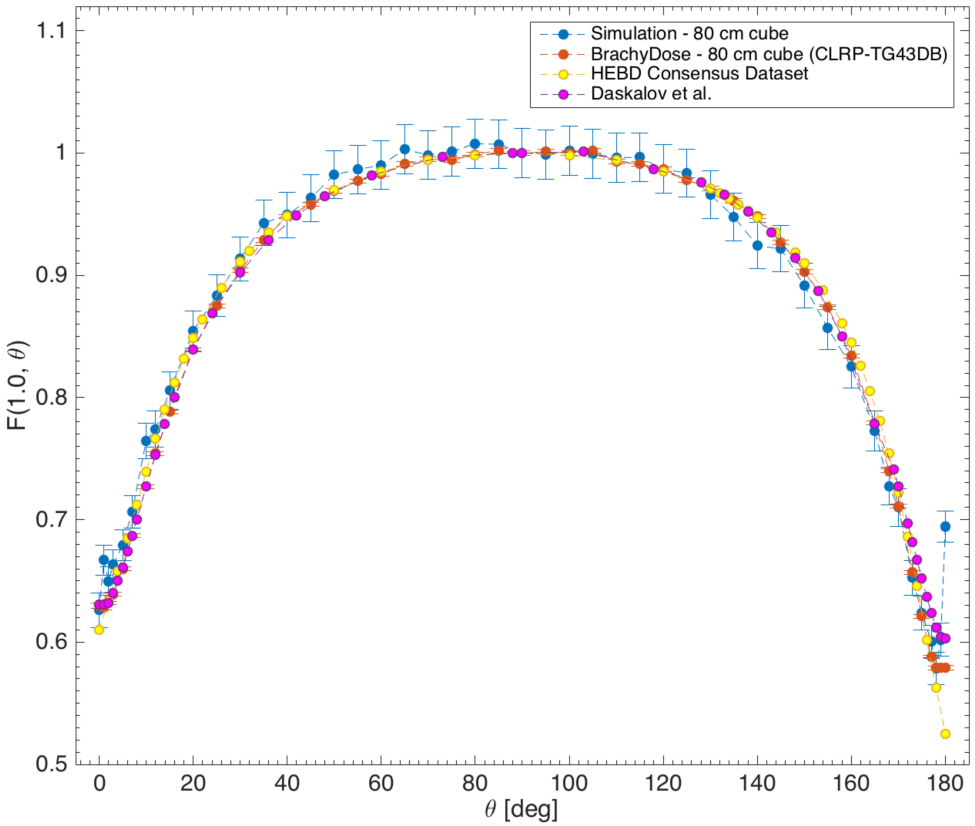

Figure 8 **Anisotropy function calculated at a radial distance of $r = 1.0$ cm, $F(1.0, \theta)$, calculated using the line-source approximation for a microSelectron v2 source model located at the center of an (80 cm)^3 voxelized water phantom. Simulation results (blue squares) are compared to data from Taylor *et al.* (red circles) [55], computed using a similar geometry with the EGSnrc code BrachyDose, the HEBD Consensus Dataset (yellow circles) [60] and Daskalov *et al.* (purple circles), computed using MCPT [56] [57].**

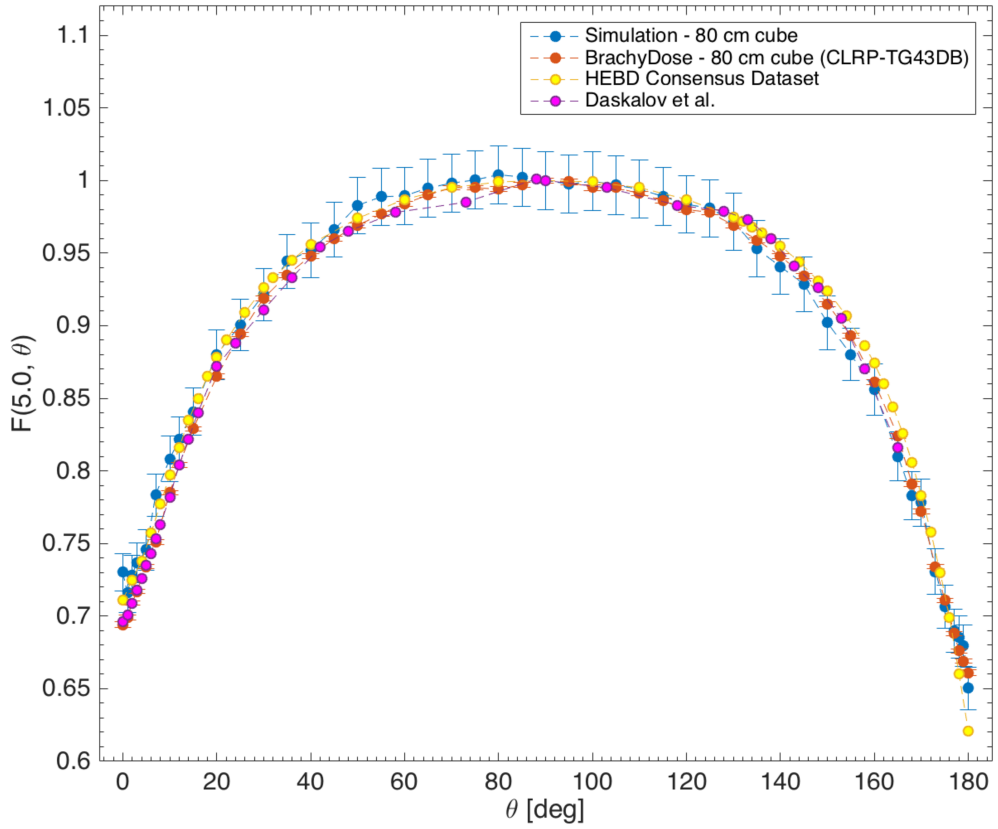

Figure 9 **Anisotropy function calculated at a radial distance of $r = 5.0$ cm, $F(5.0, \theta)$, calculated using the line-source approximation for a microSelectron v2 source model located at the center of an (80 cm)^3 voxelized water phantom. Simulation results (blue squares) are compared to data from Taylor *et al.* (red circles) [54], computed using a similar geometry with the EGSnrc code BrachyDose, the HEBD Consensus Dataset (yellow circles) [60] and Daskalov *et al.* (purple circles), computed using MCPT [56] [57].**

6.1.3 Dose Rate Constant Λ and Air Kerma Strength Per History S_K^{MC}

Using 10^{11} particle histories and the method discussed in Chapter 5, S_K^{MC} was calculated to be 1.10 x ± 0.07 10^{-24} cGy cm^2. The dose to water per history (computed using 10^{11} particle histories) was 1.21 ± 0.06 x 10^{-24} cGy cm^2. Λ was then calculated by dividing the former quantity by the latter. In this study, it was determined that Λ = 1.102 ± 0.089. While the propagated uncertainty is approximately ±8%, this value agreed with the value calculated by Taylor *et al.* using BrachyDose (Λ = 1.109 ± 0.002) within 0.64%. Hence, the calculation has met the HEBD 2007 benchmarking criteria requiring that Λ values between codes agree within 2%. That said, it is important to note that S_K^{MC} is seldom reported in the literature and could not be validated explicitly.

6.2 Calcified Phantom Simulations

6.2.1 5 mm Separation Distance

The radial distance between the calcification and the center of the microSelectron-v2 was first fixed to $r = 5$ mm along the x-axis. Figure 10 compares the dose profile through the center of the source and a calcification with radius r_c = 1 mm and volume V = 0.00419 cc to the same profile calculated in a water phantom, along with the associated relative percent dose difference between the profiles. Voxels that overlap with the calcification were neglected from the top plot. Table 10 also reports values of $\Delta D_{rel,\ d\mu}$, $\Delta D_{rel,\ dmin}$ and $\Delta D_{rel,\ dmax}$ for three distances relative to the calcification center (d = 2.5 cm, d = 5.0 cm and d = 7.5 cm). $\Delta D_{rel,\ d\mu}$ remained relatively constant for all distances assessed, suggesting that the attenuation-related effect (starting after x = 0.5 cm in Figure 10) persists for the remainder of the scoring grid. However, the effect within d = 2.5 cm was slightly more pronounced ($\Delta D_{rel,\ 2.5\mu}$ = -1.84%). This is attributable to the increasing prominence of statistical fluctuations and high statistical uncertainties with further distances away from the calcification center. While this resulted in larger reductions in dose within the calcified phantom ($\Delta D_{rel,\ 7.5min}$ = -5.60%), increases in dose were also observed (e.g. $\Delta D_{rel,\ 7.5max}$ = 2.14%).

Table 10 The distance metrics $\Delta D_{rel,\ d\mu}$, $\Delta D_{rel,\ dmin}$ and $\Delta D_{rel,\ dmax}$ for three different distances (d = 2.5 cm, d = 5.0 cm, and d = 7.5 cm) and two different calcification radii (r_c = 1 mm and r_c = 3 mm).

Calcification Radius r_c [mm]	r_c = 1 mm	r_c = 3 mm
$\Delta D_{rel,\ 2.5\mu}$	-1.84%	-7.42%
$\Delta D_{rel,\ 2.5min}$	-2.78%	-8.85%
$\Delta D_{rel,\ 2.5max}$	-0.41%	-5.31%
$\Delta D_{rel,\ 5.0\mu}$	-1.57%	-7.17%
$\Delta D_{rel,\ 5.0min}$	-4.25%	-9.52%
$\Delta D_{rel,\ 5.0max}$	1.55%	-3.76%
$\Delta D_{rel,\ 7.5\mu}$	-1.48%	-6.80%
$\Delta D_{rel,\ 7.5min}$	-5.60%	-10.34%
$\Delta D_{rel,\ 7.5max}$	2.14%	-0.07%

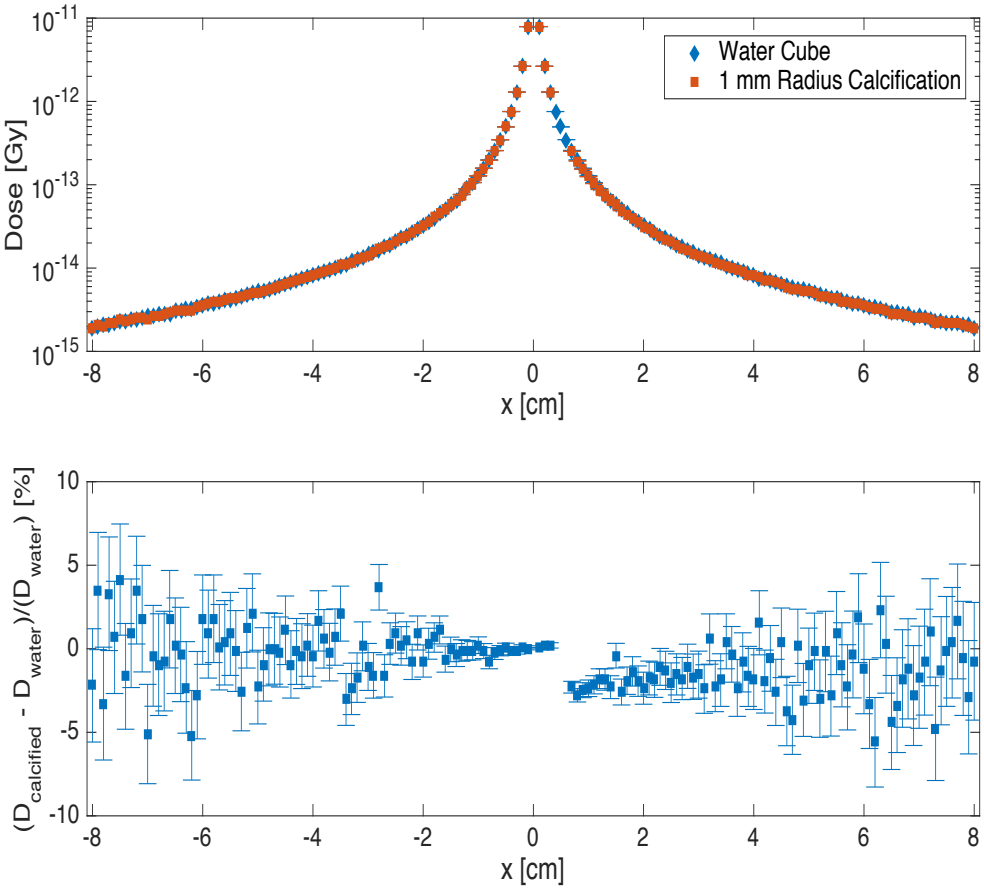

Figure 10 **In the upper plot, the dose profile passing through the center of the microSelectron-v2 source (at the origin) and the center of a 1 mm calcification placed 5 mm away is compared with the same profile in water. Red points have been removed if the voxels involved overlap with the calcification within the gridded geometry. In the lower plot, the corresponding relative dose difference is plotted along the direction of the profile. A mean effect of -1.84% was observed beyond the calcification.**

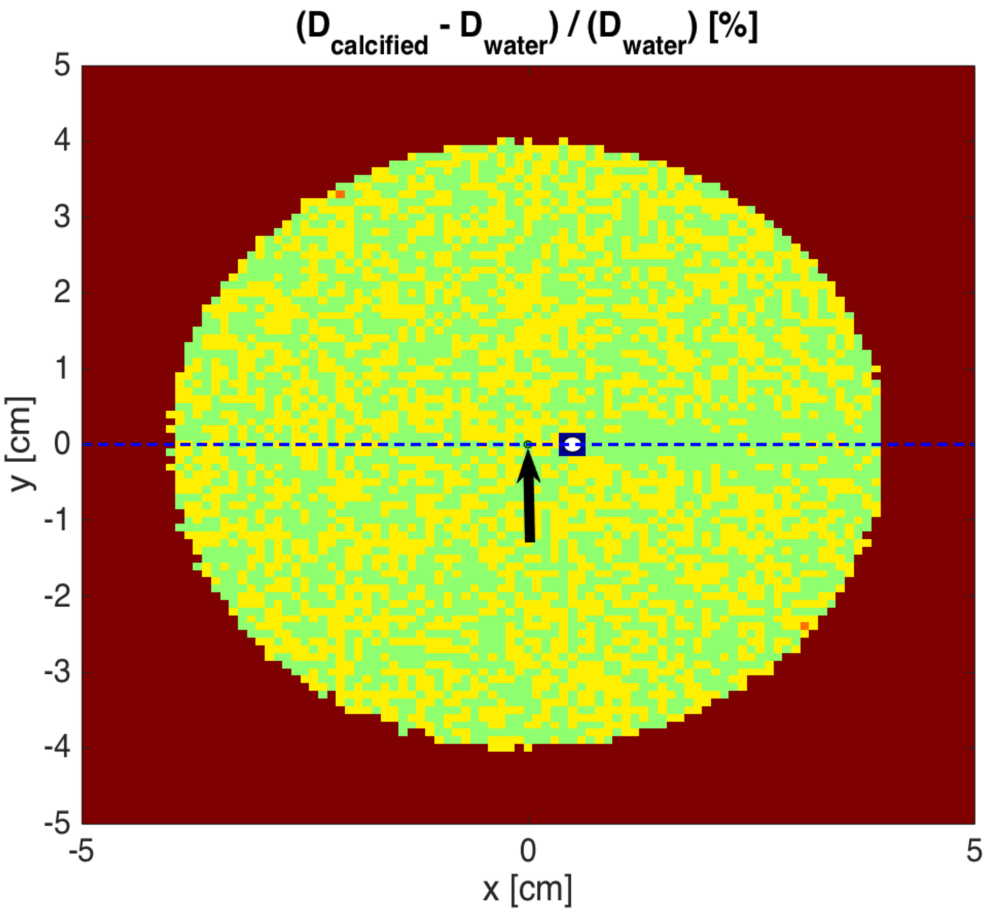

Figure 11 **An axial slice through the relative dose difference distribution that passes through the center of the microSelectron-v2 source (represented by the black arrow) and the center of the 1 mm radius calcification (white dot). The separation between source center and calcification center is 5 mm. Voxels with statistical uncertainties > 2% were coloured dark red, while yellow voxels represent 0-5% dose gains and green voxels represent 0-5% dose reductions. Black voxels indicate areas where the calcification overlaps with the gridded geometry. 0-5% dose reductions are frequently observed along the indicated profile.**

Figure 11 displays the relative dose difference map for the central (2 x 2) cm^2 axial slice where the black arrow represents the microSelectron-v2 source center and the white dot represents the calcification. The blue dashed line represents the dose difference profile exhibited in Figure 10, while the black voxels represent locations where the calcification overlaps with the gridded geometry. As the sensitive volume of these voxels were not the same as the other scoring voxels, they were ignored in this analysis. The green voxels indicate locations where the dose reduction is 1-5%, while the yellow voxels indicate regions where no reduction is observed (0-5% gain in dose). In accordance with the recommendations of TG-56 regarding the accuracy of computer-based dose calculation algorithms, all voxels with a statistical uncertainty exceeding 2% have been coloured dark red. The occasional light red voxel along the periphery of the coloured area indicates a dose gain of 5-10%.

A similar analysis was performed for a calcification with radius r_c = 3 mm and volume V = 0.11 cc for the same fixed separation distance $r = 5$ mm. Figure 12 displays the dose profiles associated with the calcified and non-calcified phantoms, along with the relative dose difference profile passing through the center of the calcification and the source center. Voxels that overlapped with the calcification were neglected from the top plot here as well. The observable separation of the dose profiles in the upper plot of Figure 12 demonstrates that a slight increase in r_c can have an observable dosimetric impact. This is corroborated by considering the distance metrics $\Delta D_{rel,\ d\mu}$, $\Delta D_{rel,\ dmin}$ and $\Delta D_{rel,\ dmax}$ considered earlier, which have also been compiled in Table 10. Once again, the shadowing effect caused by the calcification persisted for all distances within the scoring grid (d = 7.5 cm). $\Delta D_{rel,\ 2.5\mu}$, $\Delta D_{rel,\ 5.0\mu}$, and $\Delta D_{rel,\ 7.5\mu}$ were -7.42%, -7.17% and -6.80% respectively, while the minimum dose difference metric within 2.5 cm of the source was $\Delta D_{rel,\ 2.5max}$ = -8.85%. No dose enhancement was observed beyond the calcification for the scoring grid used, as the maximum dose difference metric was $\Delta D_{rel,\ 7.5max}$ = -0.07%.

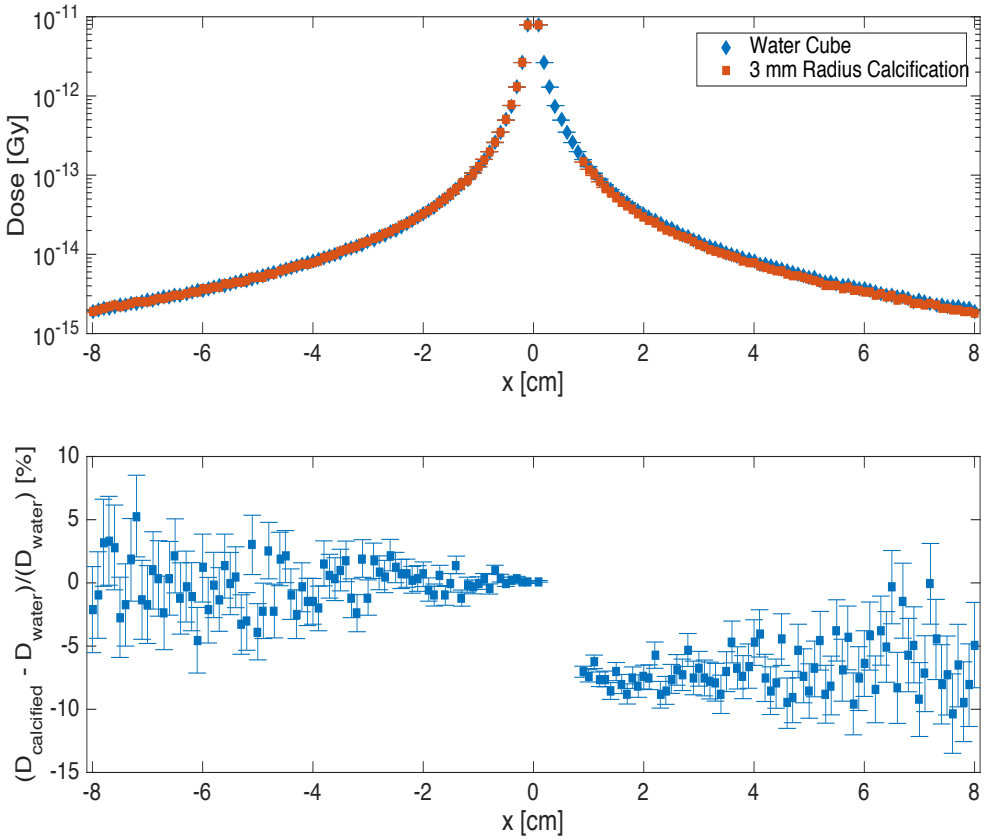

Figure 12 **In the upper plot, the dose profile passing through the center of the microSelectron-v2 source (at the origin) and the center of a 3 mm calcification placed 5 mm away is compared with the same profile in water. Red points have been removed if the voxels involved overlap with the calcification within the gridded geometry. In the lower plot, the corresponding relative dose difference is plotted along the direction of the profile. A mean effect of -6.80% was observed beyond the calcification.**

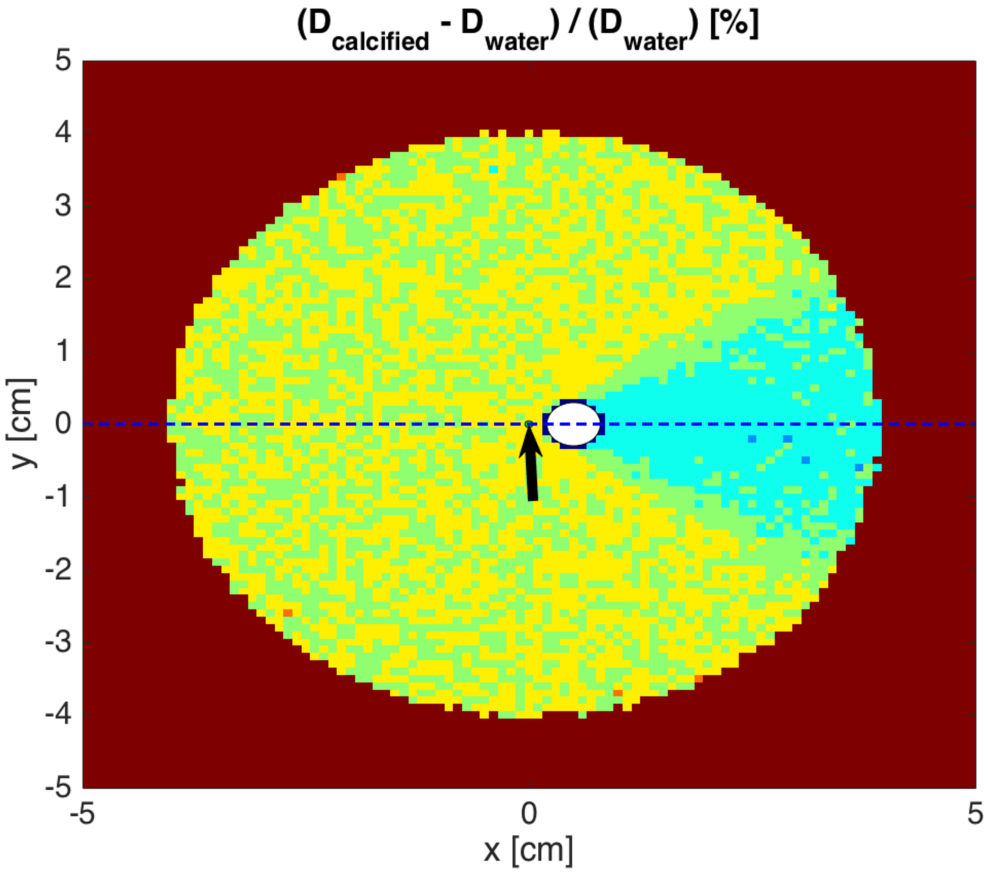

Figure 13 **An axial slice through the relative dose difference distribution that passes through the center of the microSelectron-v2 source (indicated by the black arrow) and the center of the 3 mm radius calcification (indicated by the white dot). The separation between source center and calcification center is 5 mm. Light blue voxels indicate areas with a 5-10% dose reduction, while dark blue voxels represent areas with a >10% dose reduction. Light green voxels represent a 0-5% dose reduction, while yellow voxels and red voxels indicate dose gains of 0-5% and >10%, respectively. The black voxels indicate regions where the calcification overlaps with the gridded geometry. Larger dose reductions of 5-10% are observed along the indicated profile, and the dosimetric effect has a larger spatial extent in the y-direction.**

Figure 13 is similar to Figure 11 and visualizes the relative dose difference map associated with the central (3 x 3) cm^2 slice for the larger calcification. The dark blue dashed line indicates the dose difference profile exhibited in the bottom plot of Figure 12. The same colour convention utilized to generate Figure 11 has been adopted here, although Figure 13 features a few additional colours. The lighter blue voxels indicate regions with a 5-10% dose reduction, while the dark blue indicates voxels with a dose reduction greater than 10%. Again, voxels with a statistical uncertainty exceeding 2% have been assigned a threshold colour of dark red. Qualitatively, the dosimetric effect in Figure 13 is more structured and has a larger spatial extent in the y-direction compared to Figure 11 (attributable to the minor increase in r_c). Hence, results indicate that a moderately sized heterogeneity can cause a moderate dose reduction that persists up to distances approaching the typical spatial extent of a prostate (2-4 cm).

For completeness, dose and relative dose difference profiles along the y- and z-axes are shown for a 3mm radius calcification in Figures 14 and 16. It is important to note that these profiles only go through the calcification center and do not align with the source center. Again, voxels that overlap with the calcification have been neglected from the dose profiles. Qualitatively, the profiles and statistical fluctuations are relatively symmetric about the origin. However, the distance metrics for these plots have not been quantified in light of Figures 15 and 17 (the corresponding coronal and sagittal relative dose difference maps). These plots (computed using the same colour convention used in Figures 11 and 13) indicate that any large relative dose discrepancies for the indicated profiles are entirely manufactured by the statistical fluctuations at large distances from the source. It is important to note that the structured green and black regions observed in Figure 15 indicate the location and dimensions of the source and driving cable and are not dosimetric effects. That said, 0-5% dose reductions (represented by the green voxels) are observed along both dashed blue profiles in Figures 15 and 17.

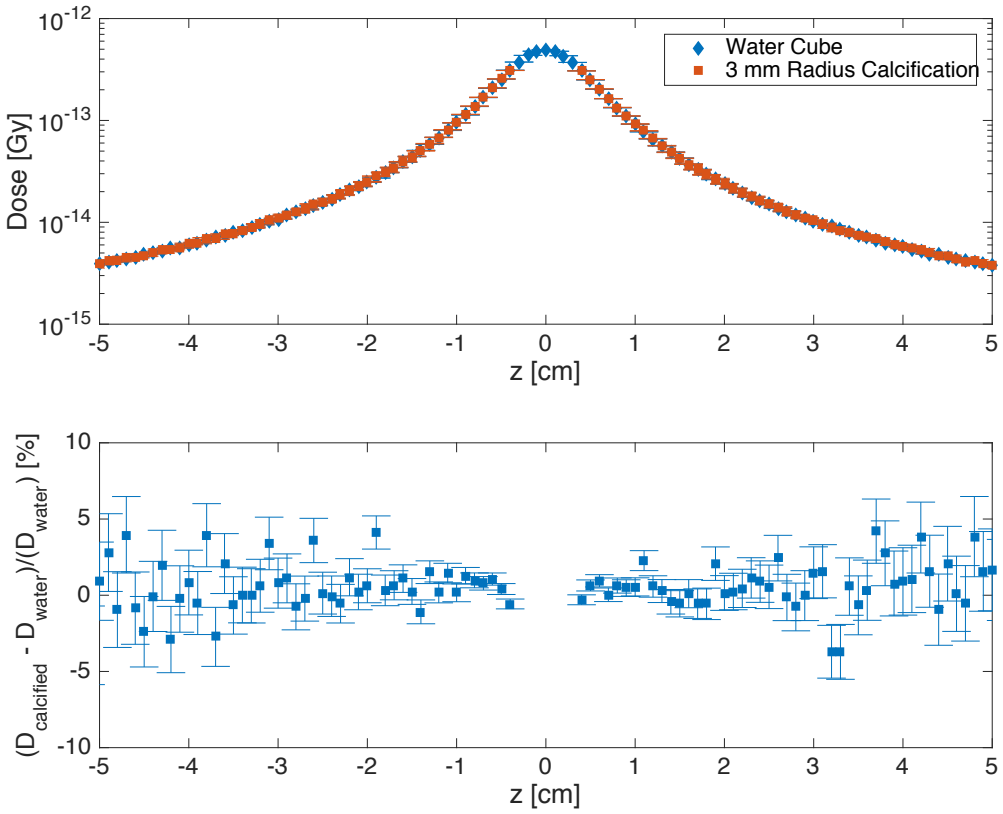

Figure 14 **In the upper plot, the dose profile passing the center of a 3 mm calcification placed 5 mm away oriented parallel to the source's longitudinal axis is compared with the same profile in water. Red points have been removed if the voxels involved overlap with the calcification within the gridded geometry. In the lower plot, the corresponding relative dose difference is plotted along the direction of the profile. The dose distribution was hardly perturbed by the calcification along this profile.**

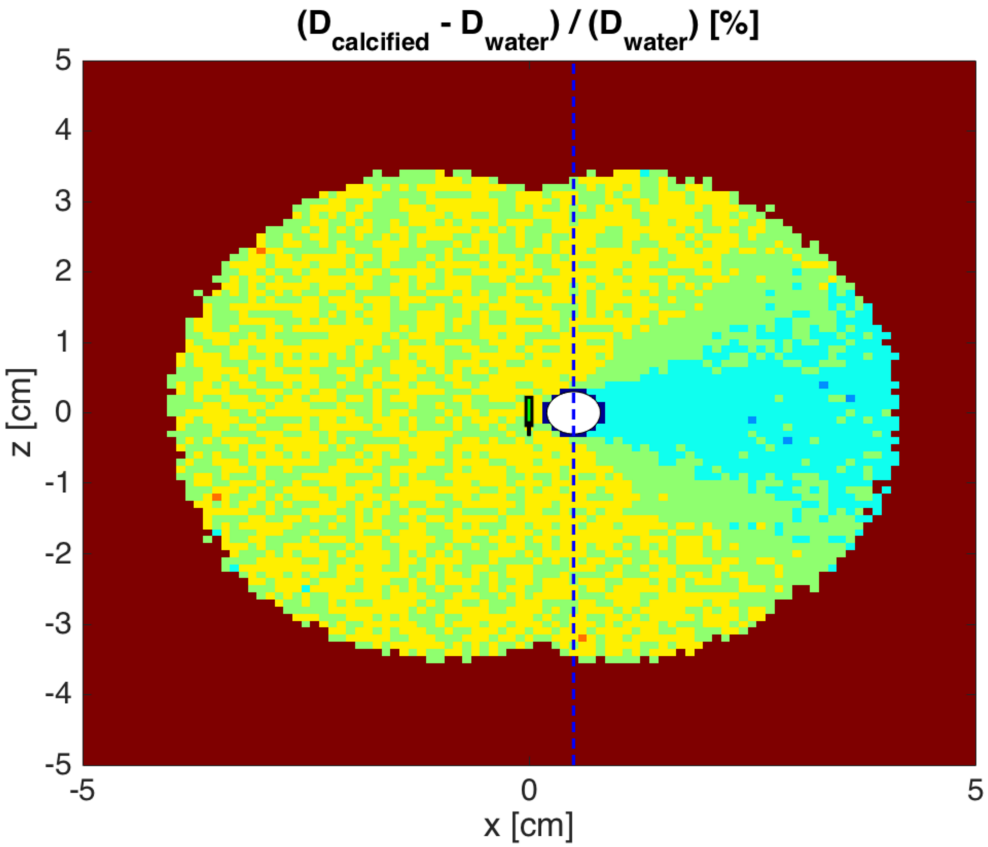

Figure 15 **A coronal slice through the relative dose difference distribution that passes through the center of the microSelectron-v2 source (represented by the green and black rectangles to scale) and the center of the 3 mm radius calcification (represented by the white dot). The separation between source center and calcification center is 5 mm. The same colour convention is used as in Figure 13 and regions of 0-5% dose reductions are observed along the profile indicated in dark blue. However, the dosimetric effect along this profile is mild.**

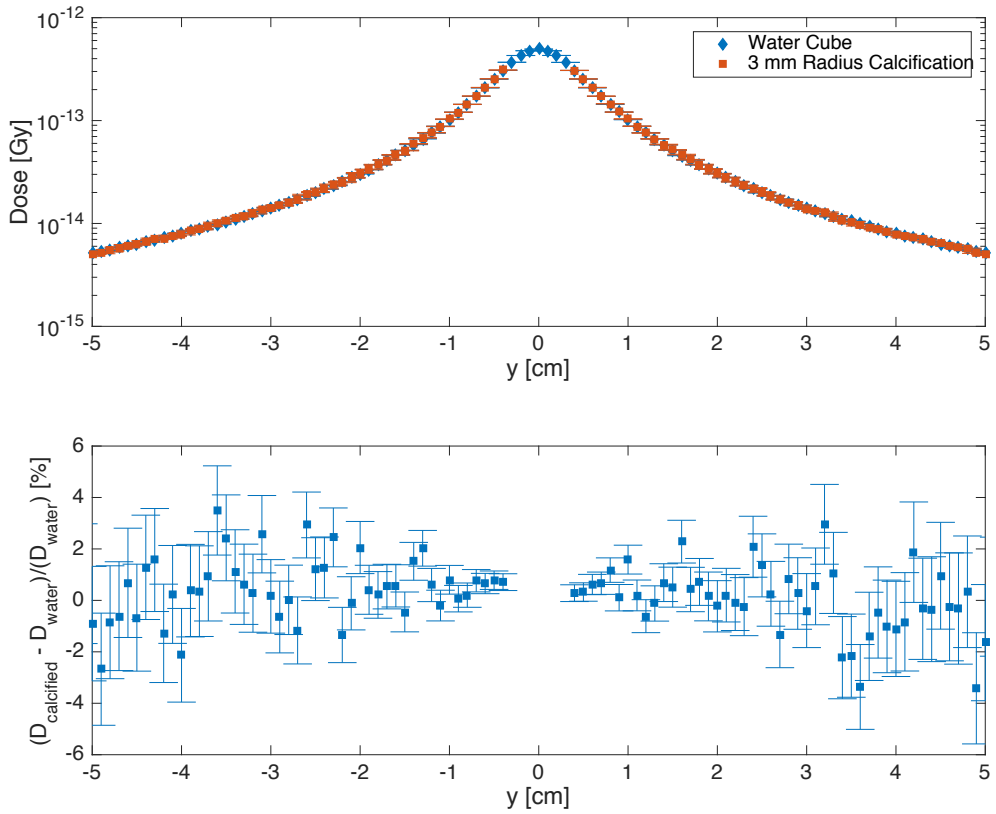

Figure 16 **In the upper plot, the dose profile passing the center of a 3 mm calcification 5 mm away from the microSelectron-v2 source is compared with the same profile in water. This particular profile is oriented perpendicular to the source's longitudinal axis and its center. Red points have been removed if the voxels involved overlap with the calcification within the gridded geometry. In the lower plot, the corresponding relative dose difference is plotted along the direction of the profile. As in Figure 14, the dose distribution was hardly perturbed by the calcification along this profile.**

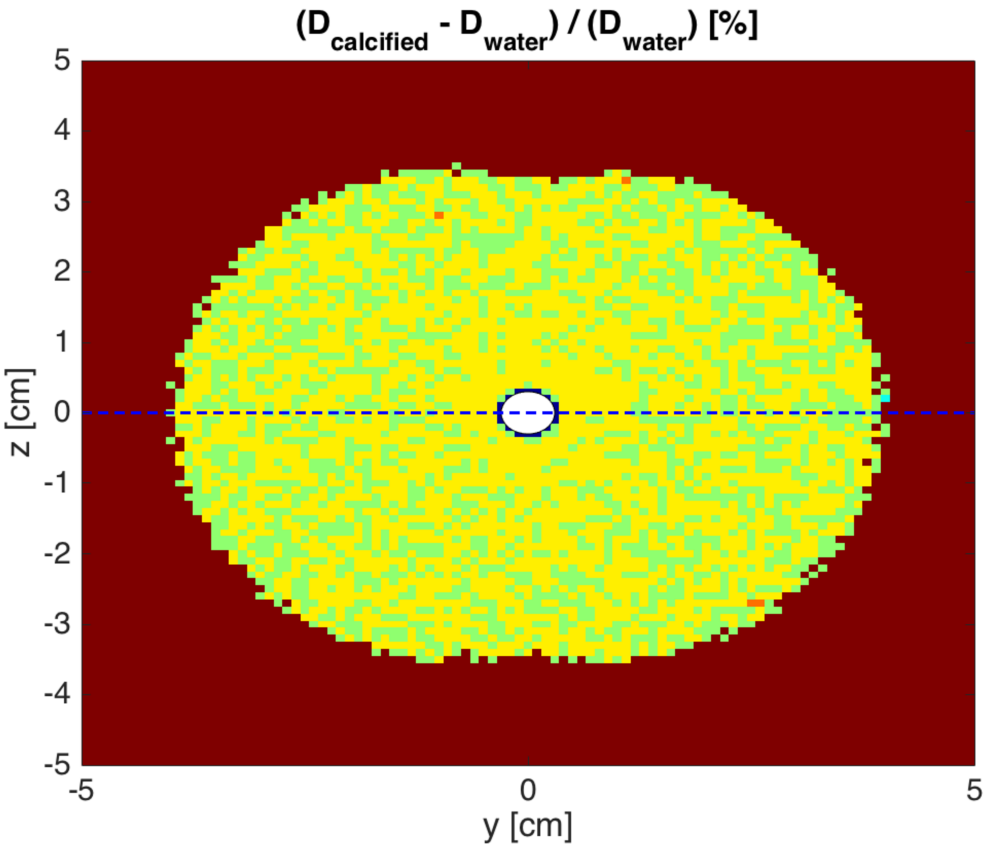

Figure 17 **A sagittal slice through the relative dose difference distribution that passes through the center of the microSelectron-v2 source and the center of the 3 mm radius calcification. The separation between source center (not observable on this slice) and calcification center is 5 mm. The same colour convention is used as in Figure 13 and regions of 0-5% dose reductions are observed along the profile indicated in dark blue. However, the dosimetric effect along this profile is mild.**

6.2.2 5 cm Separation Distance

To consider the effect of calcifications far from the microSelectron-v2 source, the radial separation distance was increased to $r = 5$ cm along the egspp x-axis. Figures 18 and 19 compare dose profiles through the center of the source and the calcification (r_c = 1 mm and r_c = 3 mm, respectively), along with the associated relative percent dose differences between the profiles. Again, voxels that overlap with the calcification have been removed from the dose difference plots. Coronal and sagittal planes were neglected based upon the earlier analysis.

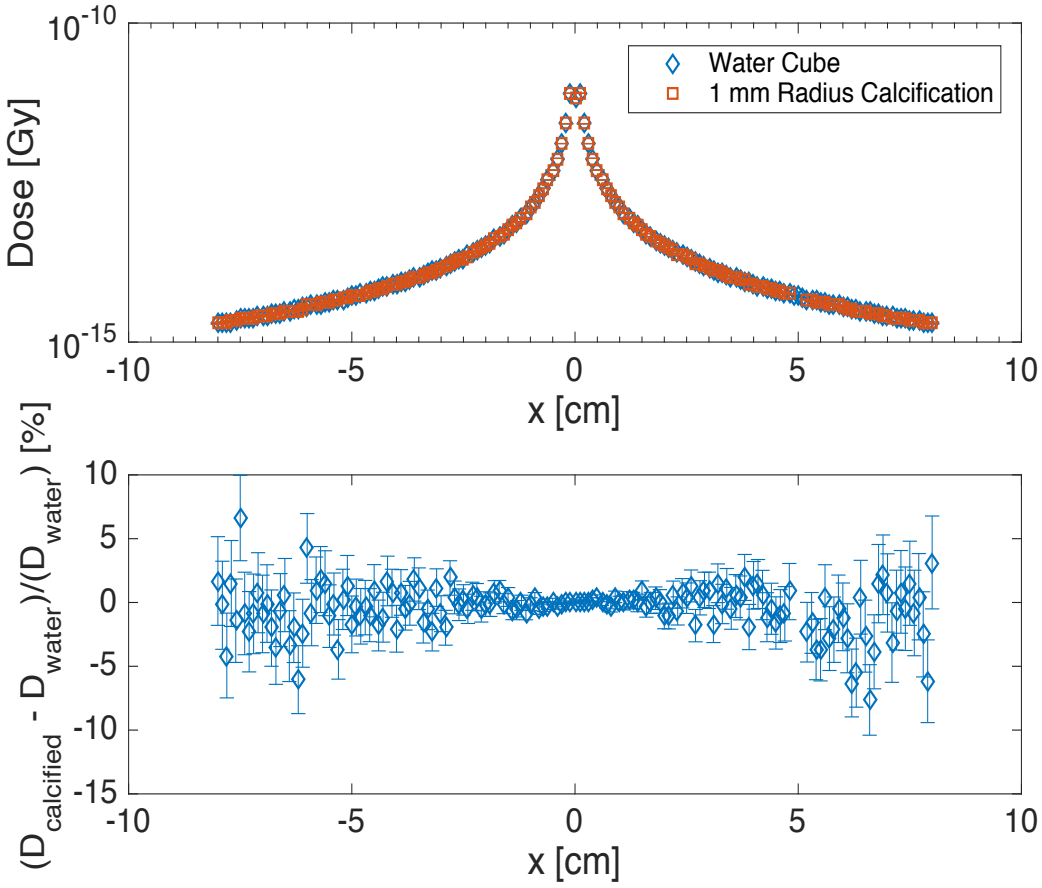

Figure 18 **In the upper plot, the dose profile passing through the center of the microSelectron-v2 source (at the origin) and the center of a 1 mm calcification placed 5 cm away is compared with the same profile in water. Red points have been removed if the voxels involved overlap with the calcification within the gridded geometry. In the lower plot, the corresponding relative dose difference is plotted along the direction of the profile. A mean effect of -1.70% was observed beyond the calcification, compared to -1.84% for the same sized calcification when $\Delta D_{rel,\ 2.5\mu}$ was calculated at r = 5 mm.**

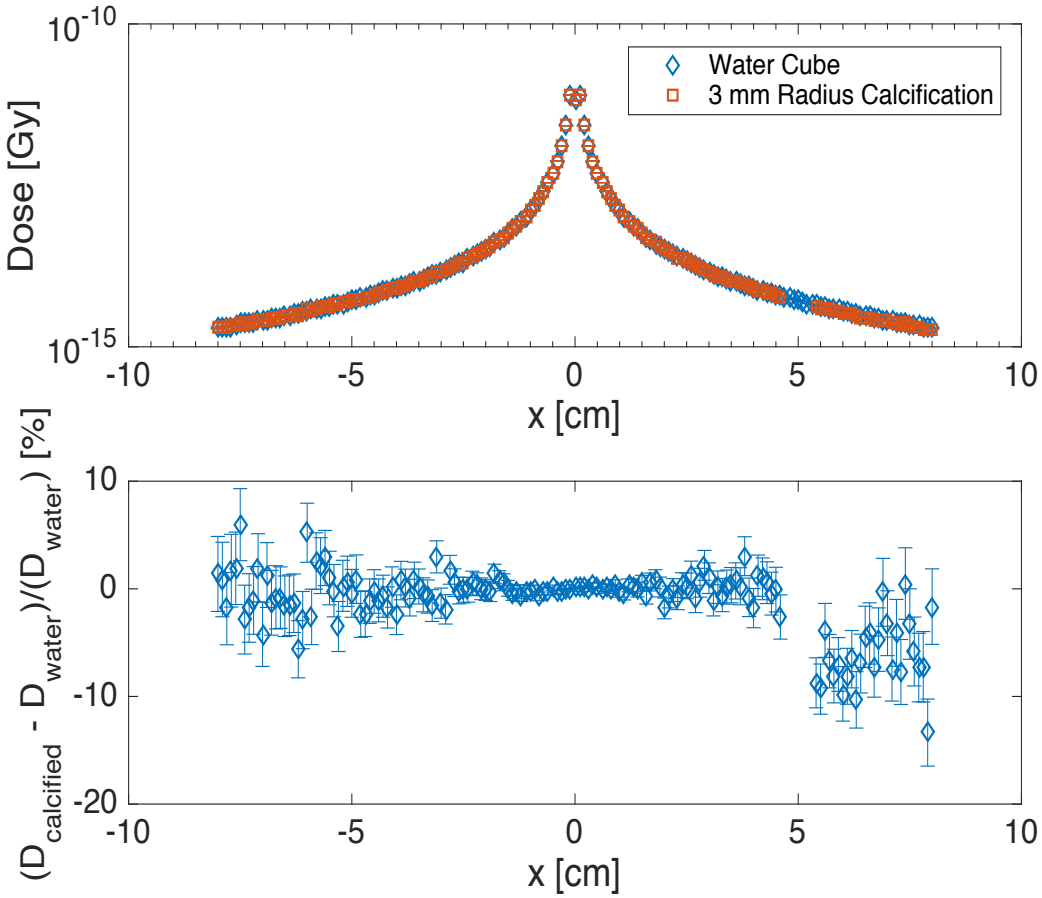

Figure 19 **In the upper plot, the dose profile passing through the center of the microSelectron-v2 source (at the origin) and the center of a 3 mm calcification placed 5 cm away is compared with the same profile in water. Red points have been removed if the voxels involved overlap with the calcification within the gridded geometry. In the lower plot, the corresponding relative dose difference is plotted along the direction of the profile. A mean effect of -6.18% was observed beyond the calcification, compared to -7.42% for the same sized calcification when $\Delta D_{rel,\ 2.5\mu}$ was calculated at r = 5 mm.**

Given the distance of the calcification from the source and the width of the scoring grid (8 cm), it is only sensible to evaluate the mean, maximum and minimum relative dose differences observed beyond the calcification. No other distance metric were considered. For r_c = 1 mm, the mean relative dose difference was -1.70% (with a maximum difference of 3.14% and a minimum difference of -7.64%), whereas the mean relative dose difference for r_c = 3 mm was -6.18% (with a maximum difference of 0.49% and a maximum dose drop of -13.36%). Comparing with Table 10, the mean relative dose differences were roughly comparable to values of $\Delta D_{rel,\ 2.5\mu}$ calculated for a 5 mm separation distance for the same sized calcification. Note that the magnitude of this discrepancy was observably larger for r_c = 3 mm (1.24%) compared to the r_c = 1 mm calcification (0.14%), indicating that the calcification's radius may determine how distance-dependent its dosimetric effect are. The mean dosimetric effects caused by the smaller r_c = 1 mm were within tolerance for the two separation distances assessed in this study, whereas the mean dosimetric effect of the larger r_c = 3 mm calcification increased was greater as the separation distance was decreased to 5 mm. These results should be interpreted cautiously, however, as the scoring grid only extends 3 cm beyond the calcification center and the magnitude of statistical fluctuations at these distances may result in an unreliable estimation of the mean relative dose differences for $r = 5$ cm. Note that the statistical uncertainty in the region after the calcification exceeds the $\pm$ 2% recommendation in TG-56 regarding computer-based dose calculation accuracy (and for r_c = 1 mm, it also exceeds the mean relative dose difference) [30]. As the $\pm$ 2% statistical uncertainty thresholds out the entire region after the calcification as red, the 2D relative dose difference plots have been neglected from the current analysis.

6.3 Patient-Specific Monte Carlo Dose Calculations

6.3.1 Statistical Uncertainty Analysis

Before fully comparing the patient-specific MC dose calculations performed with `tutor7pp` and results obtained using the TG-43 water-based Oncentra Prostate TPS (Elekta Brachytherapy Solutions, Veenendaal, The Netherlands), it was important to assess the distributions of MC statistical uncertainties for all voxels within the prostate, calcification, urethra, rectum and bladder contours. This is visualized using box-and-whisker plots in Figure 20 for a MC dose distribution calculated using a series of water phantoms representing individual source dwell positions. In the MC phantoms, all voxels within the entire contoured body were assigned TG-43 reference water while all other voxels were assigned TG-43 reference air. Dose distributions were calculated for 70 dwell positions and 500 million histories per source collection, resulting in a total of 35 billion simulated particle histories. Uncertainties were calculated using the history-by-history method discussed in Chapter 4. Red crosses represent the mean statistical uncertainties for each structure, while the blue and red markings represent the quartile statistical uncertainties Q_1, Q_2 and Q_3; whiskers are located at the extreme statistical uncertainties of the structure.

For all voxels in structures in close proximity to the ^{192}Ir sources, such as the prostate, calcification and urethra, statistical uncertainties did not exceed 1.0%. The mean statistical uncertainties for these structures were 0.473%, 0.567% and 0.390%, whereas the maximum discrepancies were 0.755%, 0.579% and 0.471% respectively. Hence, statistical uncertainties were well below the TG-56 recommendation of ±2% accuracy for computerized dose calculation algorithms. Structures containing voxels that were far removed from the radioactive sources had more inherent statistical uncertainty, as demonstrated by the box-and-whisker plots associated with the rectum and the bladder. This is attributable to the effective inverse-square law associated with encapsulated ^{192}Ir sources, resulting in fewer photon interactions in those voxels during MC radiation transport. Even so, the maximum statistical uncertainties were below 2% (1.846% and 1.875% for the rectum and the bladder respectively). The results shown in Figure 20 can be considered representative of the distribution of voxel uncertainties for all MC phantoms simulated in this study, as only minor variations were observed for other simulations.

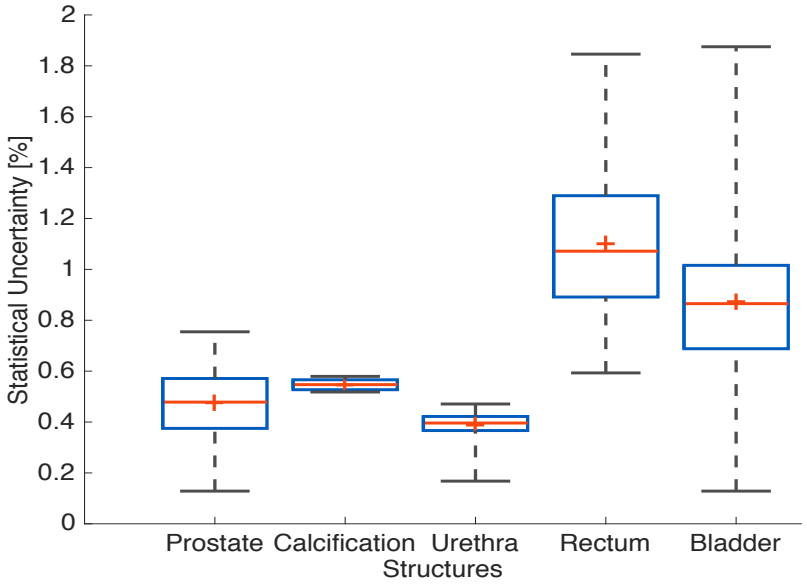

Figure 20 The computed statistical uncertainty distributions for the structures of interest of a MC water phantom. The red crosses represent the mean statistical uncertainty while the blue and red markings represent the quartiles. The black lines represent the range of the uncertainties for a given structure. For 35 billion total particle histories simulated, the statistical uncertainty is below 2% for all structures and below 1% for the prostate, calcification and urethra.

6.3.2 Comparison with TG-43

Figure 21 compares cDVHs associated with the prostate, rectum and urethra as calculated by Oncentra Brachy (Elekta Brachytherapy Solutions, Veenendaal, The Netherlands) ($D_{w,w\text{-}TG43}$, non-dashed) and `tutor7pp` applied to a series of single-source phantoms ($D_{w,w\text{-}MC,}$ dashed). The two calculation approaches were in strong agreement, yielding mean cDVH point differences of 0.947%, 1.2141% and 1.1590% for the prostate, rectum and urethra respectively. The magnitude of these mean MC under-estimations is sensible given the differences in patient scatter conditions and potential differences between the microSelectron-v2 source models used in both calculations.

Nevertheless, the maximum observed discrepancies were more pronounced (2.01%, 3.224% and 3.884% for the same structures) and occurred in the high-gradient regions for all cDVHs. This may be a systematic effect attributable to unresolved differences in the CT structure set resolution at the time of each dose calculation. While MC dose calculations were performed using the resolution of the planning CT structure set (voxel resolution of 1.27 mm 1.27 mm 2.50 mm), Oncentra Brachy (Elekta Brachytherapy Solutions, Veenendaal, The Netherlands) automatically resampled the input structure set to a finer resolution (voxel resolution of 1.00 mm 1.00 mm 1.00 mm) prior to dwell position optimization and dose calculation. This finer structure set resolution increased the number of voxels within the geometry, which might have a moderate impact in high dose gradient regions. Since doses between the treatment planning system calculation with TG-43 and a MC calculation in water were expected to be more similar, this discrepancy remains an open question for future work. Comparisons between Monte Carlo simulations involving water phantoms and TG-43 dose calculations are not widely reported in the literature and it is unclear whether these differences in the cDVHs are to be expected or not. To circumvent this concern, all remaining MC patient-specific cDVH results were compared exclusively to $D_{w,w\text{-}MC}$.

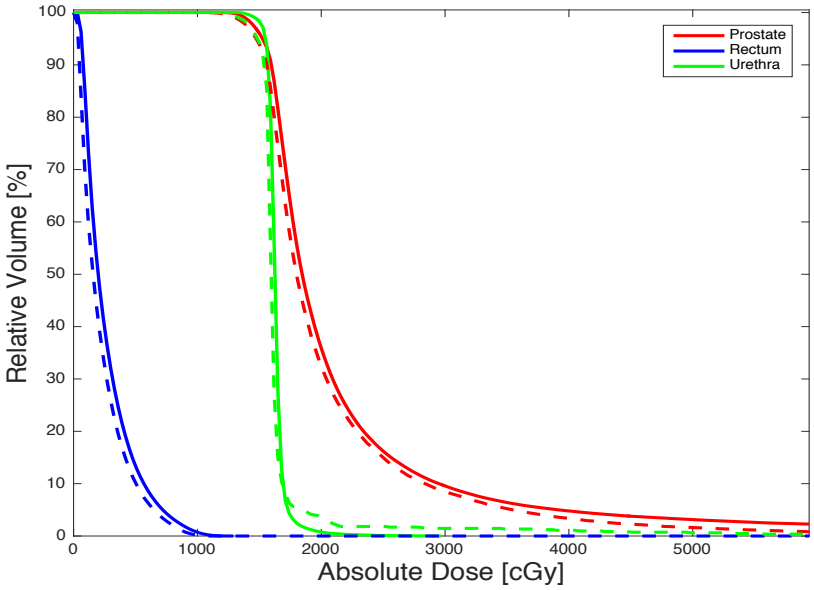

Figure 21 Cumulative dose volume histograms (cDVHs) associated with the prostate, rectum and urethra structures. The solid curves have been calculated using Oncentra Brachy (Elekta Brachytherapy Solutions, Veenendaal, The Netherlands) while the dashed curves have been calculated using `tutor7pp.m`. Plots are in general agreement, although more prominent discrepancies are observed in the high gradient regions of the curves.

6.3.3 Effect of Source Composition on 'TG-186' Scheme Phantoms

In order to assess the dosimetric impact of departing from a water-only geometry, a series of MC phantoms were created using the 'TG-186' tissue assignment scheme and the resultant dose distributions were calculated in a series of MC simulations. While the scheme only assigned a limited number of materials (namely nominal density ICRU mean male soft tissue and nominal density Woodard and White prostate tissue) to the vast majority of phantom voxels, voxels within the calcification contour were assigned a nominal density calcification composition (either ICRU breast calcification, hydroxyapatite or Pope composition #1, depending on the phantom) [4] [41] [49].

Figure 22 compares the prostate clinical metrics (the prostate V_{100}, V_{150} and V_{200}) and urethra D_{10} for all calcified TG-186 phantoms and the Monte Carlo water phantom previously considered. The dashed lines represent the clinical objective for each metric considered, as discussed in Chapter 5. Perturbations caused from the nominal non-water environment and calcification were minimal; the average decreases to the V_{100}, V_{150} and V_{200} were 0.43%, 0.467% and 0.162%, while the urethra D_{10} decreased marginally by an average of 10.7 cGy. The rectum V_{80} was 0 cc for all MC calculations. With the exception of the prostate V_{100}, all clinical outcomes were still met for the MC simulations and all reductions were insignificant compared to reported reductions to metrics in LDR prostate brachytherapy by Collins-Fekete *et al* [50]. Moreover, results indicated that the dosimetric impact was largely independent of the calcification material assessed for this particular patient. This was to be expected, as the calcification is only 0.084 cm^3 according to the treatment planning system (approximately 0.50% of the 17.3 cm^3 prostate volume). With the voxel dimensions of the planning CT used to initialize the simulations, this volume increased only marginally to 0.113 cm^3 (approximately 0.63% of the 18.1 cm^3 prostate volume). Furthermore, nearby sources were only in the vicinity of the calcification for a few seconds during treatment. These results are also sensible in light of the insensitivity of the deep-seated prostate site to changes in radiation scattering conditions.

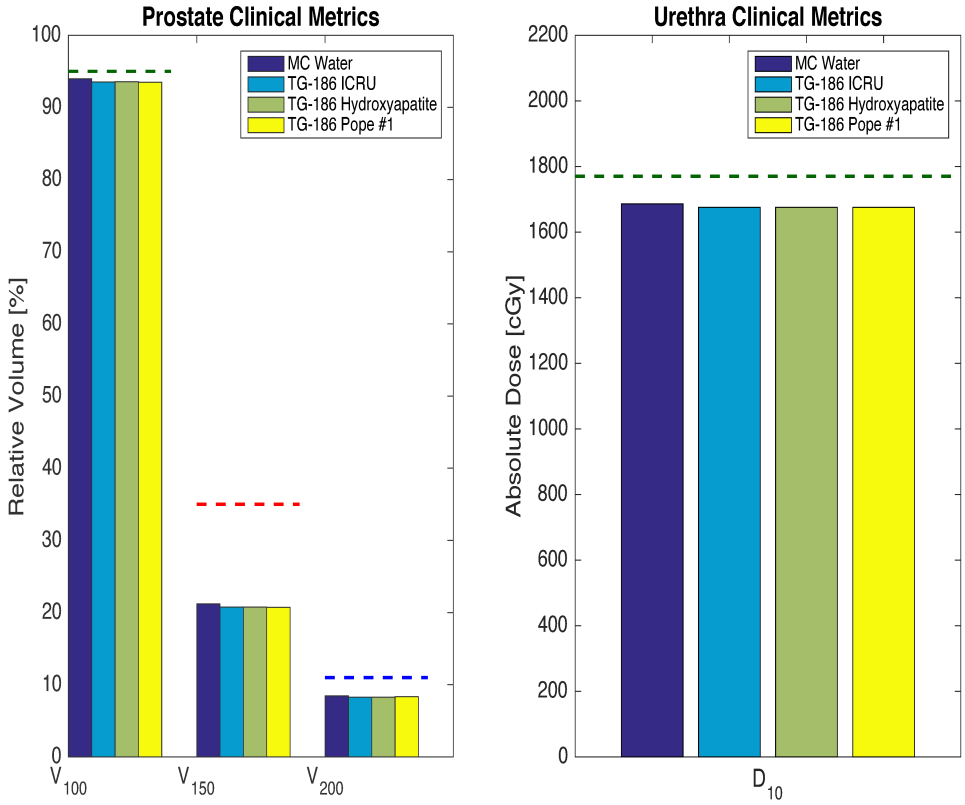

Figure 22 **Prostate clinical metrics (V_{100}, V_{150} and V_{200}) and the urethra D_{10} for the different Monte Carlo calculations. The dark blue indicates a MC phantom consisting of water every except for voxels outside of the body. The lighter blue indicates a phantom calculated using the 'TG-186' assignment scheme with the ICRU breast calcification material, whereas the green and the yellow ones are for hydroxyapatite and Pope composition #1 respectively. Only marginal reductions to clinical metrics are observed, although the prostate V_{100} failed for both MC water and 'TG-186' phantoms.**

This finding is corroborated in Figure 23, in which a 2D axial slice through the $D_{w,w\text{-}MC}$ distribution is shown with its isodose lines (black) and the isodose lines associated with the same 2D axial slice through the $D_{m,m\text{-}MC}$ TG-186 dose distribution (with ICRU breast calcification material) overlaid in magenta. Since the left axial slice passes through the center of the contoured calcification (z = -2.45 cm), a second magnified image on the right is focused upon the isodose lines surrounding the calcification (as indicated by the arrow). The colourbar represents the dose $D_{w,w\text{-}MC}$ (in cGy) within the entire water phantom. While deviations between the contours were not explicitly quantified, the two sets of contours are qualitatively well-aligned (even closer to the calcification itself).

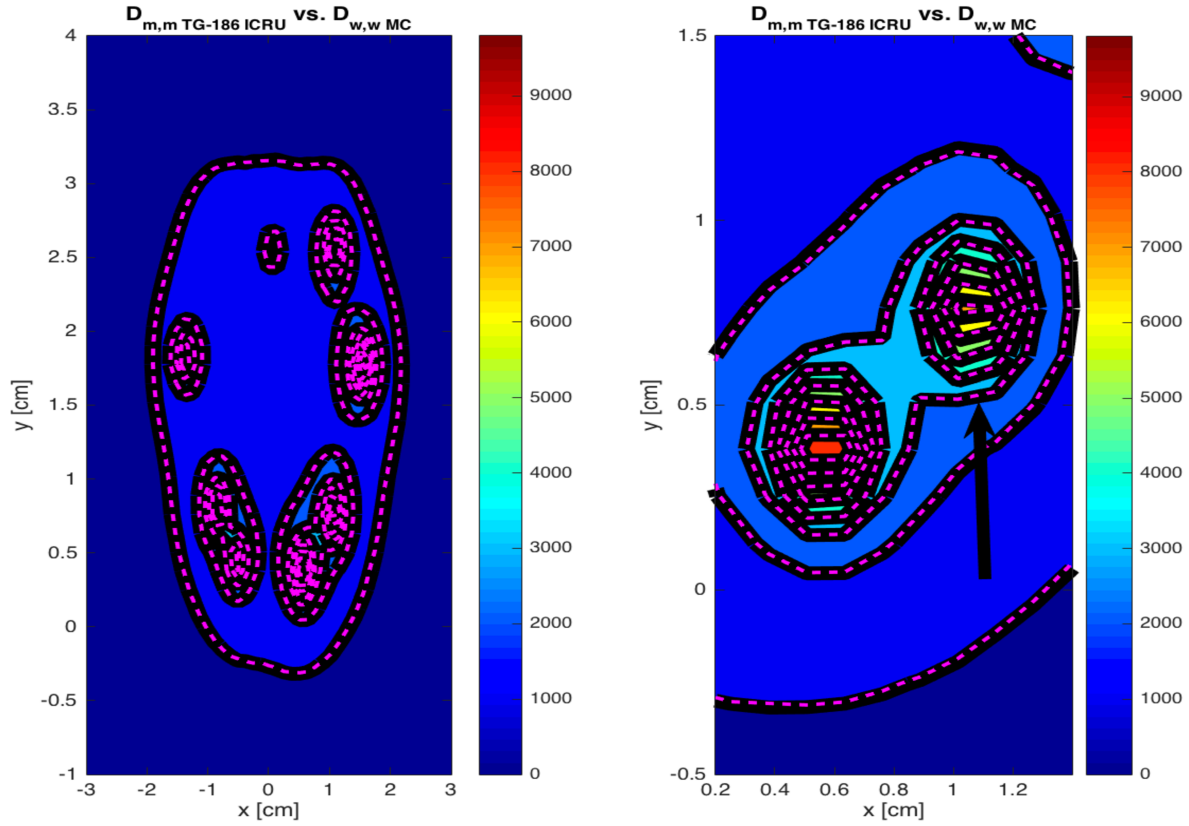

Figure 23 The left image represents a 2D axial slice associated with the dose distribution computed within the water phantom, $D_{w,w\text{-}MC}$. It represents the plane that passes through the center of the calcification. The black isodose lines are representative of $D_{w,w\text{-}MC}$ and the magenta isodose lines represent the isodose curves from the $D_{m,m\ MC}$ distribution using the 'TG-186' scheme with an ICRU breast calcification heterogeneity, which have been overlaid upon the water distribution. The right plot is the same slice magnified around the calcification, indicated by the arrow. Little deviation was observed between the isodose curves at all scales.

6.3.4 'PC' and 'PC-20%' Scheme Results

The 'PC' and 'PC-20%' schemes were also used to initialize MC phantoms in order to assess the impact of incorporating mass density information from the CT images and assigning more voxels as calcified materials. ICRU breast calcification was chosen as the material for the inhomogeneity, while interpolated homogeneous mixtures of ICRU calcification and Woodard and White prostate tissue were also used in the 'PC-20%' scheme [41]. Figure 24 displays the resulting clinical metrics for the two schemes, which were compared to the MC water phantom considered earlier. Results indicated that the dosimetric impact was mild for both schemes, with average reductions for the prostate V_{100}, V_{150} and V_{200} of 0.67%, 0.70% and 0.192%, respectively. The urethra D_{10} was also reduced by 9 cGy on average, while the prostate V_{100} objective remains unsatisfied. Hence, the impact is nowhere near the 2-5% reductions in clinical metric observed in LDR brachytherapy studies by Collins-Fekete *et al*.

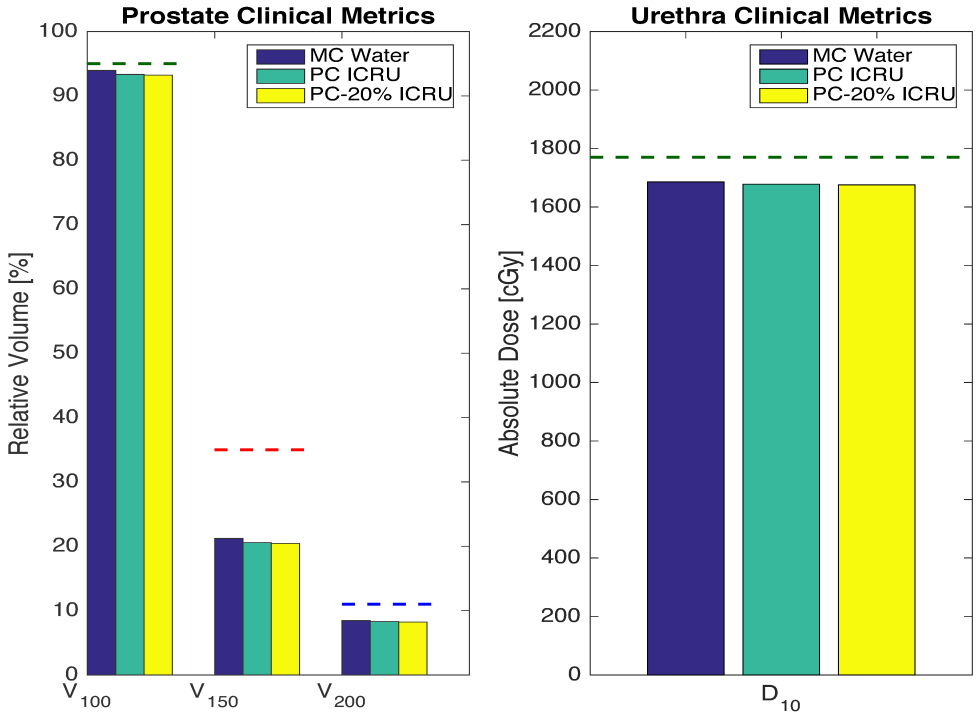

Figure 24 Prostate clinical metrics (V_{100}, V_{150} and V_{200}) and the urethra D_{10} for Monte Carlo calculations that involved CT-derived densities and tissue assignment schemes. Metrics were only slightly affected by adding calcification voxels based upon the mass density of a CT voxel for this particular patient. Once again, the prostate V_{100} objective is not met for the two schemes ('PC' and 'PC-20%').

Clinical values calculated using the 'PC' and 'PC-20%' schemes were virtually indistinguishable from the baseline 'TG-186' scheme results for the patient simulated. This finding is largely explained by the relatively constant size of the high-Z heterogeneity, as the ratio of ICRU calcification volume to the prostate volume increased only marginally from 0.63% (the 'TG-186' scheme) to 1.33% (the 'PC' scheme). Moreover, if one considers only those voxels that were assigned materials with the calcification component exceeding 60% percent mass in the 'PC-20%' scheme (i.e. 40%p60%c, 20%p80%c and pure calcification), this ratio remains fixed at 1.33%.

While the 'PC-20%' scheme assigned 59.1% of the voxels within the prostate to either pure calcification or homogeneous mixtures containing some percentage calcification by mass (i.e. 80%p20%c, 60%p40%c, 40%p60%c and 20%p80%c), this only resulted in a minor reduction in clinical metrics relative to the 'PC' scheme. Of these voxels, 65% were assigned the 80%p20%c composition (a material that barely incorporates the elemental contributions from the calcification). Hence, there is some evidence to indicate that heterogeneity corrections in CT-planned HDR brachytherapy are largely accomplished by the primary tissue compositions (namely Woodard and White prostate and pure ICRU calcification). This reaffirms the TG-186 recommendation to consider only a limited subset of materials for simulations involving MBDCAs.

In fact, questions even arise regarding the necessity of incorporating CT-derived densities into the numerical phantoms. Given the miniscule differences in clinical metrics observed between 'PC' and 'PC-20%' phantoms compared to the 'TG-186' phantom in this work, baseline TG-186 correction using only the structure set and nominal density calcification and prostate materials may be sufficient for a subset of patients. Moreover, given the ±2% dosimetric accuracy of a TG-43-based TPS, some patients may not require a corrected treatment plan computed with a MBDCA. Future work may involve formulating methods for discriminating these subsets of the patient population.

It is important to note that tissue assignment schemes simply use a patient's CT structure set information (along with the optional use of the latent electron density in the CT image itself) to propose feasible physical environments for radiation transport based upon the internal anatomy of the patient. Tissue assignment schemes are merely approximations, as the CT images provide no information about the elemental composition of each mixture and only provide physical density information [36]. Moreover, the tabulated material compositions are only averages and it is known that actual tissue compositions can vary significantly between individuals [36]. Hence, the accuracy of all heterogeneity corrections performed in this study are also impacted by the limitations of the average material compositions and interpolations used to generate homogeneous calcified materials [36].

6.3.5 A Worst-Case Scenario

Figure 25 displays the clinical metrics associated with a worst-case scenario MC phantom, in which the 'TG-186' assignment scheme was used with a contoured calcification of nominal density but 25% of the prostate voxels were also randomly assigned to be nominal density calcification. This extreme case is motivated by an interest in the relationship between the calcification volume to prostate volume ratio and the metrics considered clinically at the NSCC. More pronounced reductions in the prostate V_{100}, V_{150} and V_{200} were observed (1.78%, 1.18% and 0.401%), while the urethra D_{10} was decremented by 26 cGy. As the effect associated with the prostate V_{100} is approaching the ±2% accuracy of a computerized dose calculation algorithm, these results suggest that calcification modeling may still be essential for certain subsets of the patient population with a larger ratio of calcification volume to prostate volume. Even the worst-case scenario assessed had far more mild reductions compared to the 2-5% reductions to clinical metrics in LDR prostate brachytherapy reported by Collins-Fekete *et al.* [53].

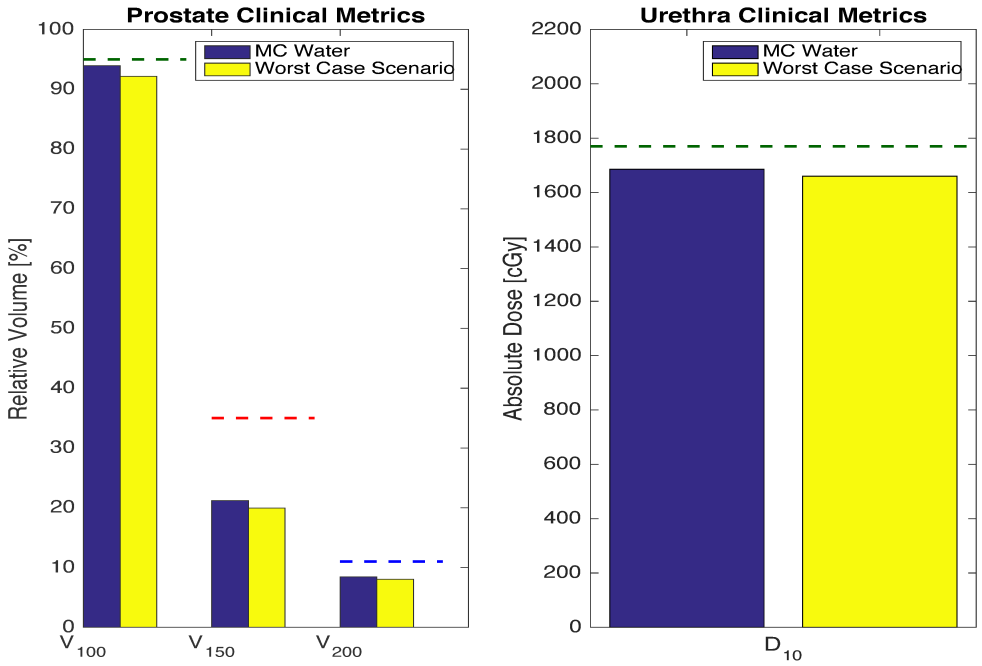

Figure 25 Prostate clinical metrics (V_{100}, V_{150} and V_{200}) and the urethra D_{10} for Monte Carlo calculations for a worst-case scenario calculation that involved assigning 25% of the voxels within the prostate contour outside of the calcification as calcification material of nominal density. The effects were more pronounced compared to previous simulations.

Chapter 7 CONCLUSION

7.1 Summary of Work

In this thesis, a computational framework was developed for performing MC dose calculations on ^{192}Ir HDR brachytherapy plans calculated with treatment planning software at the NSCC. In the current implementation, the CT image set acquired during EBRT planning was used in conjunction with a registered structure set and a tissue assignment scheme to generate truncated patient-specific numerical phantom. Using a modified version of the egspp application `tutor7pp`, dose distributions corresponding to a patient's treatment plan were generated for both homogeneous water and heterogeneous geometries with a calcification [34] [35].

In the worst-case scenario simulated, one quarter of the prostate voxels were assigned to a nominal density calcification material (in addition to the calcification contoured by the researchers). As a result, the prostate V_{100}, V_{150} and V_{200} were only reduced by 1.78%, 1.18% and 0.401% respectively when compared to a MC-calculated water phantom. These discrepancies were smaller than the 1.48% and 6.8% mean dose differences observed from profiles calculated in calcified phantoms (with a 1 mm and 3 mm radius calcification placed at a center-to-center distance of 5 mm away from the source) compared to water phantoms earlier in the study. These mild reductions are not unexpected, given the limited spatial extent of the gross calcification relative to the prostate volume and the short dwell times near the heterogeneity.

It is important to note that results have been predicated upon source validation simulations and a separate comparison between MC patient-specific calculations in water and dose calculations with the TG-43 based Oncentra Brachy (Elekta Brachytherapy Solutions, Veenendaal, The Netherlands). All TG-43 parameters calculated using `tutor7pp` agree well with results by Taylor *et al*. calculated using BrachyDose and further satisfy the 2007 HEBD recommendations for MC benchmarking agreement except at locations along the longitudinal axis of the source [54] [57] [60]. Furthermore, cDVHs determined from MC calculations in water and from Oncentra Brachy (Elekta Brachytherapy Solutions, Veenendaal, The Netherlands) agree within 1.5% on average (with deviations in the high-gradient region possibly attributable to the structure set resolution chosen for MC simulations).

7.2 Future Work

Furthermore, several potential research avenues remain to be explored. For one, more patient simulations will need to be performed in order to fully assess how problematic a calcification can be for patients with more predominant calcified regions. This will also involve a more thorough assessment of the impact the structure set resolution has at the time of dose calculation. A comparison with Nucletron's new model-based dose calculation algorithm (Elekta ACE, which is commercially available for its ^{192}Ir source) is also warranted. A full discussion of the present work's clinical utility is presented in Appendix C.

The interest in dosimetric pre-assessment of prostate cancer patients with calcifications is still in its infancy. While Collins-Fekete *et al*. proposed predicting dose discrepancies between MC patient-specific calculations and TG-43 calculations using the calcification volume to prostate volume ratio, it may be possible to use the tissue assignment schemes to predict dosimetric impact with superior predictive power [53]. In future work, one could run MC simulations retrospectively for a larger population of prostate cancer patients using their CT images and the 'PC-20%' tissue assignment scheme. After the tissue assignment scheme has been implemented, an image histogram can be binned based on the number of voxels associated with each prostate, calcification or mixture material in the tissue assignment scheme relative to the total prostate size. For example, it is hypothesized that patient histograms containing a larger number of voxels associated with pure calcification, 20%p80%c, and 40%p60%c materials could be subject to significant discrepancies in the V_{100}. Identifying modal materials and comparing distributions with similar dosimetric effects may lead the development of more accurate predictions regarding the necessity of model-based dose calculation for a given patient.

In future work, the dosimetric impact of the combination of catheter choice (steel or plastic) and tissue assignment schemes for HDR prostate brachytherapy patients could be considered. It is also possible to extend these methods for the simulation of other sites, including HDR breast treatments that involve breast calcifications and gynaecological sites where the influence of air pockets and choice of applicators might be significant. Additionally, treatments that occur near or on the patient's surface, such as for breast and skin cancers, would be worth investigating due to the lack of scatter from the air. As future developments of EGSnrc appear to be related to simulating non-stationary radioactive sources, transit dose may be more easily assessed in future research [34].

Deformable registration of a preliminary CT images to TRUS images remains a significant impediment to the implementation of MC dose calculations within the clinic. If MC dose calculations have merit for dosimetric pre-assessment, research should be devoted to the development of registration algorithms that perform well (relative to inter-observer variations in contour delineation).

Validation of dose discrepancy due to inhomogeneities merits the development of a method to measure this effect and compare to calculation. Brachytherapy measurements are typically difficult to make due to sharp dose gradients, requiring a detector with a fine resolution. Determining the appropriate detector and creating phantom materials to measure these effects is another avenue of study.

7.3 Closing Remarks

In this thesis, two major research contributions were made. Firstly, it was established in phantom studies that modelling gross high-Z heterogeneities within a few millimeters of an ^{192}Ir source can result in dose decreases (relative to water) between 0.4% and 9% within 2.5 cm of the source. Secondly, a MC framework was developed to establish the impact on a patient-specific geometry using information from a patient's treatment plan. While the prostate V_{100} only decreased by 1.78% in the worst-case scenario simulated, future work involving this framework is required in order to assess whether these mild dosimetric effects are indicative of the prostate brachytherapy patient population at large.

BIBLIOGRAPHY

[1] Canadian Cancer Society [Internet]. [cited 2017 Aug 6]. Available from: http://www.cancer.ca/~/media/cancer.ca/CW/cancer%20information/cancer%20101/Canadian%20cancer%20statistics/Canadian-Cancer-Statistics-2017-EN.pdf?la=en

[2] University of Ottawa Faculty of Medicine [Internet]. [cited 2017 July 14]. Available from: http://www.med.uottawa.ca/sim/data/Aging_e.htm

[3] E. Hansen and M. Roach III, Handbook of Evidence-Based Radiation Oncology, Springer, 2010.

[4] D. Pope. The Dosimetric Effect of Prostate Calcification on Low Dose Rate (LDR) Brachytherapy. *MSc. Thesis*, University of Wollongong.

[5] Urological Research Foundation. Additional Questions- Prostate Cancer. [Internet] [cited 2017 Aug 6]. Available from: http://www.drcatalona.com/qa/arch_other-conditions.asp

[6] RG Uzzo, JT Wei, RS Waldbaum, AP Perlmutter, JC Byrne, and ED Vaughan, "The influence of prostate size on cancer detection," *Urology* **46**(6): 831-836, 1995.

[7] Cancer Treatment Centers of America. Prostate Cancer Symptoms. [Internet]. [cited 2017 Aug 6]. Available from: http://www.cancercenter.com/prostate-cancer/symptoms/

[8] American Cancer Society. Early Detection, Diagnosis and Staging. [Internet]. [cited 2017 Aug 6]. Available from: https://www.cancer.org/cancer/prostate-cancer/detection-diagnosis-staging/staging.html

[9] AV D'Amico, R Whittington, S Malkowicz *et al.*, "Biochemical outcome after radical prostatectomy, external beam radiation therapy, or interstitial radiation therapy for clinically localized prostate cancer," *J. Am. Med. Assoc* 280(**11**):969-974, 1998.

[10] American Cancer Society. Watchful Waiting or Active Surveillance for Prostate Cancer. [Internet]. [cited 2017 Aug 6]. Available from: https://www.cancer.org/cancer/prostate-cancer/treating/watchful-waiting.html

[11] American Cancer Society. Surgery for Prostate Cancer. [Internet]. [cited 2017 Aug 6]. Available from: https://www.cancer.org/cancer/prostate-cancer/treating/surgery.html

[12] American Cancer Society. Hormone Therapy for Prostate Cancer. [Internet]. [cited 2017 Aug 6]. Available from: https://www.cancer.org/cancer/prostate-cancer/treating/hormone-therapy.html

[13] D. Baltas, L. Sakelliou and N. Zamboglou, The Physics of Modern Brachytherapy for Oncology, Taylor & Francis, 2007.

[14] E.B. Podgorsak, Radiation Oncology Physics: A Handbook for Teachers and Students, International Atomic Energy Agency, 2005.

[15] P. Devlin, Brachytherapy: Applications and Techniques, Lippincott Williams & Wilkins, 2007.

[16] J. Van Dyk, The Modern Technology of Radiation Oncology: A Compendium for Medical Physicists and Radiation Oncologists, Vol. 1, Medical Physics Publishing, 1999.

[17] N. Zaorsky, B. Davis, P. Nguyen, T. Showalter, P. Hoskin, Y. Yoshioka, G. Morton, E. Horwitz, "The evolution of brachytherapy for prostate cancer," *Nature Reviews Urology*, **14**:415-439, 2017.

[18] R. Barakat, M. Markman and M. Randall, Principles and Practice of Gynecologic Oncology, Lippincott Williams & Wilkins, 2009.

[19] V. Strnad, R. Pötter and G. Kovács, Practical Handbook of Brachytherapy, Uni-Med Verlag AG., 2014.

[20] International Commission on Radiation Units and Measurements, Dose and volume specification for reporting intracavitary therapy in gynecology. Bethesda, MD: ICRU, 1985.

[21] A. Gerbaulet, R. Pötter, J. Mazeron, H. Meertens, and E. Van Limbergen, The GEC-ESTRO Handbook of Brachytherapy, Brussels, 2002.

[22] J. Sathya, I. Davis, J. Julian, *et al,* "Randomized trial comparing iridium implant plus external-beam radiation therapy with external-beam radiation therapy alone in node-negative locally advance cancer of the prostate," *J. Clin Oncol* **23**:1192-9, 2005.

[23] E. Halperin, L. Brady, C. Perez, and D. Wazer, Perez & Brady's Principles and Practice of Radiation Oncology, Lippincott Williams & Wilkins, 2013.

[24] I. Grills, A. Martinez, M. Hollander, *et al*., "High dose rate brachytherapy as prostate cancer monotherapy reduces toxicity compared to low dose rate palladium seed," *J. Urol.* 171(**3)**:1098-1104, 2004.

[25] J. Mason, B. Al-Qaisieh, P. Bownes, D. Thwaites, A. Henry, "Dosimetry modeling for focal high-dose-rate prostate brachytherapy," *Brachytherapy* **13**:611-617, 2014.

[26] C. Dempsey, J. Arm, L. Best, G. Govindarajulu, A. Capp, P. O'Brien, "Optimal single 3T MR imaging sequence for HDR brachytherapy of cervical cancer," *J. Contemporary Brachytherapy*, 6(**1**):3-9, 2014.

[27] A. Abdellaoui, S. Iyengar, S. Freeman, "Imaging in Prostate Cancer", *Future Oncol.* 7(**5**):679-691, 2011.

[28] J. Hegde *et al.,* "Multiparametric MRI of Prostate Cancer: An Update on State-of-the-Art Techniques and their Perofrmance in Detecting and Localizing Prostate Cancer," *J. Magn. Reson. Imaging*, 37(**5**):1035-1054, 2013.

[29] J. Venselaar, D. Baltas, A. Meigooni, and P. Hoskin, Comprehensive Brachytherapy: Physical and Clinical Aspects, CRC Press, 2013.

[30] R. Nath, L. Anderson, J. Meli, A. Olch, J. Stitt, J. Williamson, "Code of practice for brachytherapy physics: report of the AAPM Radiation Therapy Committee Task Group No. 56", *Med. Phys.* **24**:1557-1598, 1997.

[31] G. Morton, "High-dose-rate brachytherapy for prostate cancer: rationale and technique," *J. Contemp Brachytherapy* 6(**3**):323-330, 2014.

[32] M. Rivard, L. Beaulieu, and B. Thomadsen, Clinical Brachytherapy Physics, AAPM Monograph, 2017 Summer School, Medical Physics Publishing, 2017.

[33] R. Nath, L. Anderson, G. Luxton, K. Weaver, J. Williamson, A. Meigooni, "Dosimetry of interstitial brachytherapy sources: Recommendations of the AAPM Radiation Therapy Committee Task Group No. 43," *Med. Phys.*, **22**:209-234, 2005.

[34] M. Rivard, B. Coursey, L. DeWerd, W. Hanson, M. Huq, G. Ibbott *et al.*, "Update of AAPM Task Group No. 43 Report: A revised AAPM protocol for brachytherapy dose calculations," *Med. Phys.***31:**633-674, 2004.

[35] M. Rivard, W. Butler, L. DeWerd, M. Huq, G. Ibbott *et al.*, "Supplement to the 2004 update of the AAPM Task Group No. 43 Report," *Med. Phys.***34:**2187-2205, 2007.

[36] I. Kawrakow, E. Mainegra-Hing, D.W.O. Rogers, F. Tessier, B.R.B. Walters. The EGSnrc Code System: Monte Carlo simulation of electron and photon transport. Technical Report PIRS-701, National Research Council Canada (2017).

[37] I. Kawrakow, E. Mainegra-Hing, D.W.O. Rogers, F. Tessier, B.R.B. Walters. EGSnrc C++ class library. Technical Report PIRS-898, National Research Council Canada (2017).

[38] L. Beaulieu, Å. Carlsson Tedgren, J. Carrier, S. Davis, F. Mourtada, M. Rivard, R. Thomson, F. Verhaegen, T. Wareing, J. Williamson, "Report of the Task Group 186 on model-based dose calculation methods in brachytherapy beyond the TG-43 formalism: Current status and recommendations for clinical implementation," *Med. Phys.* 39 **10:**6028-6236, 2012.

[39] F.H. Attix, Introduction to Radiological Physics and Radiation Dosimetry, Wiley, New York, 1986.

[40] E. Podgorsak, Radiation Physics for Medical Physicists, Springer, 2016.

[41] National Institute of Standards and Technology. XCOM: Photon Cross Sections Database. [Internet]. [cited 2017 Aug 6]. Available from: https://www.nist.gov/pml/xcom-photon-cross-sections-database

[42] M. Rivard, J. Venselaar, L. Beaulieu, "The evolution of brachytherapy treatment planning," *Med. Phys.* **36**:2136-2153, 2009.

[43] International Commission on Radiological Units and Measurements, "Photon, electron, proton and neutron interaction data for body tissues," Report No. 46 (ICRU Publications, Bethesda, MD, 1992).

[44] J. Seco, F. Verhaegen, Monte Carlo Techniques in Radiation Therapy, Taylor and Francis, 2016.

[45] I. Chetty, B. Curran, J. Cygler, J. DeMarco, G. Ezzell, B. Faddegon, I. Kawrakow, P. Keall, H. Liu, C. Ma, D.W.O. Rogers, J. Seuntjens, D. Sheikh-Bagheri, J. Siebers, "Report of the AAPM Task Group No. 105: Issues associated with clinical implementation of Monte Carlo-based photon and electron external beam treatment planning," *Med. Phys.* **34**:4818-4853, 2007.

[46] B.R.B. Walters, I. Kawrakow, D.W.O. Rogers. History by history statistical estimators in the BEAM code system. Technical Report PIRS-0791, National Research Council Canada (2002).

[47] M. Chamberland, R. Taylor, D. Rogers, R. Thomson, "egs_brachy: a versatile and fast Monte Carlo code for brachytherapy," *Phys. Med. Biol.* **61**:8214-8231, 2016.

[48] J. Suh, J. Gardner, K. Kee, S. Shen, A. Avala, J. Ro, "Calcifications in prostate and ejaculatory system: a study on 288 consecutive whole mount sections of prostate from radical prostatectomy or cystoprostatectomy specimens", *Annals of Diagnostic Pathology* **12**:165-170, 2008.

[49] O. Chibani, J. Williamson, D. Todor, "Dosimetric effects of seed anisotropy and interseed attenuation for ^{103}Pd and ^{125}I prostate implants," *Med. Phys.* **32:**2557-2566, 2005.

[50] T. Hsu, S. Lin, C. Lin, W. Cheng, "Preliminary feasibility study of FTIR microscopic mapping system for the rapid detection of the composited components of prostatic calculi," *Urol Res.* **39**:165-170, 2011.

[51] D. Pope, D. Cutajar, S. George, S. Guatelli, J. Bucci, K. Erari, S. Miller, R.Siegele, A. Rosenfeld, "The investigation of prostatic calcifications using μ-PIXE analysis and their dosimetric effect in low dose rate brachytherapy treatments using Geant4", *Phys. Med. Biol.* **60**:4335-4353, 2015.

[52] J. Carrier, M. D'Amour, F. Verhaegen, B. Reniers, A. Martin, E. Vigneault, L. Beaulieu, "Postimplant dosimetry using a Monte Carlo dose calculation engine: a new clinical standard," *Int. J. Radiation Oncology Biol. Phys.,* **68**:1190-1198, 2007.

[53] J. Mason, B. Al-Qaisieh, P. Bownes, A. Henry, D. Thwaites, "Investigation of interseed attenuation and tissue composition effects in ^{125}I seed implant prostate brachytherapy," *Brachytherapy* **13**:603-610, 2014.

[54] N. Miksys, C. Xu, L. Beaulieu, R. Thomson, "Development of virtual patient models for permanent implant brachytherapy Monte Carlo dose calculations: interdependence of CT image artifact mitigation and tissue assignment," *Phys. Med. Biol.* **60**:6039-6062, 2015.

[55] C. Collins-Fekete, M. Plamondon, A. Martin, E. Vigneault, F. Verhaegen, L. Beaulieu, "Calcifications in low-dose rate prostate seed brachytherapy treatment: Post-planning dosimetry and predictive factors", *Radiotherapy and Oncology* **114**:339-344, 2015.

[56] R. Taylor, D. Rogers, “EGSnrc Monte Carlo calculated dosimetry parameters for ^{192}Ir and ^{169}Yb brachytherapy sources”, *Med Phys.* **35**:4933–44, 2008.

[57] R. Taylor, G. Yegin, DW Rogers, “Benchmarking BrachyDose: Voxel based EGSnrc Monte Carlo calculations of TH-43 dosimetry parameters”, *Med Phys.* **34**:445–57, 2007.

[58] G. M. Daskalov, E Löffler, J Williamson, “Monte Carlo-aided dosimetry of a new high dose-rate brachytherapy source”, *Med. Phys*., **25**:2200-2208, 1998.

[59] G. M. Daskalov, Erratum: "Monte Carlo-aided dosimetry of a new high dose-rate brachytherapy source" [Med. Phys. 25, 2200-2208 (1998)], *Med. Phys*. **27**:1999--1999, 2000.

[60] B. Mathews. Development of a Monte Carlo based correction strategy for a TG-43 based brachytherapy treatment planning system to account for applicator heterogeneities. *MSc. Thesis*, Louisiana State University.

[61] B. Duchemin and N. Coursol, “Reevaluation de l’^{192}Ir,” Technical Note LPRI/93/018, DAMRI, CEA, France, 1993.

[62] J. Perez-Calatayud, F. Ballester, R. Das, L. DeWerd, G. Ibbott, A. Meigooni, Z. Ouhib, M. Rivard, R. Sloboda, J. Williamson, “Dose calculation for photon-emitting brachytherapy sources with average energy higher than 50 keV: Report of the AAPM and ESTRO,” *Med. Phys.* **39**:2904-2929, 2012.

[63] H. Woodard and D. White, “The composition of body tissues,” *Br. J. Radiol.* **59**:1209-1218, 1986.

[64] B.R.B. Walters, I. Kawrakow, D.W.O. Rogers. DOSXYZnrc Users Manual. Technical Report PIRS-794revB, National Research Council Canada (2017).

[65] E Poon. Patient-specific dose calculation methods for high-dose-rate iridium-192 brachytherapy. *PhD. Thesis*, McGill University.

APPENDIX A AJCC Staging for Prostate Cancer

Table A.1: Primary tumour (T) classification criteria (AJCC, 7th ed., 2010) [3]

Primary tumour (T) [3]	Description [3]
TX	Unable to be assessed
T0	No primary tumour observed in all tests (histological findings, biopsies, etc.)
T1	Tumour not seen in diagnostic images and not palpable T1a: Tumour observed in ≤ 5% of tissue resected in histological analysis T1b: Tumour observed in > 5% of tissue resected in histological analysis T1c: Tumour observed in needle biopsy
T2	Tumour confined to prostate T2a: Involves half a lobe or less T2b: Involves more than half of one lobe, but not both T2c: Involves both lobes
T3	Tumour extends through prostate capsule T3a: Extracapsular extension T3b: Invasion of seminal vesicles
T4	Tumour is fixed or invades adjacent structures

Table A.2: Regional lymph nodes (N) classification criteria (AJCC, 7th ed., 2010) [3]

Regional lymph nodes (N) [3]	Description [3]
NX	Regional lymph nodes not considered
N0	No regional lymph node metastasis
N1	Regional lymph node metastasis

Table A.3: Distant metastasis (M) classification criteria (AJCC, 7th ed., 2010) [3]

Distant metastasis (M) [3]	Description [3]
M0	No distant metastasis
M1	Distant metastasis

APPENDIX B Clinical Utility

The MC framework developed in this study has been largely motivated by the clinical concerns of the NSCC unable to be met with Nucletron's TG-43 based Oncentra Brachy treatment planning system (Elekta Brachytherapy Solutions, Veenendaal, The Netherlands). Clinical medical physicists and physicians alike have expressed interest in a tool that is capable of performing dosimetric pre-assessments of selected patients classified as having potentially perturbative heterogeneities (such as prostate calcifications). Given the strong agreement between cDVHs generated from the Oncentra Brachy treatment planning system (Elekta Brachytherapy Solutions, Veenendaal, The Netherlands) and the egspp MC simulations conducted in water, this objective is within reach for intermediate- or high-risk prostate cancer patients about to undergo ^{192}Ir HDR brachytherapy at the NSCC.

A number of caveats and areas for future refinement of the MC framework are worthy of further discussion. The `tutor7pp` application currently runs using the default EGSnrc radiation transport software operating on the NSCC computer cluster (with many source code files that have not been updated since 2012) [31]. This dependency on the global cluster settings introduces a host of limitations that impede efficient clinical utility for all potential users, including medical physicists, physicians and researchers. Administrator access is required in order to modify the source code and re-recompile the software to fit the research needs, which itself is not necessarily a trivial task. This led to two pertinent issues that were never fully resolved and only circumvented over the course of this research:

- (1) Rarely, a small number of running jobs fail to finish and appear to be caught within an infinite loop. It is believed to be related to a known issue in older egspp code involving the file *egs_cones.h* and it is crudely estimated to occur once in every 10^9 particle histories simulated [32]. A particle generated from the source core is quantified by its distance away from various parts of the source's conical section with the EGSnrc HOWFAR function, but floating points errors currently allow this distance to be negative and cause the infinite loop [31] [32]. This issue is generally circumvented by simply re-running the affected simulations with more CPUs, but prolongs the simulation time unnecessarily.
- (2) By default, all n source positions to be simulated for a patient's treatment plan are distributed over five CPUs to ensure dose calculations for a given source position are quick and efficient. Hence, $5n$ data files (*.egsdat) must be combined at the end using a shell script. The relevant source code, contained in *egs_application.cpp*, only combines the first 500 *.egsdat files detected in alphanumerical order into a *.egslog file. Under the assumption that all jobs finish correctly, simulations are thus limited to 100 dwell positions unless one combines multiple sets of *.egsdats into multiple *.egslog files. At the NSCC, some brachytherapy plans involve the use of 200 dwell positions or more. Given that the time required to combine results is approximately 20-30 minutes per *.egslog for the patient simulated in this study ($n = 70$), it is feasible to repeat this process for $n > 100$. However, this may be undesirable for the clinician.

Alternatively, users can download a local version of EGSnrc 2017 for use with the cluster by altering the .alias and .cshrc files governing a particular user's Linux environment [31]. However, some preliminary test simulations performed with the EGSnrc 2017 code (undocumented in this thesis) generated geometry-related errors [31] [32]. Hence, there is some concern that the simulation geometry files used in this study are not portable with newer versions of EGSnrc [31] [32]. This poses a concern if one wishes to implement variance reduction techniques from the upcoming code from `egs_brachy` [42]

It is important to emphasize that the MC software and source design has not been clinically commissioned and is not permitted for use in any activity directly related to treatment. While the current MC framework certainly has the potential for tangible clinical utility, it should be philosophically regarded as a research tool.